

The JCMT Nearby Galaxies Legacy Survey. VII. $H\alpha$ imaging and massive star formation properties

J. R. Sánchez-Gallego,^{1,2*} J. H. Knapen,^{1,2} C. D. Wilson,³ P. Barmby,⁴
M. Azimlu^{4,5} and S. Courteau⁶

¹*Instituto de Astrofísica de Canarias, E-38205 La Laguna, Tenerife, Spain*

²*Departamento de Astrofísica, Universidad de La Laguna, E-38200, La Laguna, Tenerife, Spain*

³*Department of Physics & Astronomy, McMaster University, Hamilton, Ontario, L8S 4M1, Canada*

⁴*Physics and Astronomy Department, University of Western Ontario, 1151 Richmond Street, London, Ontario, N6A 3K7, Canada*

⁵*Harvard-Smithsonian center for Astrophysics, 60 Garden St., Cambridge, MA, 02138, USA*

⁶*Department of Physics, Engineering Physics and Astronomy, Queen's University, Kingston, ON K7L 3N6, Canada*

Accepted 1988 December 15. Received 1988 December 14; in original form 1988 October 11

ABSTRACT

We present $H\alpha$ fluxes, star formation rates (SFRs) and equivalent widths (EWs) for a sample of 156 nearby galaxies observed in the $^{12}\text{CO } J = 3 - 2$ line as part of the James Clerk Maxwell Telescope Nearby Galaxies Legacy Survey. These are derived from images and values in the literature and from new $H\alpha$ images for 72 galaxies which we publish here. We describe the sample, observations and procedures to extract the $H\alpha$ fluxes and related quantities. We discuss the SFR properties of our sample and confirm the well-known correlation with galaxy luminosity, albeit with high dispersion. Our SFRs range from 0.1 to $11 M_{\odot} \text{ yr}^{-1}$ with a median SFR value for the complete sample of $0.2 M_{\odot} \text{ yr}^{-1}$. This median values is somewhat lower than similar published measurements, which we attribute, in part, to our sample being H I-selected and, thus, not biased towards high SFRs as has frequently been the case in previous studies. Additionally, we calculate internal absorptions for the $H\alpha$ line, $A(H\alpha)$, which are lower than many of those used in previous studies. Our derived EWs, which range from 1 to 880 Å with a median value of 27 Å, show little dependence with luminosity but rise by a factor of five from early- to late-type galaxies. This paper is the first in a series aimed at comparing SFRs obtained from $H\alpha$ imaging of galaxies with information derived from other tracers of star formation and atomic and molecular gas.

Key words: galaxies: star formation – galaxies: ISM – infrared: galaxies – submillimetre: galaxies.

1 INTRODUCTION

Along with galaxy interactions and the presence of active nuclei, star formation efficiency is one of the most important factors that controls a galaxy's structure and evolution. Although the subject has been extensively researched both in the local Universe (e.g., Kennicutt & Kent 1983; Gallego et al. 1995; Alonso et al. 1999; James et al. 2004; Kennicutt 2008) and in the more distant Universe (e.g., Madau et al. 1996; Hopkins, Connolly & Szalay 2000; Lanzetta et al. 2002; Nagamine et al. 2006), many fundamental questions in galactic and extragalactic research remain.

In the local Universe, many surveys have been carried out in different wavelengths (see, for example, Kennicutt 2008 for an extensive compilation of literature data) to probe

the star formation rate. Among these, the $H\alpha$ line is one of the most widely used star formation rate (SFR) tracers, both photometrically and spectroscopically (Kennicutt 1998). In contrast to, e.g., the Far Ultra-Violet (FUV), $H\alpha$ lies in the optical region for nearby galaxies, thus allowing easy ground-based observations. In addition, the spatial resolution which can be obtained with $H\alpha$ is superior to what is normally obtained at other wavelengths such as the Infrared (IR), which are also more complicated to observe with ground-based telescopes. Studies carried out throughout almost two decades have proved that the $H\alpha$ line is a solid tracer of star formation, especially if the measurements are complemented by the use of Far Infrared (FIR) data (e.g., Calzetti et al. 2007, 2010; Leroy et al. 2012).

Recent studies (see Wilson et al. 2009 and references therein) state that the warm, dense molecular hydrogen is better correlated with star formation than the cold, more

* E-mail: jrsg@iac.es

dispersed gas. Due to the lack of a permanent dipole moment, all the ground-based observations aimed to detect molecular hydrogen are made using alternative tracers. Although not the only method at hand (Gautier et al. 1976; Neufeld & Yuan 2008), the spectral lines produced by the different rotational transitions of the CO molecule stand as the best known and most widely used tracers of molecular hydrogen. However, the vast majority of surveys aiming to study the molecular gas in nearby galaxies have focused on the lower transitions ($J = 1 - 0$, $J = 2 - 1$) of CO, which do not discriminate between cold and warm gas.

The James Clerk Maxwell Telescope (JCMT) on Mauna Kea, Hawai'i is currently hosting a series of Legacy Surveys, including the Nearby Galaxies Legacy Survey (NGLS) which aims to map 156 galaxies in the CO $J = 3 - 2$ spectral line and in the 450 and 850 μm continuum (C. Wilson et al., in preparation). All the CO $J = 3 - 2$ observations have been completed and the continuum observations have begun. Further information about the scope and science goals of this survey can be found in Wilson et al. (2009) as well as in the subsequent series of papers which make use of the CO $J = 3 - 2$ data (Warren et al. 2010; Bendo et al. 2010; Irwin et al. 2011; Wilson et al. 2011; Sánchez-Gallego et al. 2011).

Because of the physical conditions needed to activate this transition, the $J = 3 - 2$ line is perfect to trace and study the warm molecular gas which is most likely to form stars. This directly inspires the interest in observing this same sample using a well proven tracer of star formation such as $\text{H}\alpha$.

This paper is organized as follows. Section 2 introduces the sample and the criteria used for its selection; Sections 3 and 4 describe the observations and the origin of the literature data used in this work. Section 5 explains in detail the complete process of data analysis, from the most basic reduction to the continuum subtraction, flux measurements and SFR and EW calculations. In Section 6 we analyze the SFR and equivalent width (EW) results obtained. They are compared with previous data from the literature in Section 7. Finally, Section 8 presents the main conclusions and outlines the future work we plan to do with these data.

2 SAMPLE SELECTION

This work presents $\text{H}\alpha$ photometry for a total of 156 nearby galaxies. The sample of galaxies has been mostly H I-flux selected in order to avoid a SFR-driven selection (as would have happened using a FIR flux criterion) while ensuring that the galaxies have a rich interstellar medium. All our galaxies are contained within a range between 2 and 25 Mpc in distance ($v < 1875 \text{ km s}^{-1}$) and were selected to cover the complete morphological spectrum, from early-type spirals and ellipticals to late-type spirals and irregular galaxies. Both field and Virgo cluster galaxies are well represented in each morphological bin. Most of the Virgo galaxies have $D_{25} < 4 \text{ arcmin}$, which allowed us to use the jiggle map method during the CO $J = 3 - 2$ observations (Warren et al. 2010) carried out with the JCMT. C. Wilson et al. (2011, in prep.) give a more detailed explanation of the criteria and parameters used to construct the sample.

The complete sample has been compiled from three different subsets: (1) 48 galaxies taken from the *Spitzer* In-

frared Nearby Galaxies Survey (SINGS; Kennicutt et al. 2003); (2) 36 galaxies chosen from a H I flux-limited sample of galaxies from the Virgo cluster; and (3) 72 H I flux limited field galaxies. The fact that a significant part of our list of targets matches the SINGS sample ensures that a large amount of multi-wavelength data is available for those galaxies, from the infrared imaging obtained by the SINGS team to H I data (for example, from THINGS; Walter et al. 2008) and UV imaging from *GALEX*. However, SINGS used FIR emission to constrain its sample, which leads to a certain bias towards spiral, star-forming galaxies. This bias also appears in our sample, as can be seen in Figure 1, which shows the distribution of the galaxies of our sample across the Hubble sequence and the contribution of each subsample. This bias will also become apparent when we discuss the SFRs (Section 6). The morphological breakdown is as follows: 4 elliptical galaxies ($T \in [-6, -4]$), 20 lenticular galaxies ($T \in [-4, 0]$), 50 early spiral galaxies ($T \in [0, 4.5]$), 49 late spiral galaxies ($T \in [4.5, 9.5]$) and 33 irregular galaxies ($T \in [9.5, 10]$). We make a distinction between small ($D_{25} < 4 \text{ arcmin}$) and large galaxies in the SINGS subsample. The sample is given in Table 1.

3 NEW $\text{H}\alpha$ OBSERVATIONS

We have imaged 72 out of the 156 sample galaxies in the $\text{H}\alpha$ line. While a small subset of these galaxies had $\text{H}\alpha$ data available in the literature, we decided that the images were either not deep or not detailed enough to serve our purpose and we reobserved them.

For these observations, we made extensive use of several of the telescopes located on the Roque de los Muchachos Observatory (La Palma, Canary Islands). In particular, we used: (1) the Wide Field Camera (WFC) mounted on the 2.5 meter Isaac Newton Telescope (INT), (2) the Auxiliary port Camera (ACAM) and the auxport camera (AUX) on the 4.2 meter William Herschel Telescope (WHT), and (3) the Andalucia Faint Object Spectrograph and Camera (ALFOSC) on the 2.5 meter Nordic Optical Telescope (NOT). Additional images were taken using the MDM8K mosaic camera on the 2.4 meter Hiltner telescope at the Michigan-Dartmouth-MIT Observatory (Kitt Peak). Table 1 summarizes the dates, observing conditions, exposure times and filters used for each galaxy.

Although working with different telescopes and instruments, we kept a systematic observation strategy. Each galaxy was observed through a narrow-band filter redshifted to the position of the $\text{H}\alpha$ line for each galaxy. The narrow filters used had a width in the range 15 – 50 \AA with transmissions always above 50% and, generally, higher than 70%. We ensured that the $\text{H}\alpha$ line always fell in the region of maximum transmission of the filter. For each target we obtained at least three $\text{H}\alpha$ images in order to remove cosmic ray hits through the combination of the different images. Standard exposure times were $3 \times 300 \text{ s}$.

The continuum subtraction was done using an R broad-band image. Due to the low recession velocity of our galaxies, no other filters were necessary to obtain the continuum contribution in the $\text{H}\alpha$ region. We typically obtained $3 \times 180 \text{ s}$ continuum exposures which were combined to produce a single R -band image.

Sky flat frames were taken during both the evening and morning twilights. In some cases this was not possible due to adverse atmospheric conditions during one or both twilights. In some of these cases, dome flats were taken. A series of bias exposures was obtained at the beginning of the night and again at the end. Typically the bias was constant and uniform throughout the night.

The photometric calibration was carried out by observing at least one spectrophotometric standard star at the beginning of the night and at the end. Landolt (1992) photometric stars were used for the R -band calibration. While most of the images were obtained during photometric nights, some galaxies were observed in clear but not perfect conditions. In those cases we did not calibrate the images. Instead, we reobserved the galaxies during photometric nights, obtaining short exposures (typically 1/4 the original exposure times) which we used to calibrate the previous images.

4 LITERATURE DATA

The remaining 84 galaxies in our list had previously been observed, and photometrically calibrated $H\alpha$ imaging was available in the literature. These include: 25 galaxies from the $H\alpha$ Galaxy Survey ($H\alpha$ GS; James et al. 2004); 33 galaxies from SINGS (Kennicutt et al. 2003); 4 galaxies from Knapen et al. (2004); 4 galaxies from Kennicutt et al. (2008); and 18 galaxies from the GoldMine project (Gavazzi et al. 2002, 2006; Boselli et al. 2002).

For these galaxies, the headers of the FITS files have been modified to match the global standards of this work (see Section 5.4) and the images have been divided by the exposure time to get an effective exposure time (t_{exp}^*) equal to 1 second. If necessary, the astrometric solution in the images was improved.

When possible (i.e., when both the original $H\alpha$ and the continuum images were available) we did not use the $H\alpha$ continuum-subtracted image from the literature, but we performed our own continuum subtraction as explained in Section 5.2. We used the final images to measure our own flux values and derived properties, as described in Sections 5.5-5.8.

5 DATA REDUCTION

5.1 Basic reduction

The data reduction is quite straightforward and we refer to the corresponding procedures described in Knapen et al. (2004). The reduction was performed using mainly packages and tasks from IRAF¹. Again, slightly different procedures were carried out depending on the instrument used to acquire the images. The main steps were, however, common to all the images regardless of their origin. The basic steps were as follows.

a) A median bias frame was produced combining all valid bias exposures. This median bias was then subtracted from each of the flat field and science images. Some images from the literature were bias-corrected using a constant value

(namely the mean value of the median bias frame) rather than the master bias image (see Knapen et al. 2004). This is no problem as the structure of the individual bias frames was negligible in those cases.

b) The flat field correction was applied using an adequate median sky flat obtained from the flat frames for each filter. Evening and morning sky flats were analyzed separately although, in the majority of cases, no important differences were found and all the flat frames were combined.

c) The images were aligned, their background was subtracted and they were weighted by their exposure time and then combined by filter using the median. A sigclip rejection algorithm was applied to remove pixels with values above or below 3σ . This ensures that most of the cosmic rays were successfully removed.

d) Although in most cases the images had a good astrometric calibration, a new astrometric solution was applied to each image using the Guide Star Catalogue II (GSC-II; Lasker et al. 2008). The final precision is better than one arcsec.

5.2 Continuum subtraction

Once both the $H\alpha$ on-line and the continuum images are completely reduced we must subtract the contribution of the continuum to the $H\alpha$ flux. The great majority of our continuum images were obtained using R -band filters and the rest of this subsection will deal with that situation. However, for a small number of cases (all from the literature) the continuum image is a narrow filter of width similar to that of the $H\alpha$ filter but shifted in wavelength so that only the continuum and not the line is measured. In these cases the procedure to subtract the contribution of the continuum is similar to when using R -band, but much more straightforward as the scale factor between the $H\alpha$ and the continuum images is always ~ 1 .

The method used to calculate the scale factor of the continuum image is well explained in Knapen et al. (2004) and we refer to that paper for further details. First, if there is an important difference between the full widths at half maximum (FWHMs) of the $H\alpha$ and continuum images, we smooth the images to the worst FWHM using a Gaussian convolution. Then, we plot the intensity of each pixel in the $H\alpha$ image, in counts per second, versus the intensity of the same pixel in the R -band image. In general, a certain percentage of the brightest pixels (usually around 3%) is removed to avoid the contribution of field stars. The resulting plot shows a strong linear correlation which can be fitted using a least squares regression line, the slope of which gives the scale factor between the two images. Although this method has been found to produce consistently good results, some galaxies (especially those with very low emission) require further processing to obtain the optimum scale factor value. Thus, a final small correction by hand was often made to ensure that the continuum subtraction was optimal by looking at different regions of the galaxy and ensuring that no area was oversubtracted. While it is not always trivial to find the most accurate scale factor, small differences in the value of this parameter do not affect the derived values (flux, SFR, EW) in a significant way.

It must be taken into account that the continuum image used is contaminated by the flux of the $H\alpha$ line. The

¹ <http://iraf.noao.edu/>

contribution of the line has previously been estimated to be 3% of the total integrated flux in the R -band (James et al. 2004). This effect does not occur when the filter used for the continuum subtraction is a narrow one, as in that case the $H\alpha$ line is not present at all. Integrating the transmission curves of the filters used, we calculated how much the $H\alpha$ line contributed to the continuum flux. We found that, for most sets of filters, the correction was in the range 2-4% with some extreme cases as high as 6%. The calibration was modified according to the value found for each galaxy. Table 2 shows the correction applied.

5.3 Photometric calibration

The next stage in the reduction process was to calibrate the science frames photometrically. The R -band calibration was done using Landolt (1992) standard stars and taking the airmass of the objects into account. For the calibration of the $H\alpha$ images, following Knapen (1992), we considered the flux density, f_λ , given by

$$\log f_\lambda = -0.4\text{mag}_\lambda - 8.42,$$

with f_λ in units of $\text{erg s}^{-1} \text{cm}^{-2} \text{\AA}^{-1}$. To calculate the zero point factor we performed aperture photometry of the spectrophotometric standard stars selected. For these stars, the value of mag_λ is tabulated every few angstroms. All the stars used are from either Stone (1977), Massey et al. (1988) or Oke (1990). If χ is the total flux of the standard star in units of counts s^{-1} , the zero point factor can be written as

$$\text{ZP} = \frac{\Delta\lambda f_\lambda}{\chi},$$

where $\Delta\lambda$ corresponds to the width of the $H\alpha$ filter used. ZP has units of $\text{erg cm}^{-2} \text{count}^{-1}$. The flux for a certain region can be calculated as

$$\log_{10} F = \text{ZP} + \log_{10}(\text{counts}),$$

in units of $\text{erg cm}^{-2} \text{s}^{-1}$. In this expression we have taken into account that the effective exposure time of our images is one second.

5.4 Final image preparation

The final images for each galaxy ($H\alpha$ without continuum subtraction, R -band and continuum-subtracted $H\alpha$) were rotated North-up and trimmed. The FITS headers of all images (including those obtained from the literature) have been modified in the following way: first, a custom header has been inserted including the relevant data (total exposure time, zero point, flux and luminosity per count, etc); second, the original header has been preserved after our custom header. The units in the final images are always counts per pixel (i.e., the exposure time has been set to one second). The original exposure time for each frame is stored in the header of the image under the field DARKTIME.

When working with literature data, the astrometric solution provided with most of the images was well below the FWHM of the frames and no correction was made. In some cases, however, the astrometric solution was wrong or nonexistent. Those images were astrometrically calibrated using the *Guide Star Catalogue* (Lasker et al. 1990) which provides an accuracy better than one arcsec.

5.5 Flux measurement

In order to determine the $H\alpha$ flux without the contribution of field stars, we masked all the stars near the galaxy while taking special care not to remove any H II regions. We used the masking utility integrated in Gaia (Draper et al. 2009) which substitutes the region to mask based on an estimate of the values of the surrounding pixels. We applied a third order surface fit, which in all cases produced an excellent result. The stars were masked in the continuum band and, when necessary, also in the $H\alpha$ continuum-subtracted image.

To calculate the integrated $H\alpha$ flux of the galaxies we used the task ELLIPSE in IRAF. On the continuum subtracted frame we ran ELLIPSE to calculate the integrated flux for a series of concentric ellipses centred on the nucleus of the galaxy and with ellipticities (ε) and position angles (PA) as obtained from the Third Reference Catalogue of Bright Galaxies (RC3; de Vaucouleurs et al. 1991). For a number of galaxies, especially in the case of irregular ones, these data were either not available or not reliable. In these cases circular apertures were used. Table 2 includes the values of ε and PA we used in our measurements. The separation between the different ellipses is a function of the pixel scale of the image used. Typically we calculated ellipses every 5 arcsec although this value was manually modified for special cases such as extremely large or small galaxies. The position of the nucleus was determined in each case from the continuum image, except for some irregular galaxies where the estimated centroid of the galaxy was used. The determination of the optimum semi-major axis of the ellipse was done using the same criterion as James et al. (2004): we consider that the photometry has converged when the measured flux between two consecutive ellipses varies by less than 0.5%. This method works efficiently for most of the galaxies in our sample. However, for a small number of galaxies (mainly irregular ones) the resulting aperture was clearly wrong. In those cases we used the D_{25} value from the RC3. The aperture determined in this way was then used on every available band. The fluxes obtained were converted from counts to $\text{erg cm}^{-2} \text{s}^{-1}$ (in the case of the $H\alpha$ band) or to magnitudes (case of R -band) using the previously calculated conversion factors.

Figures 2 to 5 show the final $H\alpha$ continuum-subtracted images. In each case, the elliptical aperture where we measured the $H\alpha$ flux is plotted on the image.

5.6 [N II] correction

Although for the sake of clarity we have only discussed $H\alpha$ fluxes, a number of our $H\alpha$ images (mainly those observed using filters wider than 35-40 \AA) are contaminated with emission from the [N II] lines at $\lambda\lambda 6548, 6584 \text{\AA}$. We estimated the contribution of the [N II] lines using the expression from Kennicutt (2008)

$$\log ([\text{N II}]/H\alpha) = \begin{cases} -0.173 \pm 0.007 M_B - \\ \quad -(3.903 \pm 0.137) & \text{if } M_B > -21 \\ 0.54 & \text{if } M_B \leq -21 \end{cases} \quad (1)$$

Helmboldt et al. (2004) provide a similar expression but using M_R instead of M_B . We decided against using this latter reference because all but two of our galaxies have measured values of M_B , while many do not have reported

M_R . For those cases where both M_B and M_R measurements were available we compared the $[\text{N II}]/\text{H}\alpha$ obtained using both methods, finding a good agreement. James et al. (2005) studied the $[\text{N II}]/\text{H}\alpha$ ratio for the $\text{H}\alpha\text{GS}$ galaxies obtaining values which are compatible with ours.

Even when it is possible to know the relation between $[\text{N II}]$ and $\text{H}\alpha$ using Equation 1, we still have to deal with the problem of the different transmissions for the $\text{H}\alpha$ and the $[\text{N II}]$ lines. Except for the broadest filters, the $\text{H}\alpha$ line is located in the region of maximum transmission of the filter (see Section 3) but the $[\text{N II}]$ lines at $\lambda\lambda 6548, 6584 \text{ \AA}$ lie at a position where the transmission is much reduced or even marginal. Solving this problem is not easy as filter shapes are often different and difficult to model. Most of the filters we used are neither Gaussian nor rectangular but a convolution of those two shapes: i.e., the transmission remains approximately constant for most of the filter width and then decays exponentially. To estimate the real transmission of the $[\text{N II}]$ lines, we took a series of filters with different FWHM (from 36 to 90 \AA) for which a transmission curve had been accurately measured. We calculated the relation between the transmission of the filter for the position of the $\text{H}\alpha$ and the $[\text{N II}]$ lines, $T_{[\text{N II}]/\text{H}\alpha}$. Figure 6 shows the values obtained. We fitted the points to a sigmoid model obtaining that $T_{[\text{N II}]/\text{H}\alpha} = 1 - 2.670 e^{-\text{FWHM}/12.385}$. Using this expression we calculated the observed ratio, $([\text{N II}]/\text{H}\alpha)_{\text{obs}}$, as $\xi_{\text{obs}} = ([\text{N II}]/[\text{H}\alpha]) \times T_{[\text{N II}]/\text{H}\alpha}$, for each galaxy (see Table 2).

5.7 Star formation rates and equivalent widths

To determine the star formation rate (SFR) from the measured fluxes we applied the following conversion from Kennicutt et al. (2009):

$$\text{SFR}(M_{\odot} \text{ yr}^{-1}) = 5.5 \times 10^{-42} L(\text{H}\alpha),$$

where $L(\text{H}\alpha)$ is the luminosity, calculated as

$$L(\text{H}\alpha)[\text{erg s}^{-1}] = 4\pi D^2 (3.086 \times 10^{24})^2 F_{\text{H}\alpha}^*,$$

with D the distance to the galaxy in Mpc and $F_{\text{H}\alpha}^*$ the absorption-corrected flux. This determination of the SFR conversion factor is based on a ‘‘Kroupa’’ initial mass function (Kroupa & Weidner 2003). The SFRs based on this estimation are lower than others calculated using older relations (for example, Kennicutt, Tamblyn & Congdon 1994 or Kennicutt 1998) by approximately a factor of 1.5 (Kennicutt et al. 2009). The distances used here (see Table 2) are the same as those indicated in C. Wilson et al. (2011, in prep.).

To correct for Galactic absorption we used, for each galaxy, the total absorption value for the R band, $A(R)$ given by NED² (see Table 2), which is based on the dust maps published by Schlegel, Finkbeiner & Davis (1998). To correct for the internal absorption, several solutions have been proposed in the literature. A number of studies over the years have adopted a constant value $A(\text{H}\alpha) = 1.1 \text{ mag}$ (Kennicutt & Kent 1983), regardless of the morphological

type or inclination of the galaxy (see, among others, Kennicutt, Bothun & Schommer 1984; Kennicutt 1998; James et al. 2004). Niklas, Klein & Wielebinski (1997), however, reported that the value for $A(\text{H}\alpha)$ might be as low as 0.8 mag and James et al. (2005) found values as low as 0.4 mag for some early-type galaxies. On the other hand, Helmboldt et al. (2004) proposed an expression to calculate $A(\text{H}\alpha)$ in function of the absolute R magnitude of the galaxy, M_R . This expression takes the form

$$\log A(\text{H}\alpha) = (-0.12 \pm 0.048) M_R + (-2.5 \pm 0.96). \quad (2)$$

We used this equation to calculate the internal absorption of the galaxies in our sample. Unfortunately, not all of our galaxies have been accurately measured in the R -band. For those galaxies we overcame this problem by selecting different values of $A(\text{H}\alpha)$ according with the type of galaxy studied. Specifically, we used

$$A(\text{H}\alpha) = \begin{cases} 0.3 & \text{if } M_B \leq -16, \\ 1.1 & \text{otherwise,} \end{cases}$$

which are in good agreement with the values yielded by Equation 2. Our method provides absorption values which are somewhat lower than those often used in previous studies of the same type. This explains that the mean SFR values we obtain here are lower than those frequently found in the literature (see Section 6.1).

The equivalent width (EW) of the $\text{H}\alpha$ line is a direct and widely used method to estimate the intensity of the line as compared to the emission of the underlying continuum. As is usual in the literature, we calculate the EW by forming a rectangle with the height of the continuum under the line and finding the width such that the area of the rectangle matches the area of the spectral line. In practice, we calculated the EW of our galaxies applying two different methods. First, we used the scale factor obtained during the continuum subtraction process, together with the FWHM of the $\text{H}\alpha$ narrow-band filter. The equivalent width can then be determined as

$$\text{EW} = \frac{\text{CPS}_{\text{H}\alpha}}{k (\text{CPS}_{\text{cont}} - \text{CPS}_{\text{H}\alpha}) / \text{FWHM}_{\text{H}\alpha}}, \quad (3)$$

where k is the scale factor and CPS_x are the counts per second of the $\text{H}\alpha$ and continuum bands, with $\text{CPS}_{\text{H}\alpha}$ already corrected for $[\text{N II}]$ contamination and internal absorption. We found that this method yielded very accurate results, and our EW measurements are determined mainly using this system. Unfortunately, some of the literature data sets included neither the continuum scale factor, nor the original $\text{H}\alpha$ image, which is necessary to perform our own continuum subtraction. In these cases, we used an alternative method. The EW can be simply calculated as the ratio between the $\text{H}\alpha$ continuum subtracted flux and the flux density in the continuum band. As our continuum images were obtained using standard R -band filters, we converted from R magnitudes to flux densities using the parameters which define the system (we mostly used Cousins R filters with an effective wavelength of 6400 \AA and a zero point of 3080 Jy; Cox 2000). As this method relies on physical measurements (with the uncertainties associated with every calibration) and not all the R -band filters are identical, we found that the EWs determined in this way are less accurate.

Finally, we used the EW values from the literature

² The NASA/IPAC Extragalactic Database; <http://nedwww.ipac.caltech.edu/>

where available and perform the calculations described above in the rest of the cases. Section 7 compares our EW values with those in the literature to study the quality of our measurements. Table 2 indicates the final SFR and EW measurements for each galaxy and, for the latter, the method used for the calculation or the source of the value.

5.8 Uncertainties

Several factors contribute to the final uncertainties of the SFR and EW measurements we present here. First, we estimated the uncertainty associated with the flat-fielding correction. Although this value changes depending on the instrument and even with the specific conditions of the night, we find the typical uncertainty to be well in the range 1–2% with some values as high as 5%.

Uncertainties in the zero point calibrations during photometric nights have typical values of 2%. We used several galaxies observed both in photometric and non-photometric conditions to estimate uncertainties associated with the latter. We find that, even in the worst cases, the uncertainty in the calibration is never higher than 5%. Similarly, the uncertainty in the flux measurement is typically below 1%, with some extreme cases as high as 5% for a few very weak galaxies.

For the uncertainties associated with the distances, we found that the values given in NED were frequently unreliable and underestimated the real uncertainty. Except for a few galaxies with quality distance measurements, we adopted a typical uncertainty of 20% in the estimated distance to the galaxy.

Along with the distance, the main contribution to the uncertainty for the vast majority of our galaxies is the continuum subtraction. As a galaxy is an extended object there is often not a single scale factor applicable to the whole image. This implies that any method aimed to measure the scale factor used in the continuum subtraction is affected by a certain amount of subjectivity. To measure the uncertainty associated with the removal of the continuum we selected 10 galaxies of different morphological types, SFRs and EWs. For each galaxy we produced new continuum subtracted frames using both the first scale factor which led to a clearly under-subtracted image and the first producing an over-subtracted one. Using these extreme values as a reference, we estimated that the uncertainty due to the scale factor is in the range from 5 to 15% for most galaxies. Unlike some previous studies (James et al. 2004; Kennicutt 2008) which reported a correlation between EW and the uncertainty of the scale factor, we find no trend whatsoever in this sense.

Without considering the problem of distance (i.e., taking into account only those uncertainties intrinsic to the quality of the images) we find that the median uncertainty in flux for all our galaxies is $\sim 18\%$. This value is in very good agreement with recent surveys using similar techniques. For instance, Kennicutt (2008) obtained a median uncertainty (also using the flux measurements) of $\sim 16\%$ while James et al. (2004) reported $\sim 18\%$.

5.9 Image availability

With the publication of this article, the H α and R -band images for all the galaxies in our sample are made publicly available through the Strasbourg astronomical Data Center (CDS).

6 RESULTS

Table 2 shows the main results of the photometry of our 156 galaxies as well as their associated uncertainties. The column description is as follows.

Column (1): the name of the galaxy in the designation used in this work.

Column (2): the morphological class of the galaxy as catalogued in NED.

Column (3): the recession velocity used to calculate the Doppler shift of the H α line, obtained from NED.

Column (4): the distance to the galaxy considering $H_0 = 70.5 \text{ km s}^{-1} \text{ Mpc}^{-1}$, $\Omega_M = 0.27$ and $\Omega_{\text{vac}} = 0.73$ and using a model that takes into account the Virgo infall velocity (Mould et al. 2000). For the galaxies belonging to the Virgo subsample we have adopted a distance of $16.7 \pm 1.1 \text{ Mpc}$ (Mei et al. 2007). Additionally, we used the distances from Freedman et al. (2001) for NGC 925, NGC 2403, NGC 3031, NGC 3198, NGC 3351, NGC 3627 and NGC 4725; Karachentsev et al. (2002) for NGC 2976, NGC 4236, UGC 04305 and UGC 08201; Tonry et al. (2001) for NGC 584, NGC 855, NGC 4594, NGC 4736, NGC 4826 and NGC 5194; Karachentsev et al. (2004) for NGC 628; Dalcanton et al. (2009) for IC 2574; Macri et al. (2001) for NGC 2841; Leonard et al. (2002) for NGC 3184; and Seth, Dalcanton & de Jong (2005) for NGC 4631. For NGC 3034, PGC 023521, UGC 05139, UGC 05336 and UGC 05423 we used the same distance as NGC 3031 (Freedman et al. 2001).

Columns (5): the major and minor axis of the galaxy in arcmin.

Column (6): the B -band absolute magnitude derived from the apparent magnitude in the RC3 catalogue and the redshift of each galaxy. The luminosity distance, necessary to derive the absolute magnitude, was calculated using a model which takes $H_0 = 70.5$, $\Omega_M = 0.27$ and $\Omega_{\text{vac}} = 0.73$. In a few cases (marked in the table) no B -band magnitude was available in RC3 and we use the closest match from the photometric data points gathered in NED for each galaxy. For PGC 140287 we used the B -band magnitude from LEDA (Paturel et al. 2003).

Column (7): the scale factor applied to the continuum image during the continuum subtraction (see Section 5.2).

Column (8): the estimated contribution of the H α line to the flux measured in the continuum filter.

Column (9): the total flux of the galaxy in the H α line in units of $\text{erg cm}^{-2} \text{ s}^{-1}$. The area used to perform the photometry has been selected as indicated in Section 5.5. This flux has not been corrected for any kind of absorption or [N II] contribution.

Column (10): the total absorption for the galaxy, A_T , in mag. This value comprises the Galactic foreground absorption in the R band, $A(R)$, for the position of the galaxy taken from Schlegel, Finkbeiner & Davis (1998), and the internal absorption, $A(H\alpha)$ calculated as explained in Section 5.7.

Column (11): the estimated ratio $\xi_{\text{obs}} = ([\text{N II}]/\text{H}\alpha)_{\text{obs}}$ calculated as explained in Section 5.6.

Column (12): the $\text{H}\alpha$ luminosity of the galaxy, in erg s^{-1} . This value has been corrected for absorption using A_T and for the contribution of the $[\text{N II}]$ lines.

Column (13): the star formation rate for the galaxy in units of $M_{\odot} \text{ yr}^{-1}$ (corrected for absorption and $[\text{N II}]$).

Column (14): the equivalent width, in Ångström, calculated as described in Section 5.7. The method used for the calculation is indicated in parenthesis meaning (1) that the equivalent width is derived from the scale factor used for the continuum subtraction as in Equation (3); (2) that the equivalent width is derived from the fluxes of the images; and (3) that we used the value from the literature. In the latter case, the reference is always the same as the one listed in Table 1 for the corresponding galaxy.

6.1 Star formation rate measurements

Figure 7 shows the correlation between the SFR (in units of solar masses per year) and the B -band absolute magnitude, $M(B)$. Our four subsamples (field, small Virgo, and large and small SINGS galaxies) are plotted separately in Figure 8 to consider the individual properties and possible biases of these subsets.

We find an expected trend, with brighter galaxies hosting a higher amount of star formation. This behavior has been previously reported by several authors such as Tresse & Maddox (1998), who used spectroscopic $\text{H}\alpha$ data from a sample of galaxies at $z \sim 0.2$, and more recently Knapen & James (2009) (their Figure 2), using the sample of the $\text{H}\alpha\text{GS}$ survey (see also Section 7). Figure 6 in Lee et al. (2009b), who use data of ~ 300 galaxies from 11HUGS (Kennicutt et al. 2008), shows a similar trend for galaxies with $M(B) \leq -15$ (for very faint galaxies, $M(B) > -15$, the SFR seems to drop suddenly to values below $10^{-4} M_{\odot} \text{ yr}^{-1}$). This same result is found by Karachentsev & Kaisin (2010) using 435 galaxies in a volume-limited region of 10 Mpc. The slope of our least squares fit is -0.29 , somewhat higher than the value of -0.41 found by Lee et al. (2009b).

The top right corner in Figure 7 is exclusively occupied by galaxies from the SINGS large subsample. The galaxy with the highest SFR in our sample ($11.31 M_{\odot} \text{ yr}^{-1}$) is NGC 4254 (Messier 99). In the other extreme of the plot we find two small irregular galaxies (PGC 23521 and IC 3105), both with a SFR below $10^{-3} M_{\odot} \text{ yr}^{-1}$.

It is interesting to consider the behavior of the four different subsamples which compose our sample. Field galaxies in the NGLS sample are distributed uniformly along a wide range of $M(B)$, which is expected as they have been selected based on their H I emission and not on their optical luminosity. The same can be said for the galaxies contained in the SINGS subsamples. The Virgo cluster subsample, however, contains galaxies with $M(B)$ well constrained in the range $[-17, -22]$ magnitudes.

We calculate the median³ SFR for all the galaxies in our sample as $0.21^{+0.37}_{-0.12} M_{\odot} \text{ yr}^{-1}$. This value is consistent

with those of the different subsamples ($0.22^{+0.46}_{-0.12} M_{\odot} \text{ yr}^{-1}$ for the field galaxies, $0.11^{+0.55}_{-0.01}$ for the SINGS small galaxies, and $0.09^{+0.21}_{-0.05} M_{\odot} \text{ yr}^{-1}$ in the case of Virgo galaxies). Not unexpectedly, the SINGS large subsample shows a higher median SFR ($1.04^{+1.77}_{-0.31} M_{\odot} \text{ yr}^{-1}$) as it is mainly populated by spiral galaxies (see Figure 1) with high FIR luminosities and, thus, large SFR (see, for example, Calzetti & Kennicutt 2009). On the other hand, the large uncertainty in the SINGS median value shows that this subsample contains galaxies with a large range of SFRs. The median value for the whole sample is lower than those of other studies in the literature (see Section 7). We attribute this difference to the fact that the internal absorptions we calculate here (see Section 5.7) are, in general, lower than those previously used. For example, if we adopt a typical, constant, $A(\text{H}\alpha) = 1.1$ mag value for the internal absorption, the median SFR becomes $0.38^{+0.60}_{-0.24} M_{\odot} \text{ yr}^{-1}$, more consistent with other values found in the literature.

To study the range of SFRs in the different subsamples, we binned the data into 0.5 magnitude bins and calculated the range (the difference between the maximum and minimum values) for each bin. We find maximum ranges between 2.0 and 2.9 dex for the field, SINGS large and Virgo subsamples. In every instance, the peak of maximum range is located around $M(B) = 20.0$ magnitudes. On the other hand, the range of values in the SINGS small sample, as can easily be appreciated from Figure 8, is much lower, with a maximum value of 1.3 dex. The same results, for the whole sample, are shown in the lower plot of Figure 7 as the normalized root mean square distance of each data point to the best fit. The largest dispersion occurs between $M(B) \sim -17$ and $M(B) \sim -20$.

Figure 9 presents the measured SFR as a function of the Hubble stage of each galaxy. We find that most of the star forming members of our sample are spiral galaxies with stage $T \sim 4$ (Sb/Sbc). A secondary peak is found for late-type spirals ($T \sim 7$). These results are in good agreement with previous studies (see, for example, James et al. 2004). While there is an expected decline in the SFR toward late-type and irregular galaxies the same is not true for very early ellipticals. A slight increase in SFR appears to exist for early-type galaxies ($T \leq -2$). This behavior seems to contradict the widely accepted theory that elliptical galaxies have exhausted most of their gas reservoirs and do not form stars. A series of recent studies (see, e.g., Sarzi et al. 2006, 2010) has shown that these galaxies may contain more ionized gas than traditionally thought. However, this may be mostly due to internal shocks and not necessarily to the star formation processes occurring in the galaxy. The number of early-type galaxies in our sample is, unfortunately, not large enough to make a definitive statement in this debate.

Figure 10 shows Σ (the SFR surface density, in units of $M_{\odot} \text{ yr}^{-1} \text{ kpc}^{-2}$) of each galaxy plotted against the corresponding SFR. To compute the size of the galaxy we used the optical size D_{25} from RC3 and converted it to kpc using the distance from Table 2. We find that galaxies with higher Σ tend to host larger amounts of star formation, with a regression fit of $\log(\Sigma) = 0.37 \log(\text{SFR}) - 2.28$. Knapen &

the maximum and minimum median values obtained as the upper and lower uncertainties.

³ The uncertainties are calculated by selecting a random subsample from the complete set of SFR values and calculating its median. We repeated this process a thousand times and selected

James (2009) (their Figure 4) published a similar plot for the galaxies in the H α GS sample. In their case, however, Σ remains constant for SFRs lower than $\sim 1 M_{\odot} \text{ yr}^{-1}$.

As in the case of the SFRs, the result for Σ shows a wide dispersion, with values ranging across three orders of magnitude. This can be said for each one of the subgroups which make up our sample.

We also compared our SFRs with the $M(K)$ magnitudes of the galaxies in our sample, following the same process as explained above. We find that the general behavior of the plotted data does not change when using $M(K)$ instead of $M(B)$ for the SINGS Large and Small and for the Virgo subsamples. In the case of the Field subsample, the data show a higher dispersion when using $M(K)$.

6.2 Equivalent widths

Figures 11 and 12 show, globally and separated by subsample, the EWs of the galaxies in our sample as a function of their absolute magnitude in the B -band.

We find that our EW values are distributed over almost two orders of magnitude, with a median value of $27_{-20}^{+33} \text{ \AA}$. The different subsamples are consistent with this global result showing median values that range between $21_{-6}^{+37} \text{ \AA}$ (SINGS Large) and $31_{-21}^{+47} \text{ \AA}$ (SINGS Small).

The relation between EW and $M(B)$ is basically flat, which indicates that, in most cases, an enhanced rate of star formation comes with a similar increase in the continuum emission produced by evolved stars. This behavior has been suspected for almost three decades (see, for example Kennicutt & Kent 1983) and confirmed in recent studies such as Gavazzi et al. (1998) (their Figure 5), James et al. (2004) and Knapen & James (2009), the latter two using H α GS data. They also detected (see Figure 3 in Knapen & James 2009) a significant number of very luminous galaxies with low EW. Their hypothesis that these galaxies are, in their majority, massive elliptical and early-type objects with almost no star formation is also supported by Lee et al. (2007) and Lee et al. (2009a), who showed that this result is also valid when comparing the EW with the rotation velocity of the galaxies. The downturn in EW is not as conspicuous in our sample as in these studies, but it seems to exist for $M(B) < -17$ mag, a region populated mostly by field and Virgo galaxies.

Four out of the ten highest EW values are field galaxies, the top one being PGC 43211, a spheroidal galaxy with an EW of 880 \AA . Almost no SINGS galaxies are found among the galaxies with the highest EW values. This indicates that, while these other galaxies contain SFRs usually above the mean for field galaxies, their masses of old stars are proportionally high. We also find that two of the lowest EW measurements, with EWs below 5 \AA , are intermediate-type (Sab and Sb) galaxies from the SINGS large subsample. NGC 4470, of Sa class and $\text{EW} \sim 0.1 \text{ \AA}$, is the galaxy with the lowest EW in our sample.

Figure 13 (which shows the EW plotted as a function of the Hubble stage) does not show any significant correlation between EW and morphological type except, maybe, a certain increase of the EW values for galaxies of Sb type and later.

7 OTHER STUDIES

Our current study is one of many surveys based on H α as a tracer of massive stars. In the last decade alone, many samples have been observed and reduced using techniques similar to those presented here (e.g., Gavazzi et al. 2002; Boselli et al. 2002; Gavazzi et al. 2003; Hunter & Elmegreen 2004; James et al. 2004; Meyer et al. 2004; Verdes-Montenegro et al. 2005; Gavazzi et al. 2006; Kennicutt et al. 2008). Notwithstanding the common goal of characterizing massive star formation in the local Universe, these samples have used different selection criteria and thus all suffer from different biases. Some of the most representative SFR studies in recent years are addressed below and their results compared with some of ours.

The GOLDMine project⁴ has observed and collected data for over 3000 galaxies belonging to, among others, the Coma supercluster and the Virgo, Cancer and Hercules clusters. This data includes H I, IR and optical continuum measurements, as well as spectral observations. Two large sets of original H α data have been published by Gavazzi and collaborators. Gavazzi et al. (2002) observed 369 galaxies with types later than S0a in the Virgo and Coma/A1367 clusters. Gavazzi et al. (2006) extended the sample with some 273 galaxies in the Virgo and Cancer clusters and in the Coma/A1367 and Hercules superclusters.

We have already introduced the SINGS survey (Kennicutt et al. 2003) in Section 2. Aimed to characterize the infrared emission in the local Universe, it includes 75 galaxies within 30 Mpc from elliptical to irregular and with a large range of SFRs. The SINGS team has obtained H α and continuum broad-band imaging for the whole sample but, although the images have been made public, no catalogue of galaxy-integrated SFRs or EWs has been published.

Our survey has also made extensive use of the H α GS work (James et al. 2004), which observed 334 galaxies extracted from the Uppsala Galaxy Catalogue (Nilson 1973) of types later than S0a and with $m(B) \lesssim 14.5$ in the Palomar observatory plates. The targets were selected to include galaxies with recession velocities from 0 to 3000 km s^{-1} . As in our case, they found a clear trend between SFRs and absolute magnitudes and an apparent lack of correlation of EW with luminosity and morphological type (see also Knapen & James 2009).

Although it is generally accepted that most of the massive star formation in galaxies occurs in the spiral arms of late-type galaxies, some authors have questioned the necessity of a spiral density wave to achieve an important amount of star formation (see, for example, Hunter, Gallagher & Rautenkranz 1982, Elmegreen & Elmegreen 1986; Elmegreen 2011 and references therein). Hunter & Elmegreen (2004, hereafter HE04) focused on observing a sample of 142 mainly irregular galaxies. Some Sm and blue compact dwarfs (BCD) were observed for comparison. The sample of irregular galaxies was compiled from the Fisher & Tully (1975) H I atlas of galaxies and thus includes only galaxies containing gas. They found H α emission in over 80 of their 96 irregular galaxies and in all the Sm and dwarf (BCD) galaxies except one. The SFRs are low, with a mean value of $0.1 M_{\odot} \text{ yr}^{-1}$ and a maximum of $0.5 M_{\odot} \text{ yr}^{-1}$.

⁴ <http://goldmine.mib.infn.it/>

The Survey for Ionization in Neutral-Gas Galaxies (SINGG) aims to observe 468 galaxies selected from the HI Parkes All Sky Survey (HIPASS, Meyer et al. 2004) with peak flux densities above 0.05 Jy. The galaxies have been selected to cover a range of $\log(M_{\text{HI}}/M_{\odot})$ from 8 to 10.5. The most recent data release we have been able to find is the one published by Hanish et al. (2006) which contains observations and derived values for 111 galaxies. Among those, every galaxy with $M_{\text{HI}} > 3 \times 10^7 M_{\odot}$ has also been detected in H α , thus constraining the amount of gas necessary to trigger global star formation in a galaxy.

Kennicutt et al. (2008) (hereafter RCK08) have made, along with H α GS, one of the first attempts to observe a volume-limited sample of galaxies using H α . Two main factors make this a difficult task: firstly, the mapping of galaxies (especially irregular ones) in the local universe is currently not complete; and secondly, even for the known galaxies, the high uncertainties in the distances make it difficult to define the set of galaxies within a certain radius. While these problems cannot be solved at the present moment, RCK08 managed to observe a sample of 261 S and Irr galaxies within 11 Mpc with galactic latitudes above 20° and $m(B) \leq 15$ magnitudes, and an additional set of 175 galaxies with lower galactic latitudes or fainter. This sample is shared with other legacy surveys to be carried out using *Galax* and *Spitzer* which will provide interesting complementary information in the near and far UV and in the IR (3.6 to 160 μm).

Finally, Karachentsev & Kaisin (2010) presented a study of 52 galaxies observed in H α as part of a larger survey aimed to study a sample of galaxies in the Local Volume (207 galaxies within 10 Mpc). An important number of the galaxies observed belong to the Maffei 2/IC 342 complex. The sample contains galaxies of all morphological types but with prevalence of irregular galaxies.

Figure 14 shows a series of histograms comparing the number of galaxies versus the morphological class (in the form of Hubble stages) for our sample and the different samples presented above. Most of these studies lack a good representation (or any representation at all) of early-type galaxies. While this is a natural thing in surveys like HE04, aimed to study irregular galaxies specifically, it indicates that a general bias towards late-type (S0 and later) galaxies dominates the literature of H α surveys. This comparison also shows that HI-selected samples, as SINGG and our own sample, span a wider range of morphological classes.

Figures 15 to 17 present similar histograms for distance, SFR and EW respectively. SINGS does not provide measurements of H α fluxes (and, consequently, L(H α) and SFR) or EW. EWs for HE04 and RCK08 are not available in the public catalogues. The EWs from RCK08 we use to complete our data (see Section 5.7) have been taken directly from the headers of the images, but they are not included in the catalogue published in CDS.

The distance histograms show that most of the galaxies observed to date with resolved H α imaging are closer than 50 Mpc even when, among the surveys discussed here, only RCK08 and H α GS include the distance as a selection criterion. The exceptions are SINGG, which observed galaxies as far as 80 Mpc, and Gavazzi et al. (2002, 2006), most of whose galaxies are located at the specific distances of

the clusters observed ($\sim 100 \text{ Mpc}^5$ for the Coma Cluster, 16.4 to 22.9 Mpc for the Virgo Cluster –Mei et al. 2007, and $> 150 \text{ Mpc}^5$ for the Hercules Cluster). The galaxies in our sample have a mean distance of 15.8 Mpc, similar to those in the rest of the surveys, except for RCK08 with 6.8 Mpc and Gavazzi et al. (2002, 2006) with $\sim 50 \text{ Mpc}$.

All the SFR histograms shown in Figure 16 tell a similar story, with most galaxies hosting small amounts of star formation (less than $0.5 M_{\odot} \text{ yr}^{-1}$). The number of galaxies with rates of star formation higher than $\sim 1 M_{\odot} \text{ yr}^{-1}$ drops dramatically in every case. Gavazzi et al. (2002) show a significant number of galaxies with high SFRs (up to $\sim 6 M_{\odot} \text{ yr}^{-1}$). This may be due to a systematic overestimation of their H α fluxes, since the distribution of morphological types (see Figure 14) does not indicate an overwhelming presence of highly efficient star forming galaxies. Eleven of the SINGG galaxies present SFRs higher than $10 M_{\odot} \text{ yr}^{-1}$ with the extreme case of M 83 with a SFR of $145 M_{\odot} \text{ yr}^{-1}$. Those cases are suspect, as such behaviour is not found in any of the other surveys. Hunter & Elmegreen (2004) and Karachentsev & Kaisin (2010) show virtually no SFRs above $0.5 M_{\odot} \text{ yr}^{-1}$, which can be attributed to the fact that their samples are mostly or totally composed of irregular galaxies with very low SFRs.

A similar behaviour is found (Figure 17) for the EW of the SINGG galaxies. The large number of galaxies with very high EW ($\gtrsim 140 \text{ \AA}$, with a maximum value of 450 \AA for the peculiar galaxy NGC 5253) is surprising. These exceptions notwithstanding, the comparison between the different histograms show a similar pattern, with mean EWs between 20 and 35 \AA (in the case of SINGG the mean is 50.7 \AA but this is mainly due to some extremely high values).

Figure 18 shows the comparison between our SFR data and the values found in the literature. Except for a global offset, which can be explained by the different internal absorption used in this work (see Section 6.1), the global agreement is good, with a fit of slope 0.90 and a correlation coefficient $R^2 = 0.82$. This good agreement is also valid if we compare our data with each individual study. We find a slope of 0.95 and $R^2 = 0.98$ for H α GS, 1.01 and 0.88 for RCK08, 1.35 and 0.92 for GM and 0.86 and 0.58 for SINGS. The excellent fit in the case of H α GS is especially important as our aperture selection and flux measurement methods are essentially the same. As we have already commented, the SINGS team has not published SFR measurements based on their H α images. Kennicutt et al. (2003) gives the SFR values from the IRAS catalogue (Fullmer & Lonsdale 1989), based not on H α observations but on IR measurements from 60 to 100 μm . This explains that the fit using SINGS values is worse than those using the other points. In any case, these comparisons show that the differences between our SFR values and those in the literature lie well within the typical errors for this kind of measurement, whatever the methods applied and the specific luminosity-to-SFR constant used in each study.

⁵ From NED

8 CONCLUSIONS AND FUTURE WORK

We have presented new H α and *R*-band observations of 72 out of the 156 galaxies sampled in the JCMT Nearby Galaxies Legacy Survey. This sample is partly H I-selected and aims to include galaxies within 25 Mpc with morphological types from E to Irr. The sample is largely formed by field galaxies but also includes targets from the SINGS survey and a fair amount of Virgo cluster galaxies.

For the remaining 84 galaxies we have compiled images from the literature. We processed all these data using well-defined methods and criteria and present H α fluxes, SFR and EW measurements for the whole sample. With this article, we make our new data publicly available.

We analyzed the data reaching, among others, the following conclusions:

- (i) The SFR shows a clear increasing trend when plotted against $M(B)$. This trend is dependent on the subsample considered, with a better fit for the field and SINGS Small galaxies than for those in the SINGS Large or Virgo subsamples.
- (ii) We find a median SFR across our sample of $0.2 M_{\odot} \text{ yr}^{-1}$, while in the case of the galaxies in the SINGS Large subsample the median SFR is $1 M_{\odot} \text{ yr}^{-1}$.
- (iii) The SFR values range across almost three orders of magnitude, except in the case of the SINGS Small galaxies where the values are confined to a range of one order of magnitude.
- (iv) The SFR of our sample peaks for Sb/Sb-c galaxies ($T \sim 4$) with a secondary peak for late-type Sc galaxies ($T \sim 7$).
- (v) We plotted EW versus $M(B)$ confirming that the relation between EW and luminosity is practically flat. This is also valid when comparing the EWs with the morphological type, although a trend seems to exist leading to slightly higher EW for late-type and irregular galaxies.
- (vi) The comparison of our SFR values with those found in the literature shows an excellent agreement for SFR, well within the typical margins of error.

This paper has presented our H α line observations, as well as a general study of the star forming properties of the sample and a comparison with previous similar studies. However, this is only the first step towards the more ambitious goal of comparing the star formation in the galaxies of the sample with their gas content, both atomic and molecular. $^{12}\text{CO } J = 3 - 2$ maps of the whole sample are available as a part of the NGLS observations carried out with HARP-B in the JCMT, thus allowing a global comparison between L(H α) and L(CO) for all our galaxies. This will be the largest study correlating the star formation with the amount of warm, dense molecular hydrogen present in a galaxy and may be key to understanding the physics involved in large-scale star formation in the nearby universe.

Furthermore, the rich variety of literature data available for a large part of our sample, from IR data obtained with *Spitzer* to FUV from *GALEX* as well as H I from a variety of sources (THINGS: Walter et al. 2008; WHISP: van der Hulst 2002; etc.) and CO $J = 1 - 0$ and $J = 2 - 1$ (e.g., HERACLES: Leroy et al. 2009) allows us to study the behavior of the different gas and dust components over the complete morphological range.

Finally, the JCMT NGLS has been awarded guaranteed

time to observe the whole sample using SCUBA-2 to obtain continuum imaging in 450 and 850 μm and study the cold dust within galaxies with an unprecedented sensitivity and resolution. These data will also be compared to the current H α and other data in forthcoming papers.

ACKNOWLEDGMENTS

We thank Elias Brinks, Jen Golding, Frank Israel, Robert C. Kennicutt and Paul van der Werf for their comments and useful suggestions during the preparation of this manuscript. We also thank Eduardo González for his help during the initial steps of the INT image reduction. Finally, we thank Santiago Erroz Ferrer and Elena Mohd-Noh Velastín for the observation and reduction of the images of NGC 4504 with the NOT. The James Clerk Maxwell Telescope is operated by the Joint Astronomy Centre on behalf of the Science and Technology Facilities Council of the United Kingdom, the Netherlands Organisation for Scientific Research, and the National Research Council of Canada. Based on observations obtained with the WHT, the INT, and the NOT, operated on the island of La Palma by the Isaac Newton Group of Telescopes, and jointly by Denmark, Finland, Iceland, Norway and Sweden, in the Spanish Observatorio del Roque de los Muchachos of the Instituto de Astrofísica de Canarias. We acknowledge the use of the Hiltner telescope at the MDM Observatory operated by the University of Michigan, Dartmouth College, the Ohio State University, Columbia University, and Ohio University. This research has made use of the NASA/IPAC Extragalactic Database (NED) which is operated by the Jet Propulsion Laboratory, California Institute of Technology, under contract with the National Aeronautics and Space Administration.

REFERENCES

- Alonso O., García-Dabó C. E., Zamorano J., Gallego J., Rego M., 1999, *ApJS*, 122, 415
- Bendo G. J. et al., 2010, *MNRAS*, 402, 1409
- Boselli A., Iglesias-Páramo J., Vílchez J. M., Gavazzi G., 2002, *A&A*, 386, 134
- Calzetti D., Kennicutt R. C., 2009, *PASP*, 121, 937
- Calzetti D. et al., 2007, *ApJ*, 666, 870
- , 2010, *ApJ*, 714, 1256
- Cox A. N., 2000, *Allen's astrophysical quantities*, Cox, A. N., ed.
- Dalcanton J. J. et al., 2009, *ApJS*, 183, 67
- de Vaucouleurs G., de Vaucouleurs A., Corwin, Jr. H. G., Buta R. J., Paturel G., Fouque P., 1991, *Third Reference Catalogue of Bright Galaxies*. (New York : Springer)
- Draper P. W., Berry D. S., Jenness T., Economou F., 2009, in *ASP Conf. Series*, Vol. 411, *Astronomical Data Analysis Software and Systems XVIII*, D. A. Bohlender, D. Durand, & P. Dowler, ed., p. 575
- Elmegreen B. G., 2011, in press (ArXiv:1101.3109)
- Elmegreen B. G., Elmegreen D. M., 1986, *ApJ*, 311, 554
- Fisher J. R., Tully R. B., 1975, *A&A*, 44, 151
- Freedman W. L. et al., 2001, *ApJ*, 553, 47

- Fullmer L., Lonsdale C. J., 1989, JPL D-1932, Version 2
- Gallego J., Zamorano J., Aragon-Salamanca A., Rego M., 1995, *ApJL*, 455, L1
- Gautier, III T. N., Fink U., Larson H. P., Treffers R. R., 1976, *ApJL*, 207, L129
- Gavazzi G., Boselli A., Cortese L., Arosio I., Gallazzi A., Pedotti P., Carrasco L., 2006, *A&A*, 446, 839
- Gavazzi G., Boselli A., Donati A., Franzetti P., Scodreggio M., 2003, *A&A*, 400, 451
- Gavazzi G., Boselli A., Pedotti P., Gallazzi A., Carrasco L., 2002, *A&A*, 396, 449
- Gavazzi G., Catinella B., Carrasco L., Boselli A., Contursi A., 1998, *AJ*, 115, 1745
- Hanish D. J. et al., 2006, *ApJ*, 649, 150
- Helmboldt J. F., Walterbos R. A. M., Bothun G. D., O’Neil K., de Blok W. J. G., 2004, *ApJ*, 613, 914
- Hopkins A. M., Connolly A. J., Szalay A. S., 2000, *AJ*, 120, 2843
- Hunter D. A., Elmegreen B. G., 2004, *AJ*, 128, 2170
- Hunter D. A., Gallagher J. S., Rautenkranz D., 1982, *ApJS*, 49, 53
- Irwin J. A. et al., 2011, *MNRAS*, 410, 1423
- James P. A. et al., 2004, *A&A*, 414, 23
- James P. A., Shane N. S., Knapen J. H., Etherton J., Percival S. M., 2005, *A&A*, 429, 851
- Karachentsev I. D. et al., 2002, *A&A*, 383, 125
- Karachentsev I. D., Kaisin S. S., 2010, *AJ*, 140, 1241
- Karachentsev I. D., Karachentseva V. E., Huchtmeier W. K., Makarov D. I., 2004, *AJ*, 127, 2031
- Kennicutt R. C., 2008, *Pathways Through an Eclectic Universe ASP Conference Series*, 390, 149
- Kennicutt R. C. et al., 2003, *Publ. Astron. Soc. Pac.*, 115, 928
- Kennicutt R. C. et al., 2009, *ApJ*, 703, 1672
- Kennicutt, Jr. R. C., 1998, *ApJ*, 498, 541
- Kennicutt, Jr. R. C., Bothun G. D., Schommer R. A., 1984, *AJ*, 89, 1279
- Kennicutt, Jr. R. C., Kent S. M., 1983, *AJ*, 88, 1094
- Kennicutt, Jr. R. C., Lee J. C., Funes, José G. S. J., Sakai S., Akiyama S., 2008, *ApJS*, 178, 247
- Kennicutt, Jr. R. C., Tamblyn P., Congdon C. E., 1994, *ApJ*, 435, 22
- Knapen J. H., 1992, PhD thesis, Univ. La Laguna, Tenerife, Spain
- Knapen J. H., James P. A., 2009, *ApJ*, 698, 1437
- Knapen J. H., Stedman S., Bramich D. M., Folkes S. L., Bradley T. R., 2004, *A&A*, 426, 1135
- Kroupa P., Weidner C., 2003, *ApJ*, 598, 1076
- Landolt A. U., 1992, *AJ*, 104, 340
- Lanzetta K. M., Yahata N., Pascarella S., Chen H.-W., Fernández-Soto A., 2002, *ApJ*, 570, 492
- Lasker B. M. et al., 2008, *AJ*, 136, 735
- Lasker B. M., Sturch C. R., McLean B. J., Russell J. L., Jenkner H., Shara M. M., 1990, *AJ*, 99, 2019
- Lee J. C. et al., 2009a, *ApJ*, 706, 599
- Lee J. C., Kennicutt R. C., Funes, José G. S. J., Sakai S., Akiyama S., 2007, *ApJL*, 671, L113
- Lee J. C., Kennicutt, Jr. R. C., Funes S. J. G., Sakai S., Akiyama S., 2009b, *ApJ*, 692, 1305
- Leonard D. C. et al., 2002, *AJ*, 124, 2490
- Leroy A. K. et al., 2012, in press (ArXiv:1202.2873)
- , 2009, *AJ*, 137, 4670
- Macri L. M., Stetson P. B., Bothun G. D., Freedman W. L., Garnavich P. M., Jha S., Madore B. F., Richmond M. W., 2001, *ApJ*, 559, 243
- Madau P., Ferguson H. C., Dickinson M. E., Giavalisco M., Steidel C. C., Fruchter A., 1996, *MNRAS*, 283, 1388
- Massey P., Strobel K., Barnes J. V., Anderson E., 1988, *ApJ*, 328, 315
- Mei S. et al., 2007, *ApJ*, 655, 144
- Meurer G. R. et al., 2006, *ApJS*, 165, 307
- Meyer M. J. et al., 2004, *MNRAS*, 350, 1195
- Mould J. R. et al., 2000, *ApJ*, 529, 786
- Nagamine K., Ostriker J. P., Fukugita M., Cen R., 2006, *ApJ*, 653, 881
- Neufeld D. A., Yuan Y., 2008, *ApJ*, 678, 974
- Niklas S., Klein U., Wielebinski R., 1997, *A&A*, 322, 19
- Nilson P., 1973, *Uppsala general catalogue of galaxies*, Nilson, P., ed.
- Oke J. B., 1990, *AJ*, 99, 1621
- Paturel G., Petit C., Prugniel P., Theureau G., Rousseau J., Brouty M., Dubois P., Cambrésy L., 2003, *A&A*, 412, 45
- Sánchez-Gallego J. R. et al., 2011, *A&A*, 527, A16
- Sarzi M. et al., 2006, *MNRAS*, 366, 1151
- , 2010, *MNRAS*, 402, 2187
- Schlegel D. J., Finkbeiner D. P., Davis M., 1998, *ApJ*, 500, 525
- Seth A. C., Dalcanton J. J., de Jong R. S., 2005, *AJ*, 129, 1331
- Stone R. P. S., 1977, *ApJ*, 218, 767
- Tonry J. L., Dressler A., Blakeslee J. P., Ajhar E. A., Fletcher A. B., Luppino G. A., Metzger M. R., Moore C. B., 2001, *ApJ*, 546, 681
- Tresse L., Maddox S. J., 1998, *ApJ*, 495, 691
- van der Hulst J. M., 2002, in *ASP Conf. Series*, Vol. 276, *Seeing Through the Dust: The Detection of HI and the Exploration of the ISM in Galaxies*, A. R. Taylor, T. L. Landecker, & A. G. Willis, ed., p. 84
- Verdes-Montenegro L., Sulentic J., Lisenfeld U., Leon S., Espada D., Garcia E., Sabater J., Verley S., 2005, *A&A*, 436, 443
- Walter F., Brinks E., de Blok W. J. G., Bigiel F., Kennicutt R. C., Thornley M. D., Leroy A., 2008, *AJ*, 136, 2563
- Warren B. E. et al., 2010, *ApJ*, 714, 571
- Wilson C. D. et al., 2011, *MNRAS*, 410, 1409
- , 2012, submitted
- Wilson C. D. et al., 2009, *ApJ*, 693, 1736

Table 1: Observations log

Galaxy	Subsample	Telescope	Instrument	Date of obs. (YY-MM-DD)	Filters ^a		Exp. time H α (s)	Pixel scale (arcsec/pix)	Seeing (arcsec)	Ref. ^b
					H α (Å/Å)	Cont. (Å/Å)				
NGC0024	SINGS Large	CTIO 1.5m	CFCCD	01-10-19	6568/20	6425/1500	600	0.43	1.3	(4)
ESO538-024	Field	WHT	ACAM	09-07-31	6589/15	6228/1322	720	0.25	2.2	(1)
NGC0210	Field	JKT	SITe2 CCD	00-01-01	6594/44	6470/1115	2400	0.24	1.3	(6)
NGC0216	Field	WHT	ACAM	09-10-08	6589/15	6228/1322	720	0.25	0.9	(1)
IC0051	Field	WHT	ACAM	09-10-07	6589/15	6228/1322	720	0.26	0.9	(1)
NGC0274	Field	WHT	ACAM	09-10-07	6589/15	6228/1322	720	0.25	0.9	(1)
NGC0337	SINGS Small	CTIO 1.5m	CFCCD	01-10-19	6602/20	6425/1500	600	0.43	1.3	(4)
NGC0404	Field	NOT	ALFOSC	09-01-13	6562/46	6500/1300	1800	0.19	0.9	(1)
NGC0450	Field	JKT	JAG-CCD	01-10-19	6594/44	6373/1491	1200	0.33	1.0	(5)
NGC0473	Field	JKT	JAG-CCD	01-10-23	6626/44	6373/1491	1200	0.33	1.2	(5)
NGC0584	SINGS Small	CTIO 1.5m	CFCCD	01-10-18	6602/18	6425/1500	601	0.43	1.1	(4)
NGC0615	Field	NOT	ALFOSC	09-01-13	6611/18	6500/1300	1800	0.19	1.1	(1)
NGC0628	SINGS Large	CTIO 1.5m	CFCCD	01-10-21	6586/20	6425/1500	600	0.43	2.3	(4)
ESO477-016	Field	NOT	ALFOSC	09-01-13	6598/18	6500/1300	1800	0.19	1.6	(1)
NGC0855	SINGS Small	WHT	ACAM	09-07-30	6577/15	6228/1322	720	0.25	1.8	(1)
NGC0925	SINGS Large	Kitt Peak 2.1m	T2KA	01-11-09	6573/67	6513/1511	600	0.30	1.6	(4)
NGC1036	Field	NOT	ALFOSC	09-01-13	6577/18	6500/1300	1800	0.19	0.9	(1)
NGC1140	Field	WHT	ACAM	10-09-03	6589/15	6228/1322	540	0.25	1.6	(1)
NGC1156	Field	JKT	JAG-CCD	00-11-17	6570/55	6373/1491	1200	0.33	1.2	(5)
ESO481-019	Field	NOT	ALFOSC	09-01-13	6598/18	6500/1300	1800	0.19	2.3	(1)
NGC1325	Field	WHT	ACAM	10-09-03	6589/15	6228/1322	540	0.42	2.7	(1)
NGC2146A	Field	JKT	JAG-CCD	01-01-20	6594/44	6373/1491	1200	0.33	2.4	(5)
NGC2403	SINGS Large	Kitt Peak 2.1m	T2KA	01-11-16	6573/67	6513/1511	600	0.30	2.2	(4)
UGC04305	SINGS Large	Kitt Peak 2.1m	CFIM	01-03-29	6573/67	6513/1511	900	0.30	1.7	(4)
PGC023521	SINGS Small	Bok 2.3m	CCD21	01-05-01	6580/69	6580/1539	1001	0.43	2.0	(8)
NGC2742	Field	JKT	JAG-CCD	01-02-11	6594/44	6471/1115	1200	0.33	2.2	(5)
NGC2787	Field	NOT	ALFOSC	09-01-13	6611/18	6500/1300	1800	0.19	4.1	(1)
NGC2841	SINGS Large	Kitt Peak 2.1m	T2KA	02-03-06	6573/67	6513/1511	200	0.30	1.4	(4)
UGC05139	SINGS Small	JKT	JAG-CCD	01-03-28	6570/55	6373/1491	1200	0.33	1.6	(5)
NGC2976	SINGS Large	JKT	JAG-CCD	00-02-23	6570/55	6390/1540	900	0.33	2.1	(5)
UGC05272	Field	Bok 2.3m	CCD21	01-04-01	6580/69	6580/1380	1000	0.43	1.3	(8)
NGC3049	SINGS Small	Kitt Peak 2.1m	T2KA	02-04-11	6618/74	6513/1511	900	0.30	1.6	(4)
NGC3031	SINGS Large	INT	WFC	08-03-15	6568/95	6380/1520	480	0.33	6.1	(1)
NGC3034	SINGS Large	Kitt Peak 2.1m	T2KA	02-03-06	6573/67	6513/1511	200	0.30	1.5	(4)
UGC05336	SINGS Small	JKT	JAG-CCD	01-03-29	6570/55	6373/1491	1200	0.33	1.7	(5)
NGC3077	Field	Bok 2.3m	CCD21	01-04-01	6580/69	6580/1539	1000	0.43	1.6	(8)
UGC05423	SINGS Small	NOT	ALFOSC	10-03-25	6564/33	6500/1300	600	0.19	1.3	(1)
NGC3162	Field	NOT	ALFOSC	08-01-03	6583/36	6500/1300	2700	0.19	1.2	(1)
NGC3190	SINGS Small	Kitt Peak 2.1m	T2KA	02-04-09	6618/74	6513/1511	900	0.30	1.6	(4)
NGC3184	SINGS Large	Kitt Peak 2.1m	T2KA	02-04-15	6573/67	6513/1511	900	0.30	1.5	(4)
NGC3198	SINGS Large	Kitt Peak 2.1m	T2KA	02-03-09	6573/67	6513/1511	900	0.30	3.4	(4)

Table 1: continued.

Galaxy	Subsample	Telescope	Instrument	Date of obs. (YY-MM-DD)	Filters ^a		Exp. time Cont. (s)	Pixel scale (arcsec/pix)	Seeing (arcsec)	Ref. ^b
					H α (Å/Å)	Cont. (Å/Å)				
NGC3227	Field	JKT	SITe2 CCD	00-01-01	6594/44	6580/1380	900	0.24	1.4	(6)
IC2574	SINGS Large	Kitt Peak 2.1m	CFIM	01-03-29	6573/67	6513/1511	900	0.30	1.9	(4)
NGC3254	Field	NOT	ALFOSC	09-01-13	6598/18	6500/1300	1800	0.19	1.7	(1)
NGC3265	SINGS Small	Kitt Peak 2.1m	T2KA	02-04-10	6618/74	6513/1511	900	0.30	1.6	(4)
UGC05720	SINGS Small	Kitt Peak 2.1m	T2KA	00-01-01	6618/74	6513/1511	240	0.30	1.1	(4)
NGC3351	SINGS Large	Kitt Peak 2.1m	T2KA	01-03-29	6573/67	6513/1511	900	0.30	1.6	(4)
NGC3353	Field	NOT	ALFOSC	09-01-13	6577/18	6500/1300	600	0.19	2.1	(1)
NGC3413	Field	NOT	ALFOSC	10-03-25	6583/36	6500/1300	600	0.19	1.4	(1)
NGC3447B	Field	NOT	ALFOSC	08-01-02	6583/36	6500/1500	2700	0.19	1.1	(1)
UGC06029	Field	NOT	ALFOSC	09-01-13	6598/18	6500/1300	1800	0.19	1.9	(1)
NGC3507	Field	JKT	JAG-CCD	00-02-29	6570/55	6373/1491	1200	0.33	1.3	(5)
NGC3521	SINGS Large	Kitt Peak 2.1m	T2KA	02-03-10	6573/67	6513/1511	900	0.30	1.4	(4)
UGC06161	Field	JKT	JAG-CCD	01-02-14	6570/55	6471/115	1200	0.33	1.6	(5)
ESO570-019	Field	NOT	ALFOSC	09-01-13	6598/18	6500/1300	600	0.19	2.1	(1)
NGC3627	SINGS Large	Kitt Peak 2.1m	T2KA	02-04-14	6618/74	6513/1511	900	0.30	1.5	(4)
UGC06378	Field	NOT	ALFOSC	09-01-13	6598/18	6500/1300	1800	0.19	1.6	(1)
UGC06566	Field	NOT	ALFOSC	09-01-13	6598/18	6500/1300	1200	0.19	1.9	(1)
NGC3741	Field	JKT	JAG-CCD	01-01-20	6570/55	6373/1491	1200	0.33	1.0	(5)
UGC06578	Field	INT	WFC	08-03-14	6568/95	6380/1520	480	0.33	1.9	(1)
NGC3773	SINGS Small	Kitt Peak 2.1m	T2KA	02-04-11	6573/67	6513/1511	900	0.30	1.2	(4)
NGC3782	Field	JKT	JAG-CCD	01-02-14	6570/55	6373/1491	1200	0.33	1.6	(5)
UGC06792	Field	INT	WFC	09-05-04	6568/95	6380/1520	1800	0.33	1.8	(1)
NGC3931	Field	NOT	ALFOSC	10-03-25	6583/36	6500/1300	480	0.19	1.3	(1)
NGC3928	Field	NOT	ALFOSC	10-03-25	6583/36	6500/1300	480	0.19	1.6	(1)
NGC3938	SINGS Large	Kitt Peak 2.1m	T2KA	02-04-12	6573/67	6513/1511	900	0.30	2.6	(4)
NGC3998	Field	NOT	ALFOSC	10-03-26	6583/36	6500/1300	480	0.19	0.9	(1)
NGC4013	Field	NOT	ALFOSC	10-03-26	6583/36	6500/1300	360	0.19	1.0	(1)
IC0750	Field	JKT	JAG-CCD	99-02-11	6570/55	6373/1491	1200	0.33	1.5	(5)
UGC07009	Field	NOT	ALFOSC	09-01-13	6583/36	6500/1300	1800	0.19	1.7	(1)
NGC4041	Field	NOT	ALFOSC	09-01-13	6583/36	6500/1300	1800	0.19	1.1	(1)
NGC4117	Field	NOT	ALFOSC	10-03-26	6583/36	6500/1300	480	0.19	0.8	(1)
NGC4138	Field	NOT	ALFOSC	10-03-26	6583/36	6500/1300	480	0.19	0.8	(1)
NGC4190	Field	JKT	JAG-CCD	01-01-20	6570/55	6373/1491	1200	0.33	1.1	(5)
PGC039265	Virgo Small	SPM 2.1m	SIT3	04-03-17	6603/100	6550/900	900	0.31	1.8	(7)
NGC4236	SINGS Large	NOT	ALFOSC	10-03-25	6564/33	6500/1300	480	0.19	0.9	(1)
IC3105	Field	JKT	JAG-CCD	01-05-18	6570/55	6373/1491	1200	0.33	1.5	(5)
NGC4241	Virgo Small	Calar Alto 1.23m	SITe	99-04-19	6569/113	6744/97	600	0.50	1.7	(3)
NGC4254	SINGS Large	Kitt Peak 2.1m	T2KA	02-04-12	6618/74	6513/1511	900	0.30	2.5	(4)
NGC4262	Virgo Small	INT	WFC	08-03-14	6568/95	6380/1520	480	0.33	1.6	(1)
IC3155	Virgo Small	NOT	ALFOSC	10-03-26	6611/18	6500/1300	480	0.19	1.0	(1)
NGC4268	Virgo Small	NOT	ALFOSC	10-03-26	6611/18	6500/1300	480	0.19	1.1	(1)

Table 1: continued.

Galaxy	Subsample	Telescope	Instrument	Date of obs. (YY-MM-DD)	Filters ^a		Exp. time H α (s)	Pixel scale (arcsec/pix)	Seeing (arcsec)	Ref. ^b
					H α (Å/Å)	Cont. (Å/Å)				
NGC4270	Virgo Small	NOT	ALFOSC	10-03-26	6611/18	6500/1300	480	0.19	0.9	(1)
NGC4277	Virgo Small	NOT	ALFOSC	10-03-26	6611/18	6500/1300	480	0.19	0.8	(1)
NGC4288	Field	Bok 2.3m	CCD21	01-05-01	6580/69	6580/1539	1000	0.43	1.2	(8)
NGC4298	Virgo Small	Calar Alto 1.23m	SITe	99-04-17	6569/110	6744/97	600	0.50	3.0	(3)
UGC07428	Field	WHT	TEK2	07-04-03	6594/44	6391/1455	360	0.22	15.0	(1)
NGC4301	Virgo Small	INT	WFC	08-03-15	6568/95	6380/1520	480	0.33	1.9	(1)
NGC4318	Virgo Small	INT	WFC	08-03-15	6568/95	6380/1520	480	0.33	1.3	(1)
NGC4321	SINGS Large	Kitt Peak 2.1m	CFIM	01-03-28	6573/67	6513/1511	900	0.30	1.3	(4)
NGC4324	Virgo Small	SPM 2.1m	TEK	00-04-01	6603/90	6723/90	420	0.31	2.3	(2)
NGC4376	Virgo Small	INT	WFC	09-05-06	6568/95	6380/1520	1800	0.33	1.6	(1)
NGC4383	Virgo Small	SPM 2.1m	SITe	04-03-11	6603/90	6550/900	1200	0.31	2.1	(7)
UGC07512	Field	NOT	ALFOSC	10-03-26	6598/18	6500/1300	480	0.19	1.0	(1)
NGC4390	Virgo Small	SPM 2.1m	SITe	04-03-11	6603/90	6550/900	240	0.31	1.9	(7)
NGC4394	Virgo Small	JKT	JAG-CCD	01-02-17	6570/55	6373/1491	1200	0.33	1.2	(5)
NGC4423	Virgo Small	NOT	ALFOSC	10-03-26	6583/36	6500/1300	360	0.19	1.5	(1)
NGC4430	Virgo Small	OHP 1.2m	TEK	93-03-07	6612/55	6000/1500	600	0.41	2.0	(3)
IC3365	Virgo Small	JKT	JAG-CCD	01-01-21	6607/50	6373/1491	1200	0.33	1.6	(5)
UGC07590	Virgo Small	SPM 2.1m	Thomson	01-04-25	6603/90	6723/90	300	0.39	1.7	(2)
NGC4450	SINGS Large	Kitt Peak 2.1m	T2KA	02-04-09	6618/74	6513/1511	900	0.30	1.4	(4)
NGC4468	Virgo Small	MDM 2.4m	MDM8K	08-12-30	6563/100	6470/1330	2700	0.35	2.2	(1)
NGC4470	Virgo Small	Calar Alto 1.23m	SITe	99-04-18	6569/113	6744/97	600	0.51	1.9	(3)
NGC4504	Field	NOT	ALFOSC	11-07-24	6583/36	6500/1300	900	0.19	1.1	(1)
NGC4522	Virgo Small	SPM 2.1m	SIT3	04-03-11	6603/90	6550/900	900	0.31	2.5	(7)
NGC4532	Virgo Small	MDM 2.4m	MDM8K	08-12-30	6563/100	6470/1330	2700	0.35	1.8	(1)
UGC07739	Virgo Small	SPM 2.1m	Thomson	01-04-23	6603/90	6723/90	600	0.39	2.9	(2)
IC3522	Virgo Small	MDM 2.4m	MDM8K	08-12-31	6563/100	6470/1330	1800	0.35	1.2	(1)
NGC4550	Field	INT	WFC	08-03-16	6568/95	6380/1520	480	0.33	1.7	(1)
NGC4559	SINGS Large	Kitt Peak 2.1m	T2KA	02-03-09	6673/67	6513/1511	900	0.30	2.0	(4)
NGC4561	Virgo Small	INT	WFC	09-06-13	6568/95	6380/1520	1199	0.33	1.8	(1)
NGC4567	Virgo Small	OHP 1.2m	TEK	98-02-28	6612/55	6561/48	1800	0.69	2.8	(3)
NGC4568	Virgo Small	OHP 1.2m	TEK	98-02-28	6612/55	6561/48	1800	0.69	2.8	(3)
IC3583	Virgo Small	SPM 2.1m	TEK	99-04-17	6603/90	6723/90	420	0.30	3.3	(2)
NGC4569	SINGS Large	OHP 1.2m	TEK	98-02-28	6561/48	6600/55	1800	0.68	3.2	(7)
IC3591	Virgo Small	NOT	ALFOSC	10-02-09	6583/36	6500/1300	1800	0.19	1.8	(1)
NGC4579	SINGS Large	Kitt Peak 2.1m	T2KA	02-03-10	6618/74	6513/1511	900	0.30	1.3	(4)
IC3617	Virgo Small	SPM 2.1m	Thomson	01-04-25	6603/90	6723/90	300	0.39	2.5	(2)
UGC07827	Field	INT	WFC	09-05-05	6568/95	6380/1520	1800	0.33	1.5	(1)
NGC4595	Virgo Small	JKT	JAG-CCD	01-03-27	6570/55	6373/1491	1200	0.33	2.0	(5)
NGC4594	SINGS Large	Kitt Peak 2.1m	T2KA	02-03-10	6573/67	6513/1511	900	0.30	1.2	(4)
NGC4625	SINGS Small	NOT	ALFOSC	10-02-09	6583/36	6500/1300	1800	0.19	1.3	(1)
NGC4631	SINGS Large	Kitt Peak 2.1m	T2KA	02-03-11	6573/67	6513/1511	900	0.30	2.5	(4)

Table 1: continued.

Galaxy	Subsample	Telescope	Instrument	Date of obs. (YY-MM-DD)	H α (Å/Å)	Filters ^a Cont. (Å/Å)	H α (s)	Exp. time Cont (s)	Pixel scale (arcsec/pix)	Seeing (arcsec)	Ref. ^b
NGC4639	Virgo Small	OHP 1.20m	TEK	00-03-09	6612/55	6450/45	900	900	0.69	3.3	(3)
NGC4640	Virgo Small	NOT	ALFOSC	10-03-27	6610/50	6500/1300	480	120	0.19	0.9	(1)
NGC4647	Virgo Small	INT	WFC	09-06-13	6568/95	6380/1520	2399	540	0.33	2.0	(1)
NGC4651	Virgo Small	JKT	JAG-CCD	00-04-23	6570/55	6373/1491	1200	300	0.33	1.7	(5)
PGC043211	Field	NOT	ALFOSC	10-03-27	6583/36	6500/1300	480	120	0.19	0.8	(1)
NGC4725	SINGS Large	Kitt Peak 2.1m	T2KA	02-03-11	6573/67	6513/1511	900	420	0.30	2.2	(4)
NGC4736	SINGS Large	JKT	JAG CCD	02-01-15	6570/55	6580/1380	3600	1620	0.24	1.4	(6)
NGC4772	Field	SPM 2.1m	SIT3	03-02-28	6603/90	6550/900	900	240	0.31	2.0	(7)
NGC4789A	SINGS Small	JKT	JAG-CCD	00-04-26	6570/55	6471/115	1200	600	0.33	1.6	(5)
NGC4826	SINGS Large	Kitt Peak 0.9m	T2KA	99-04-22	6573/67	6513/1511	360	20	0.78	1.8	(4)
NGC4941	Field	NOT	ALFOSC	10-03-27	6583/36	6500/1300	480	120	0.19	0.8	(1)
PGC045195	Field	INT	WFC	08-03-16	6568/95	6380/1520	528	130	0.33	1.3	(1)
UGC08201	SINGS Small	JKT	JAG-CCD	01-03-31	6570/55	6373/1491	1200	300	0.33	2.0	(5)
UGC08303	Field	JKT	JAG-CCD	01-01-23	6570/55	6373/1491	1200	300	0.33	1.4	(5)
NGC5033	SINGS Large	NOT	ALFOSC	10-03-27	6583/36	6500/1300	360	83	0.19	0.8	(1)
ESO508-030	Field	NOT	ALFOSC	10-03-27	6598/18	6500/1300	480	120	0.19	0.9	(1)
NGC5055	SINGS Large	Kitt Peak 0.9m	T2KA	99-04-20	6573/67	-/-	420	-	0.38	-	(4)
NGC5194	SINGS Large	Kitt Peak 2.1m	CFIM	01-03-28	6573/67	6425/1500	900	372	0.30	1.4	(4)
NGC5195	SINGS Large	Kitt Peak 2.1m	CFIM	01-03-28	6573/67	6425/1500	900	372	0.30	1.4	(4)
NGC5474	SINGS Small	JKT	JAG-CCD	00-02-29	6570/55	6471/115	1200	1200	0.33	1.4	(5)
NGC5477	Field	JKT	JAG-CCD	00-07-04	6570/55	6373/1491	1200	300	0.33	0.9	(5)
NGC5486	Field	JKT	JAG-CCD	01-05-13	6594/44	1471/115	1200	1200	0.33	1.3	(5)
PGC140287	Field	INT	WFC	08-03-17	6568/95	6380/1520	450	135	0.33	2.2	(1)
IC1024	Field	WHT	TEK2	07-04-28	6594/44	6391/1455	360	300	0.22	1.9	(1)
NGC5701	Field	NOT	ALFOSC	10-03-27	6598/18	6500/1300	480	120	0.19	0.8	(1)
IC1066	Field	INT	WFC	08-03-14	6568/95	6380/1520	600	285	0.33	1.9	(1)
PGC057723	Field	INT	WFC	08-03-16	6568/95	6380/1520	480	120	0.33	1.7	(1)
NGC6140	Field	INT	PFCU	96-05-14	6594/44	6580/1380	3600	1800	0.24	1.4	(6)
NGC6118	Field	INT	WFC	08-03-14	6568/95	6380/1520	600	180	0.33	1.8	(1)
PGC058661	Field	INT	WFC	08-03-16	6568/95	6380/1520	510	135	0.33	1.3	(1)
IC1254	Field	WHT	TEK2	07-04-28	6594/44	6391/1455	360	300	0.21	1.3	(1)
NGC7465	Field	WHT	ACAM	09-07-30	6613/15	6228/1322	720	360	0.25	1.5	(1)
NGC7742	Field	WHT	ACAM	10-09-03	6589/15	6228/1322	900	60	0.30	1.1	(1)

^a Given for the H α and the continuum filters in the format central wavelength/FWHM.

^b (1) This work; (2) Gavazzi et al. (2002); (3) Boselli et al. (2002); (4) Kennicutt et al. (2003); (5) James et al. (2004); (6) Knapen et al. (2004); (7) Gavazzi et al. (2006); (8) Kennicutt et al. (2008)

Table 2: Results

Galaxy	Class	v_{rec} kms $^{-1}$	Dist. Mpc	a/b arcmin	$M(B)$ mag	k	η %	$F(\text{H}\alpha + [\text{NII}])$ $10^{-13} \text{ erg cm}^{-2} \text{ s}^{-1}$	A_T mag	ξ_{Obs}^a	$L(\text{H}\alpha)^b$ $10^{40} \text{ erg s}^{-1}$	SFR^b $M_{\odot} \text{ yr}^{-1}$	EW Å
NGC0024	SA(s)c	554	7.6 (1.1)	5.8/1.3	-15.49	0.011	1.1	18.0 (3.1)	0.3	0.03	1.6 (0.6)	0.09 (0.03)	19 (1) [3]
ESO538-024	IB(s)m	1551	21.4 (3.2)	1.4/1.2	-16.44 ^c	0.014	1.1	1.8 (0.3)	0.4	0.02	1.3 (0.5)	0.07 (0.02)	28 (6) [1]
NGC0210	SAB(s)b	1663	23.1 (3.5)	5.0/3.3	-19.76	0.516	0.0	52.6 (8.9)	0.8	0.3	47.8 (16.5)	2.53 (0.87)	31 (7) [1]
NGC0216	S0	1541	21.0 (3.1)	2.0/0.7	-17.44	0.015	1.1	5.1 (0.9)	0.5	0.03	4.1 (1.4)	0.22 (0.08)	13 (3) [1]
IC0051	S0	1753	23.8 (3.6)	1.3/1.2	-17.70 ^c	0.015	1.1	2.7 (0.5)	0.5	0.03	2.8 (1.0)	0.15 (0.05)	8 (2) [1]
NGC0274	SAB(r)	1773	24.6 (3.7)	2.3/1.5	-18.66 ^c	0.012	1.1	6.4 (1.1)	0.7	0.04	8.8 (3.0)	0.46 (0.16)	7 (1) [1]
NGC0337	SB(s)d	1648	23.1 (3.5)	2.9/1.8	-19.32	0.009	1.1	27.2 (4.6)	0.9	0.13	34.5 (11.9)	1.83 (0.63)	43 (9) [1]
NGC0404	SA(s)0	-48	2.8 (0.4)	3.5/3.5	-13.79	0.035	3.5	18.1 (3.1)	0.3	0.03	0.2 (0.1)	0.01 (0.00)	6 (1) [1]
NGC0450	SAB(s)cd	1761	25.0 (3.7)	3.1/2.3	-18.11 ^c	-	2.0	19.7 (3.4)	0.6	0.16	21.3 (7.3)	1.13 (0.39)	53 (5) [3]
NGC0473	SAB(r)0/a	2222	31.3 (4.7)	1.7/1.1	-18.67	-	2.0	3.4 (0.6)	1.0	0.2	8.0 (2.8)	0.43 (0.15)	12 (4) [3]
NGC0584	E4	1802	20.1 (3.0)	4.2/2.3	-20.14	0.010	1.1	7.2 (1.2)	1.3	0.14	10.2 (3.5)	0.54 (0.19)	3 (1) [1]
NGC0615	SA(rs)b	1948	25.6 (3.8)	3.6/1.4	-19.18	0.010	1.5	12.9 (2.2)	0.7	0.1	17.0 (5.9)	0.90 (0.31)	16 (3) [1]
NGC0628	SA(s)c	657	7.3 (1.1)	10.5/9.5	-18.51	-	1.1	146.1 (24.8)	0.9	0.09	18.9 (6.5)	1.00 (0.35)	35 (4) [3]
ESO477-016	Sb	1646	24.2 (3.6)	2.8/0.3	-16.78 ^c	0.018	1.5	3.6 (0.6)	0.4	0.04	3.5 (1.2)	0.18 (0.06)	32 (6) [1]
NGC0855	E	575	9.7 (1.5)	2.6/1.0	-15.06	0.014	1.1	7.8 (1.3)	1.3	0.01	2.8 (1.0)	0.15 (0.05)	40 (4) [3]
NGC0925	SAB(s)d	553	9.1 (1.4)	10.5/5.9	-17.56	0.046	4.2	26.9 (4.6)	0.8	0.13	4.9 (1.7)	0.26 (0.09)	25 (2) [3]
NGC1036	Pec?	802	12.5 (1.9)	1.4/1.0	-15.69	0.013	3.0	13.9 (2.4)	0.6	0.02	4.3 (1.5)	0.23 (0.08)	50 (10) [1]
NGC1140	IBm	1501	20.1 (3.0)	1.7/0.9	-18.42	0.017	1.1	30.0 (5.1)	0.5	0.04	22.5 (7.8)	1.19 (0.41)	48 (10) [1]
NGC1156	IB(s)m	375	7.2 (1.1)	3.3/2.5	-14.57	-	2.0	26.5 (4.5)	0.8	0.04	3.3 (1.1)	0.17 (0.06)	74 (7) [3]
ESO481-019	IB(s)m	1480	19.8 (3.0)	2.0/1.7	-16.43 ^c	0.012	1.5	9.3 (1.6)	0.3	0.03	5.7 (2.0)	0.30 (0.10)	193 (41) [1]
NGC1325	SA(s)bc	1646	20.6 (3.1)	4.7/1.6	-19.29	0.012	1.1	12.7 (2.2)	0.7	0.06	12.0 (4.1)	0.63 (0.22)	12 (2) [1]
NGC2146A	SAB(s)c	1386	25.9 (3.9)	3.0/1.1	-18.04	-	1.8	2.7 (0.5)	0.8	0.15	4.0 (1.4)	0.21 (0.07)	17 (4) [3]
NGC2403	SAB(s)cd	131	3.2 (0.5)	21.9/12.3	-18.03	-	4.2	791.6 (134.6)	0.7	0.16	16.2 (5.6)	0.86 (0.30)	50 (15) [3]
UGC04305	Im	142	3.4 (0.5)	7.9/6.3	-15.96	0.012	4.2	48.2 (8.2)	0.4	0.07	0.9 (0.3)	0.05 (0.02)	37 (4) [3]
PGC023521	I	113	3.6 (0.5)	1.3/0.7	-11.05 ^c	0.240	4.5	0.2 (0.0)	0.1	0.01	0.0 (0.0)	0.00 (0.00)	98 (23) [1]
NGC2742	SA(s)c	1285	22.7 (3.4)	3.0/1.5	-19.40	-	0.0	18.2 (3.1)	1.0	0.26	20.1 (6.9)	1.06 (0.37)	21 (2) [3]
NGC2787	SB(r)0+	696	14.4 (2.2)	3.2/2.0	-18.31	0.011	1.5	8.0 (1.4)	1.1	0.07	4.9 (1.7)	0.26 (0.09)	3 (1) [1]
NGC2841	SA(r)b	638	14.1 (2.1)	8.1/3.5	-20.14	-	4.2	38.2 (6.5)	1.4	0.38	19.7 (6.8)	1.04 (0.36)	7 (3) [2]
UGC05139	IAB(s)m	139	3.6 (0.5)	3.6/3.0	-14.26	-	2.0	3.6 (0.6)	0.3	0.04	0.1 (0.0)	0.00 (0.00)	55 (6) [3]
NGC2976	SAC	3	3.6 (0.5)	5.9/2.7	-14.65	-	2.0	62.0 (10.5)	0.5	0.04	1.4 (0.5)	0.07 (0.03)	35 (3) [3]
UGC05272	ImIII	524	7.0 (1.1)	2.1/0.8	-15.71	0.250	4.5	1.8 (0.3)	0.4	0.06	0.1 (0.0)	0.01 (0.00)	62 (6) [3]
NGC3049	SB(rs)ab	1455	22.7 (3.4)	2.1/1.1	-19.85 ^c	0.044	4.5	18.1 (3.1)	0.9	0.34	16.7 (5.8)	0.88 (0.30)	65 (13) [1]
NGC3031	SA(s)ab	-34	3.6 (0.5)	26.9/14.1	-16.21	0.060	3.0	1849.0 (314.3)	0.5	0.08	42.4 (14.6)	2.25 (0.77)	10 (1) [3]
NGC3034	I0	203	3.6 (0.5)	11.2/4.3	-18.63	0.041	4.2	766.9 (130.4)	1.4	0.21	33.6 (11.6)	1.78 (0.61)	64 (5) [3]
UGC05336	Im	46	3.6 (0.5)	2.5/2.0	-11.93	-	3.0	1.1 (0.2)	0.3	0.01	0.0 (0.0)	0.00 (0.00)	18 (4) [3]
NGC3077	I0	14	2.5 (0.4)	5.4/4.5	-15.07	0.217	4.5	51.5 (8.8)	0.4	0.05	0.5 (0.2)	0.03 (0.01)	42 (4) [3]
UGC05423	Im	347	3.6 (0.5)	0.9/0.6	-14.81 ^c	0.028	3.0	4.7 (0.8)	0.4	0.04	0.1 (0.0)	0.01 (0.00)	27 (4) [3]
NGC3162	SAB(rs)bc	1384	21.7 (3.3)	3.0/2.5	-19.52	0.022	2.5	75.8 (12.9)	0.4	0.25	44.4 (15.3)	2.36 (0.81)	102 (21) [1]
NGC3190	SA(s)a	1271	21.3 (3.2)	4.4/1.5	-19.57	-	4.5	8.5 (1.5)	1.3	0.3	10.6 (3.7)	0.56 (0.19)	3 (2) [2]
NGC3184	SAB(rs)cd	592	11.1 (1.7)	7.4/6.9	-19.92	-	4.2	69.9 (11.9)	1.2	0.35	19.7 (6.8)	1.04 (0.36)	13 (6) [2]
NGC3198	SB(rs)c	663	13.7 (2.1)	8.5/3.3	-19.54	-	4.2	38.4 (6.5)	1.0	0.3	14.7 (5.1)	0.78 (0.27)	34 (17) [2]

Table 2: continued.

Galaxy	Class	v_{rec} kms $^{-1}$	Dist. Mpc	a/b arcmin	M(B) mag	k	η %	$F(\text{H}\alpha + [\text{NII}])$ $10^{-13} \text{ erg cm}^{-2} \text{ s}^{-1}$	A_T mag	ξ_{obs}^a	$L(\text{H}\alpha)^b$ $10^{40} \text{ erg s}^{-1}$	SFR b $M_{\odot} \text{ yr}^{-1}$	EW Å
NGC3227	SAB(s)	1157	23.1 (3.5)	5.4/3.6	-20.26	0.020	3.0	4.5 (0.8)	0.9	0.37	4.0 (1.4)	0.21 (0.07)	13 (3) [1]
IC2574	SAB(s)m	57	3.8 (0.6)	13.2/5.4	-15.74	0.047	4.2	89.8 (15.3)	0.4	0.07	2.0 (0.7)	0.11 (0.04)	31 (8) [3]
NGC3254	SA(s)bc	1262	23.2 (3.5)	5.0/1.6	-19.37	0.014	1.5	16.1 (2.7)	1.0	0.11	23.6 (8.1)	1.25 (0.43)	13 (3) [1]
NGC3265	E	1319	22.7 (3.4)	1.3/1.0	-18.78 ^c	-	4.5	5.0 (0.9)	0.6	0.22	4.0 (1.4)	0.21 (0.07)	46 (22) [2]
UGC05720	Im	1430	25.0 (3.8)	1.1/0.8	-18.33 ^c	-	4.5	21.3 (3.6)	0.7	0.18	24.1 (8.3)	1.28 (0.44)	80 (38) [2]
NGC3351	SB(r)b	778	9.3 (1.4)	3.1/2.9	-20.42	0.047	4.2	101.5 (17.3)	1.4	0.42	22.5 (7.8)	1.19 (0.41)	16 (3) [3]
NGC3353	BCD/Irr	944	18.0 (2.7)	1.2/0.8	-17.67	0.018	1.5	19.3 (3.3)	0.5	0.05	11.6 (4.0)	0.62 (0.21)	49 (10) [1]
NGC3413	S0	667	8.8 (1.3)	2.2/0.9	-17.46 ^c	0.029	3.0	9.4 (1.6)	0.5	0.11	1.2 (0.4)	0.06 (0.02)	36 (7) [1]
NGC3447B	IB(s)m	1023	17.0 (2.6)	4.2/2.3	-	0.028	2.5	4.9 (0.8)	0.4	0.0	2.4 (0.8)	0.13 (0.04)	119 (25) [1]
UGC06029	Pec	1403	24.2 (3.6)	1.0/0.9	-17.64 ^c	0.019	1.5	9.6 (1.6)	0.4	0.05	9.5 (3.3)	0.50 (0.17)	137 (29) [1]
NGC3507	SB(s)b	967	14.3 (2.1)	3.4/2.9	-19.56	-	2.0	41.0 (7.0)	1.0	0.29	17.4 (6.0)	0.92 (0.32)	39 (4) [3]
NGC3521	SAB(rs)bc	801	7.9 (1.2)	11.0/5.1	-21.20	0.047	4.2	126.8 (21.6)	1.2	0.53	13.0 (4.5)	0.69 (0.24)	20 (3) [3]
UGC06161	SBdm	804	13.3 (2.0)	2.6/1.2	-16.67 ^c	-	2.0	2.6 (0.4)	0.4	0.09	0.7 (0.2)	0.04 (0.01)	34 (3) [3]
ESO570-019	(R)SAc	1249	19.4 (2.9)	1.6/0.5	-17.91 ^c	0.016	1.5	3.7 (0.6)	0.6	0.06	2.6 (0.9)	0.14 (0.05)	25 (5) [1]
NGC3627	SAB(s)b	727	9.4 (1.4)	9.1/4.2	-21.20	0.049	4.5	125.5 (21.3)	1.7	0.54	30.3 (10.4)	1.60 (0.55)	19 (2) [3]
UGC06378	Sd	1309	23.8 (3.6)	2.7/0.4	-16.75 ^c	0.019	1.5	3.6 (0.6)	0.4	0.04	3.5 (1.2)	0.18 (0.06)	34 (7) [1]
UGC06566	SBm	1249	22.5 (3.4)	1.1/0.8	-	0.011	1.5	1.0 (0.2)	0.3	0.0	0.8 (0.3)	0.04 (0.02)	16 (3) [1]
NGC3741	ImIII/BCD	223	3.6 (0.5)	2.0/1.1	-14.68	-	2.0	4.5 (0.8)	0.3	0.04	0.1 (0.0)	0.00 (0.00)	66 (7) [3]
UGC06578	WR/BCD	1178	15.8 (2.4)	0.7/0.5	-16.27 ^c	0.076	6.0	4.6 (0.8)	0.4	0.08	1.8 (0.6)	0.09 (0.03)	118 (24) [1]
NGC3773	SA0	987	10.5 (1.6)	1.2/1.0	-18.80 ^c	-	4.2	9.3 (1.6)	0.6	0.22	1.7 (0.6)	0.09 (0.03)	37 (17) [2]
NGC3782	SAB(s)cd	748	13.4 (2.0)	1.7/1.1	-17.50	-	2.0	11.3 (1.9)	0.5	0.13	3.4 (1.2)	0.18 (0.06)	53 (5) [3]
UGC06792	Scd	832	14.7 (2.2)	2.8/0.4	-16.32 ^c	0.064	6.0	7.9 (1.3)	0.5	0.08	3.0 (1.0)	0.16 (0.06)	31 (6) [1]
NGC3931	SA0-	929	16.2 (2.4)	1.1/0.9	-16.40 ^c	0.019	3.0	3.4 (0.6)	0.5	0.07	1.6 (0.5)	0.08 (0.03)	18 (3) [1]
NGC3928	SA(s)b?	951	18.9 (2.8)	1.3/1.2	-17.85	0.027	3.0	0.1 (0.0)	0.7	0.13	0.1 (0.0)	0.01 (0.00)	27 (5) [1]
NGC3938	SA(s)c	809	14.7 (2.2)	5.4/4.9	-19.88	-	4.2	71.4 (12.1)	1.1	0.34	33.1 (11.4)	1.75 (0.60)	21 (10) [2]
NGC3998	SA(r)0	1040	20.0 (3.0)	2.7/2.2	-19.49	0.024	3.0	13.7 (2.3)	1.0	0.25	12.3 (4.3)	0.65 (0.23)	5 (1) [1]
NGC4013	SAb	831	15.3 (2.3)	5.2/1.0	-18.63	0.016	3.0	18.4 (3.1)	0.8	0.18	8.6 (3.0)	0.46 (0.16)	22 (4) [1]
IC0750	Sab:	701	11.8 (1.8)	2.5/0.9	-17.60	-	2.0	17.4 (3.0)	0.7	0.13	4.8 (1.7)	0.26 (0.09)	26 (3) [3]
UGC07009	Im	1097	21.3 (3.2)	2.0/0.5	-15.66	0.031	2.5	3.5 (0.6)	0.4	0.05	2.5 (0.9)	0.13 (0.05)	44 (9) [1]
NGC4041	SA(rs)bc:	1221	22.9 (3.4)	2.1/1.7	-19.48	0.029	3.0	74.4 (12.6)	0.8	0.25	75.3 (26.0)	3.99 (1.38)	46 (9) [1]
NGC4117	S0	886	17.7 (2.7)	1.7/0.6	-16.98 ^c	0.024	3.0	1.7 (0.3)	0.6	0.09	1.0 (0.3)	0.05 (0.02)	5 (1) [1]
NGC4138	SA(r)0+	888	16.7 (2.5)	2.6/1.7	-18.76	0.018	3.0	26.3 (4.5)	0.8	0.19	14.6 (5.0)	0.77 (0.27)	21 (4) [1]
NGC4190	Im	192	2.8 (0.4)	1.5/1.2	-15.22	-	2.0	4.6 (0.8)	0.4	0.05	0.1 (0.0)	0.00 (0.00)	20 (2) [3]
PGC039265	IAm?	2175	13.6 (1.1)	1.1/0.5	-17.90 ^c	0.300	10.0	0.7 (0.1)	0.4	0.16	0.2 (0.0)	0.01 (0.00)	60 (20) [3]
NGC4236	SB(s)dm	0	4.4 (0.7)	21.9/7.2	-15.20	0.011	3.0	76.4 (13.0)	0.3	0.04	2.2 (0.8)	0.12 (0.04)	29 (4) [3]
IC3105	Im	-159	2.4 (0.4)	1.8/0.5	-12.13	-	2.0	0.7 (0.1)	0.2	0.02	0.0 (0.0)	0.00 (0.00)	73 (7) [3]
NGC4241	SB(s)cd	733	16.7 (1.1)	1.2/1.0	-17.12	0.660	0.0	3.0 (0.5)	0.4	0.11	1.2 (0.3)	0.07 (0.01)	10 (2) [1]
NGC4254	SA(s)c	2407	16.7 (2.5)	5.4/4.7	-22.45	0.051	4.5	161.2 (27.4)	2.3	0.54	213.4 (73.6)	11.31 (3.90)	39 (8) [1]
NGC4262	SB(s)0-?	1363	16.7 (1.1)	1.9/1.7	-19.34	0.067	6.0	6.7 (1.1)	0.9	0.28	3.8 (0.8)	0.20 (0.04)	6 (1) [1]
IC3155	S0	2209	16.7 (1.1)	1.2/0.6	-17.82 ^c	0.011	1.5	0.4 (0.1)	0.7	0.06	0.2 (0.0)	0.01 (0.00)	3 (1) [1]
NGC4268	SB0/a	2374	16.7 (1.1)	1.6/0.7	-19.06	0.012	1.5	0.4 (0.1)	1.0	0.09	0.3 (0.1)	0.01 (0.00)	1 (0) [1]

Table 2: continued.

Galaxy	Class	v_{rec} kms $^{-1}$	Dist. Mpc	a/b arcmin	M(B) mag	k	η %	$F(\text{H}\alpha + [\text{NII}])$ $10^{-13} \text{ erg cm}^{-2} \text{ s}^{-1}$	Ar mag	ξ_{obs}^a	$L(\text{H}\alpha)^b$ $10^{40} \text{ erg s}^{-1}$	SFR b $M_{\odot} \text{ yr}^{-1}$	EW Å
NGC4270	S0	2357	16.7 (1.1)	2.0/0.9	-19.79	0.011	1.5	1.6 (0.3)	1.0	0.12	1.1 (0.2)	0.06 (0.01)	2 (0) [1]
NGC4277	SAB(rs)0/a	2196	16.7 (1.1)	1.1/0.8	-19.35	0.010	1.5	1.1 (0.2)	0.7	0.1	0.6 (0.1)	0.03 (0.01)	3 (1) [1]
NGC4288	SB(s)dm	556	8.7 (1.3)	1.6/1.2	-16.74	0.247	4.5	8.9 (1.5)	0.3	0.1	1.0 (0.3)	0.05 (0.02)	49 (4) [3]
NGC4298	SA(rs)c	1135	16.7 (1.1)	3.3/1.2	-19.48	0.640	0.0	14.8 (2.5)	0.4	0.29	5.0 (1.1)	0.27 (0.06)	36 (8) [1]
UGC07428	Im	1170	22.5 (3.4)	1.3/1.2	-17.34	0.021	3.0	0.5 (0.1)	0.3	0.12	0.3 (0.1)	0.02 (0.01)	5 (1) [1]
NGC4301	SAB(s)cd	1275	16.7 (1.1)	1.5/1.3	-18.34	0.067	6.0	10.9 (1.9)	0.4	0.19	4.1 (0.9)	0.22 (0.05)	55 (11) [1]
NGC4318	E?	1231	16.7 (1.1)	0.8/0.7	-17.47	0.062	6.0	1.4 (0.2)	0.4	0.13	0.5 (0.1)	0.03 (0.01)	8 (2) [1]
NGC4321	SAB(s)bc	1571	16.7 (2.5)	7.4/6.3	-22.03	-	4.2	85.7 (14.6)	2.0	0.53	85.3 (29.4)	4.52 (1.56)	7 (3) [2]
NGC4324	SA(r)0+	1685	16.7 (1.1)	2.8/1.2	-19.70	1.000	0.0	3.7 (0.6)	0.4	0.32	1.2 (0.3)	0.06 (0.01)	7 (1) [1]
NGC4376	Im	1136	16.7 (1.1)	1.4/0.9	-17.67	0.064	6.0	14.3 (2.4)	0.6	0.14	7.0 (1.5)	0.37 (0.08)	76 (15) [1]
NGC4383	Sa?	1710	16.7 (1.1)	1.9/1.0	-19.57	0.330	10.0	22.6 (3.8)	0.4	0.3	7.3 (1.6)	0.39 (0.08)	650 (10) [3]
UGC07512	ImIV	1505	27.6 (4.1)	1.3/0.6	-17.03 ^c	0.013	1.5	3.7 (0.6)	0.5	0.04	4.9 (1.7)	0.26 (0.09)	56 (11) [1]
NGC4390	Sbc(s)	1131	16.7 (1.1)	1.6/1.1	-18.18	0.420	10.0	4.2 (0.7)	0.4	0.17	1.6 (0.4)	0.09 (0.02)	280 (40) [3]
NGC4394	(R)SB(r)b	922	16.7 (1.1)	3.6/3.2	-19.42	-	2.0	12.9 (2.2)	1.0	0.28	8.0 (1.7)	0.43 (0.09)	10 (3) [3]
NGC4423	Sdm	1104	16.7 (1.1)	2.3/0.4	-17.51	0.032	3.0	2.5 (0.4)	0.5	0.11	1.2 (0.3)	0.06 (0.01)	18 (3) [1]
NGC4430	SB(rs)b	1468	16.7 (1.1)	1.9/1.2	-19.17	-	3.0	6.4 (1.1)	0.3	0.25	2.2 (0.5)	0.12 (0.03)	5 (1) [1]
IC3365	Im	2375	16.7 (1.1)	2.1/1.0	-18.48	-	2.0	1.9 (0.3)	0.7	0.19	1.0 (0.2)	0.05 (0.01)	24 (4) [3]
UGC07590	Sbc	1118	13.6 (1.1)	1.3/0.4	-17.40	1.150	0.0	1.6 (0.3)	0.4	0.13	0.4 (0.1)	0.02 (0.01)	36 (9) [1]
NGC4450	SA(s)ab	1954	16.7 (2.5)	5.2/3.9	-21.58	-	4.5	28.0 (4.8)	1.9	0.54	26.0 (9.0)	1.38 (0.48)	4 (2) [2]
NGC4468	SA0-?	908	16.7 (1.1)	1.5/1.0	-17.57	0.054	3.0	4.5 (0.8)	0.6	0.14	2.2 (0.5)	0.12 (0.03)	12 (2) [1]
NGC4470	Sa?	2340	16.7 (1.1)	1.6/1.0	-19.82	1.170	0.0	2.0 (0.3)	0.4	0.34	0.6 (0.1)	0.03 (0.01)	0 (0) [1]
NGC4504	SA(s)cd	1000	11.7 (1.8)	4.4/2.7	-19.26 ^c	0.036	3.0	35.6 (6.0)	0.7	0.23	8.5 (2.9)	0.45 (0.15)	25 (5) [1]
NGC4522	SB(s)cd	2307	16.7 (1.1)	4.0/0.8	-19.84	0.300	10.0	3.7 (0.6)	0.4	0.34	1.1 (0.2)	0.06 (0.01)	170 (30) [3]
NGC4532	IBm	2012	16.7 (1.1)	2.6/0.9	-20.25	0.054	3.0	13.3 (2.3)	0.4	0.4	3.7 (0.8)	0.20 (0.04)	16 (3) [1]
UGC07739	Im	2039	13.6 (1.1)	1.3/1.2	-17.96	1.180	0.0	0.1 (0.0)	0.4	0.16	0.0 (0.0)	0.00 (0.00)	2 (0) [1]
IC3522	ImIII-IV	668	16.7 (1.1)	1.0/0.5	-15.01 ^c	0.052	3.0	1.1 (0.2)	1.2	0.05	1.1 (0.2)	0.06 (0.01)	170 (90) [3]
NGC4550	SB0	409	2.8 (0.4)	3.3/0.9	-17.38	0.062	6.0	4.5 (0.8)	0.6	0.13	0.1 (0.0)	0.00 (0.00)	6 (1) [1]
NGC4559	SAB(rs)cd	816	9.3 (1.4)	10.7/4.4	-20.42	-	4.2	139.2 (23.7)	1.2	0.42	26.0 (9.0)	1.38 (0.48)	6 (3) [2]
NGC4561	SB(rs)dm	1407	16.7 (1.1)	1.5/1.3	-18.96	0.070	6.0	17.4 (3.0)	0.8	0.24	9.3 (2.0)	0.49 (0.11)	32 (6) [1]
NGC4567	SA(rs)bc	2274	16.7 (1.1)	2.9/1.4	-20.69	1.130	0.0	10.2 (1.7)	0.4	0.46	2.6 (0.6)	0.14 (0.03)	17 (4) [1]
NGC4568	SA(rs)bc	2255	16.7 (1.1)	4.3/1.0	-21.07	1.130	0.0	24.4 (4.2)	0.4	0.52	5.6 (1.2)	0.29 (0.06)	23 (6) [1]
IC3583	SmIII	1121	16.7 (1.1)	2.2/1.1	-18.18	1.100	0.0	2.9 (0.5)	0.4	0.17	1.2 (0.3)	0.06 (0.01)	39 (10) [1]
NGC4569	SAB(rs)ab	-235	16.7 (2.5)	9.5/4.4	-15.17	-	0.0	11.1 (1.9)	0.3	0.05	4.6 (1.6)	0.25 (0.08)	3 (0) [1]
IC3591	SBmIII	1632	16.7 (1.1)	0.9/0.6	-17.76	0.029	3.0	3.9 (0.7)	0.6	0.13	2.0 (0.4)	0.11 (0.02)	36 (7) [1]
NGC4579	SAB(rs)b	1519	16.7 (2.5)	5.9/4.7	-21.54	-	4.5	67.8 (11.5)	2.0	0.54	68.2 (23.5)	3.62 (1.25)	13 (6) [2]
IC3617	SBmIII/BCD	2079	16.7 (1.1)	1.4/0.7	-18.24	1.130	0.0	2.2 (0.4)	0.4	0.18	0.8 (0.2)	0.04 (0.01)	125 (51) [1]
UGC07827	Im:	552	9.3 (1.4)	1.2/0.7	-	0.060	6.0	1.9 (0.3)	0.3	0.0	0.3 (0.1)	0.01 (0.00)	49 (10) [1]
NGC4595	SAB(rs)b?	604	16.7 (1.1)	1.7/1.1	-17.66	-	2.0	7.6 (1.3)	0.7	0.14	4.0 (0.9)	0.21 (0.05)	19 (5) [3]
NGC4594	SA(s)a	1024	9.8 (1.5)	8.7/3.5	-22.39	-	4.2	65.7 (11.2)	2.6	0.53	37.1 (12.8)	1.96 (0.68)	4 (2) [2]
NGC4625	SAB(rs)m	609	9.4 (1.4)	1.3/1.2	-17.35	0.027	3.0	15.1 (2.6)	0.6	0.11	2.4 (0.8)	0.13 (0.04)	25 (4) [3]
NGC4631	SB(s)d	606	7.7 (1.2)	15.5/2.7	-20.63	0.051	4.2	80.9 (13.8)	1.3	0.46	10.3 (3.6)	0.55 (0.19)	42 (3) [3]

Table 2: continued.

Galaxy	Class	v_{rec} km s ⁻¹	Dist. Mpc	a/b arcmin	M(B) mag	k	η %	$F(\text{H}\alpha + [\text{NII}])$ 10 ⁻¹³ erg cm ⁻² s ⁻¹	A_{T} mag	$\xi_{\text{obs}}^{\text{a}}$	$L(\text{H}\alpha)^{\text{b}}$ 10 ⁴⁰ erg s ⁻¹	SFR ^b $M_{\odot} \text{ yr}^{-1}$	EW Å
NGC4639	SAB(rs)bc	977	16.7 (1.1)	2.8/1.9	-19.08	0.440	0.0	10.1 (1.7)	0.4	0.24	3.6 (0.8)	0.19 (0.04)	38 (9) [1]
NGC4640	dS0	2082	16.7 (1.1)	1.6/0.8	-18.09 ^c	0.025	4.0	3.0 (0.5)	0.7	0.16	1.7 (0.4)	0.09 (0.02)	27 (5) [1]
NGC4647	SAB(rs)c	1334	16.7 (1.1)	2.9/2.3	-19.95	0.065	6.0	31.0 (5.3)	2.3	0.35	53.6 (11.5)	2.84 (0.61)	11 (2) [1]
NGC4651	SA(rs)c	805	16.7 (1.1)	4.0/2.6	-19.50	-	2.0	36.3 (6.2)	1.0	0.29	21.7 (4.7)	1.15 (0.25)	23 (2) [3]
PGC043211	dE	1146	13.6 (2.0)	0.7/0.7	-19.46	0.022	3.0	0.4 (0.1)	0.2	0.25	0.1 (0.0)	0.00 (0.00)	880 (233) [1]
NGC4725	SAB(r)ab	1206	11.9 (1.8)	10.7/7.6	-21.45	-	4.2	57.2 (9.7)	1.8	0.53	24.1 (8.3)	1.28 (0.44)	7 (3) [2]
NGC4736	(R)SA(r)ab	308	5.2 (0.8)	11.2/9.1	-20.40	0.043	3.0	297.3 (50.5)	1.4	0.41	19.9 (6.9)	1.05 (0.36)	10 (0) [3]
NGC4772	SA(s)a	998	13.4 (2.0)	3.4/1.7	-19.42	0.320	10.0	4.3 (0.7)	0.9	0.29	1.5 (0.5)	0.08 (0.03)	90 (10) [3]
NGC4789A	IB(s)m	374	3.8 (0.6)	3.0/2.2	-15.81	-	2.0	6.2 (1.0)	0.3	0.07	0.1 (0.0)	0.01 (0.00)	47 (5) [3]
NGC4826	(R)SA(rs)ab	408	7.5 (1.1)	10.0/5.4	-20.55	-	4.2	19.3 (3.3)	0.4	0.44	1.1 (0.4)	0.06 (0.02)	9 (1) [3]
NGC4941	(R)SAB(r)ab	1108	17.4 (2.6)	3.6/1.9	-19.58	0.025	3.0	27.2 (4.6)	1.1	0.26	20.3 (7.0)	1.08 (0.37)	26 (5) [1]
PGC045195	SAB(s)dm	1362	24.4 (3.7)	1.2/0.9	-19.26 ^c	0.063	6.0	30.8 (5.2)	0.7	0.27	30.3 (10.4)	1.60 (0.55)	68 (14) [1]
UGC08201	Im	31	4.6 (0.7)	3.5/1.9	-13.12	-	2.0	2.1 (0.3)	0.2	0.02	0.1 (0.0)	0.00 (0.00)	10 (2) [3]
UGC08303	IAB(s)m	929	18.1 (2.7)	2.2/1.9	-17.55	-	2.0	7.2 (1.2)	0.5	0.13	3.9 (1.3)	0.21 (0.07)	63 (6) [3]
NGC5033	SA(s)c	875	16.2 (2.4)	10.7/5.0	-20.16	0.033	3.0	97.4 (16.6)	0.8	0.33	41.3 (14.2)	2.19 (0.75)	31 (6) [1]
ESO508-030	IB(s)m	1510	23.1 (3.5)	1.7/0.6	-17.26 ^c	0.018	1.5	4.7 (0.8)	0.6	0.05	5.1 (1.8)	0.27 (0.09)	74 (15) [1]
NGC5055	SA(rs)bc	504	7.9 (1.2)	12.6/7.2	-20.57	-	4.2	19.8 (3.4)	0.7	0.45	1.6 (0.5)	0.08 (0.03)	20 (4) [3]
NGC5194	SA(s)bc	463	7.7 (1.2)	11.2/6.9	-20.75	-	4.2	737.0 (125.3)	1.4	0.48	101.6 (35.0)	5.39 (1.86)	28 (3) [3]
NGC5195	SB0.1	465	7.7 (1.2)	5.8/4.6	-19.26	-	4.2	48.7 (8.3)	1.1	0.27	6.9 (2.4)	0.37 (0.13)	4 (1) [3]
NGC5474	SA(s)cd	273	6.5 (1.0)	4.8/4.3	-17.39	-	2.0	26.1 (4.4)	0.5	0.12	1.8 (0.6)	0.10 (0.03)	22 (2) [3]
NGC5477	SA(s)m	304	7.1 (1.1)	1.7/1.3	-14.46	-	3.0	7.0 (1.2)	0.2	0.04	0.5 (0.2)	0.03 (0.01)	92 (9) [3]
NGC5486	SA(s)m	1386	25.6 (3.8)	1.7/1.0	-17.80 ^c	-	1.8	5.0 (0.8)	0.6	0.14	5.8 (2.0)	0.31 (0.11)	35 (3) [3]
PGC140287	Im	1470	25.5 (3.8)	1.0/0.7	-15.27 ^d	0.025	6.0	0.3 (0.0)	1.2	0.05	0.6 (0.2)	0.03 (0.01)	130 (26) [1]
IC1024	S0?	1411	25.0 (3.8)	1.6/0.6	-17.97 ^c	0.018	3.0	10.0 (1.7)	0.4	0.15	9.1 (3.1)	0.48 (0.17)	48 (10) [1]
NGC5701	(R)SB(rs)0/a	1524	25.8 (3.9)	4.3/4.1	-20.12	0.012	1.5	28.6 (4.9)	1.2	0.14	57.8 (19.9)	3.07 (1.06)	20 (4) [1]
IC1066	Sab	1577	26.5 (4.0)	1.3/0.7	-17.82 ^c	0.061	6.0	7.2 (1.2)	0.4	0.15	7.6 (2.6)	0.40 (0.14)	33 (6) [1]
PGC057723	SAB(r)b?	934	16.4 (2.5)	2.4/1.7	-18.11 ^c	0.065	6.0	22.6 (3.8)	1.3	0.17	19.6 (6.7)	1.04 (0.36)	35 (7) [1]
NGC6140	SB(s)cd	866	18.8 (2.8)	6.3/4.6	-18.73	0.020	3.0	84.1 (14.3)	0.4	0.2	39.8 (13.7)	2.11 (0.73)	8 (2) [1]
NGC6118	SA(s)cd	1611	25.7 (3.9)	4.7/2.0	-19.37	0.066	6.0	27.2 (4.6)	1.2	0.28	46.0 (15.9)	2.44 (0.84)	19 (4) [1]
PGC058661	Sc	1581	25.6 (3.8)	1.6/0.5	-16.64 ^c	0.064	6.0	1.3 (0.2)	1.3	0.09	3.2 (1.1)	0.17 (0.06)	30 (6) [1]
IC1254	Sb?	1283	24.0 (3.6)	1.6/0.7	-16.16	0.017	3.0	2.4 (0.4)	0.4	0.07	2.2 (0.8)	0.12 (0.04)	23 (5) [1]
NGC7465	(R)SB(s)	1972	30.1 (4.5)	1.2/0.8	-18.41	0.012	1.1	6.8 (1.2)	1.0	0.04	17.7 (6.1)	0.94 (0.32)	17 (3) [1]
NGC7742	SA(r)b	1663	25.2 (3.8)	1.7/1.7	-18.90 ^c	0.013	1.1	8.0 (1.4)	0.4	0.05	8.8 (3.0)	0.46 (0.16)	8 (2) [1]

^a [NII]/H α ratio corrected for the transmission profile of the H α filter used (see Section 5.6.).

^b Corrected for Galactic foreground absorption and internal absorption using $A_{\text{T}} = A(R) + A(\text{H}\alpha)$ (see Section 5.7).

^c From NED.

^d From LEDA (Paturel et al. 2003).

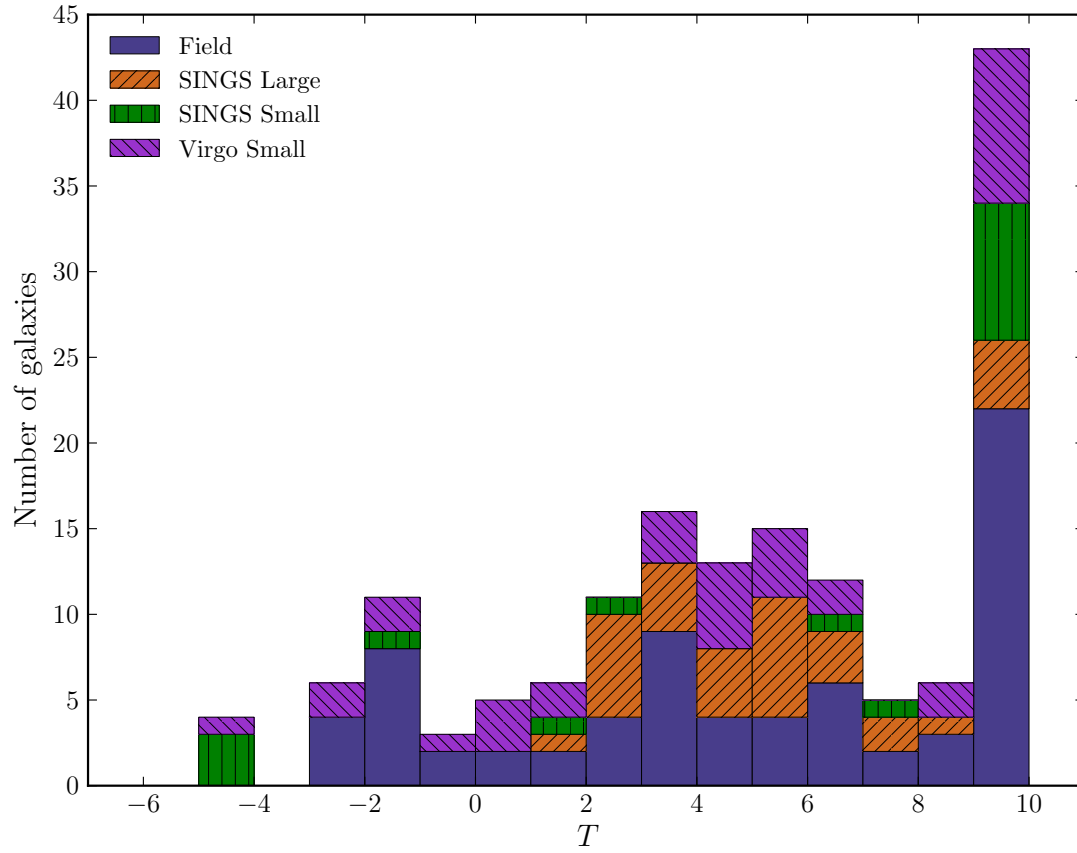


Figure 1. Histogram of the number of galaxies as a function of the Hubble stage, T , as listed in the Third Reference Catalogue of Bright Galaxies (RC3). The four different subsamples are shown with different patterns and colors.

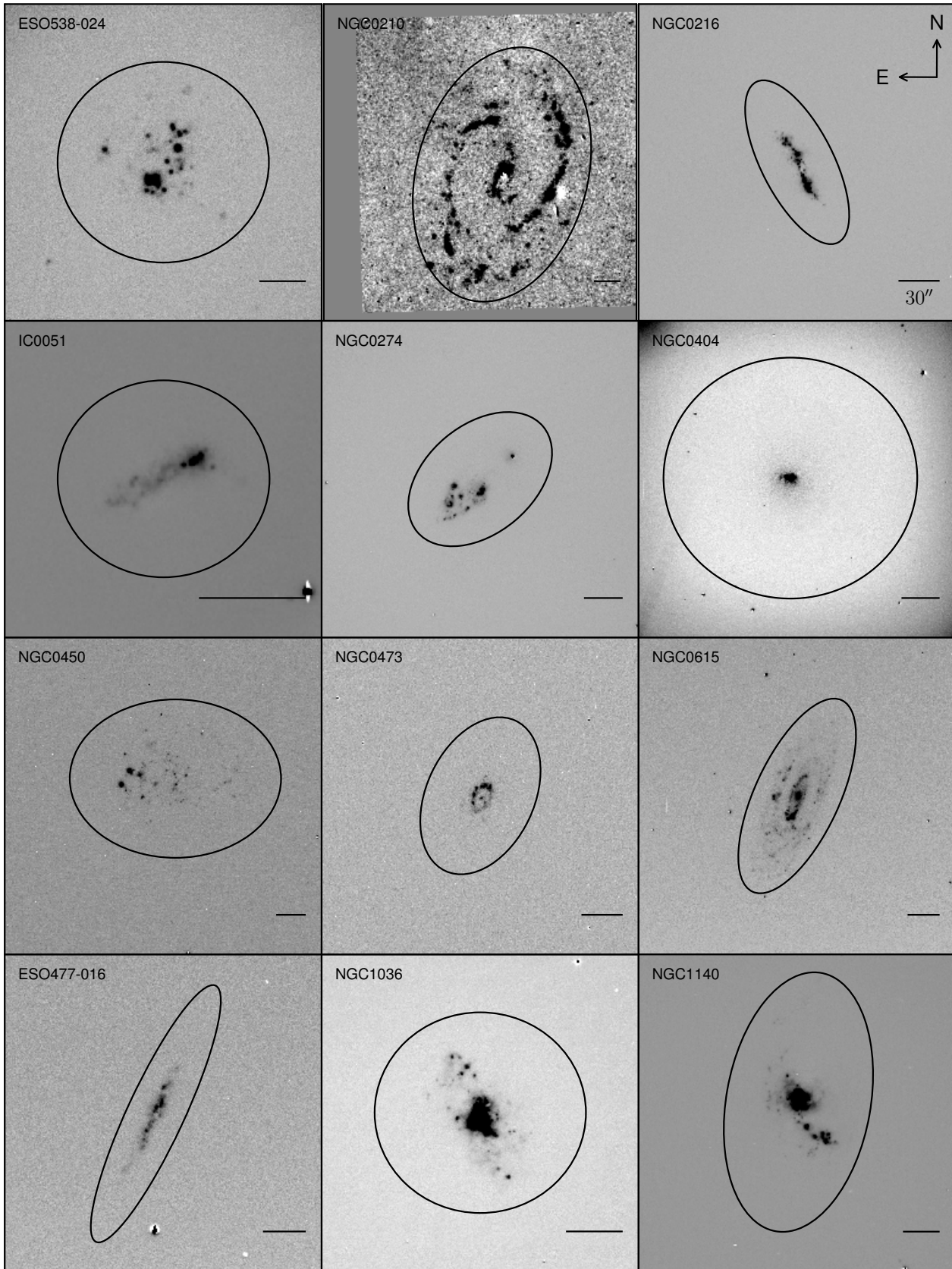


Figure 2. $H\alpha$ continuum-subtracted images of the field galaxies of our sample. The ellipse shows the aperture used to perform the photometry (see Section 5.5). All the images are oriented North up, East to the left. The right bottom line is always 30 arcsec.

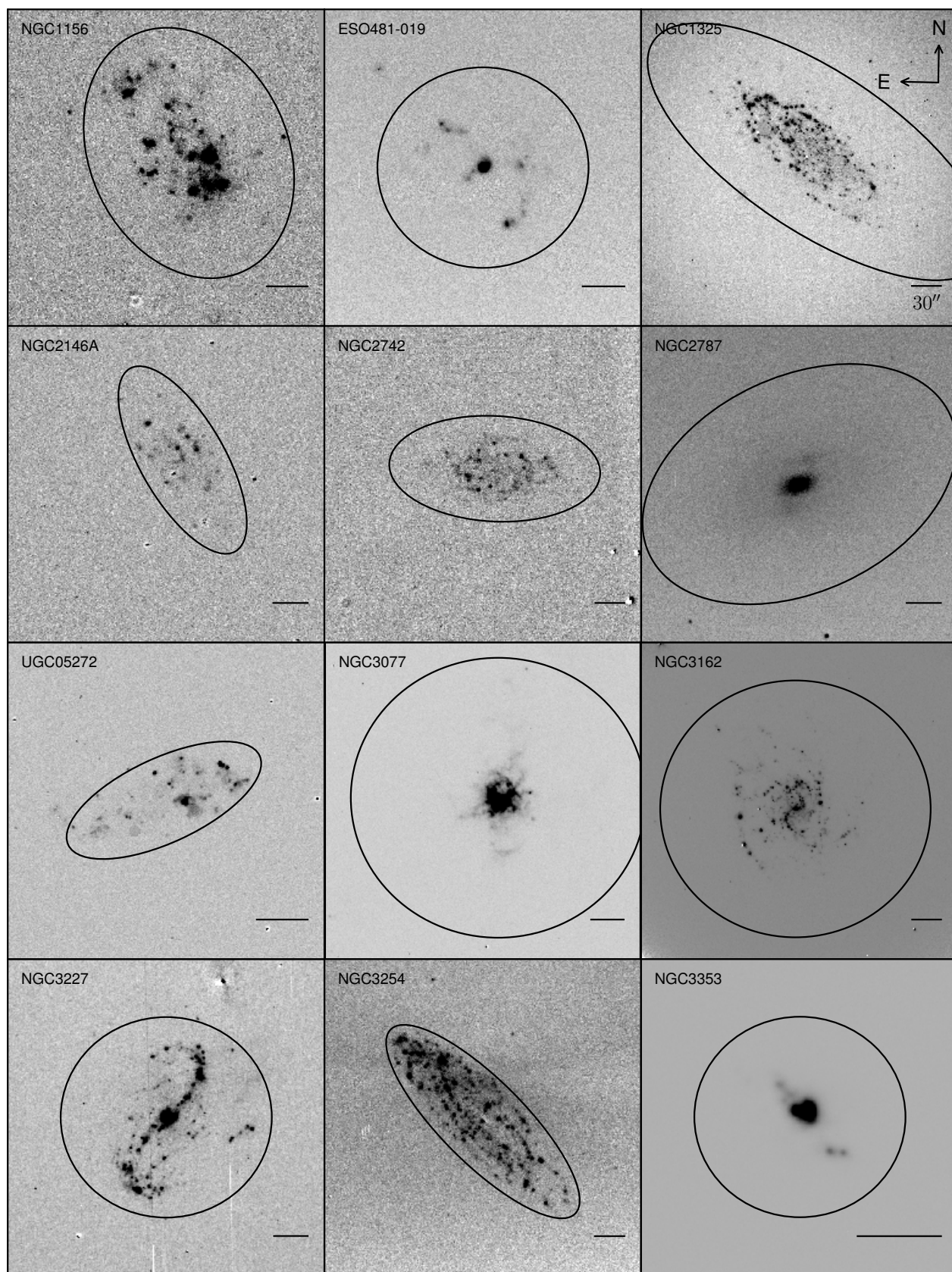


Figure 2. Continued

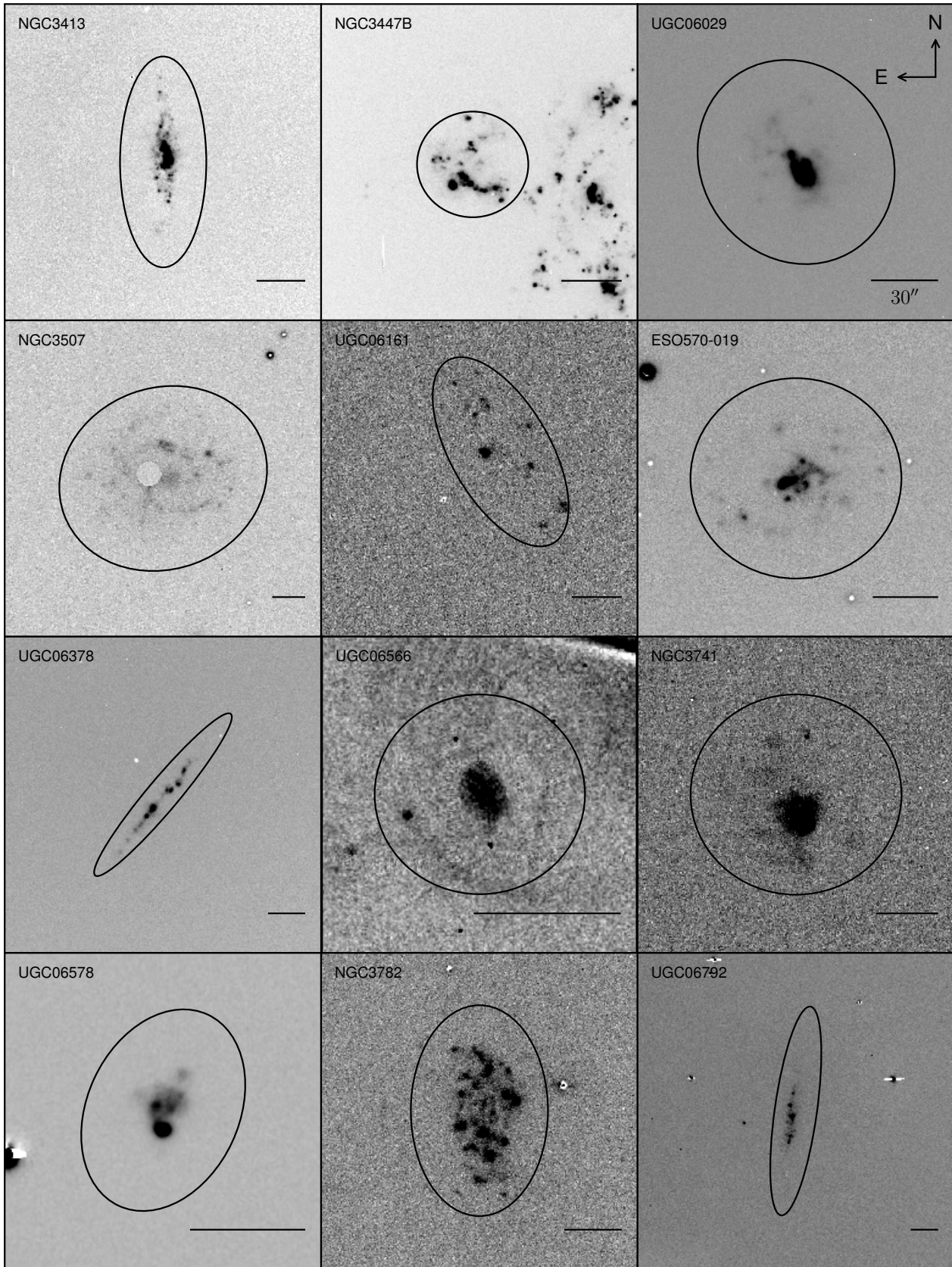


Figure 2. Continued

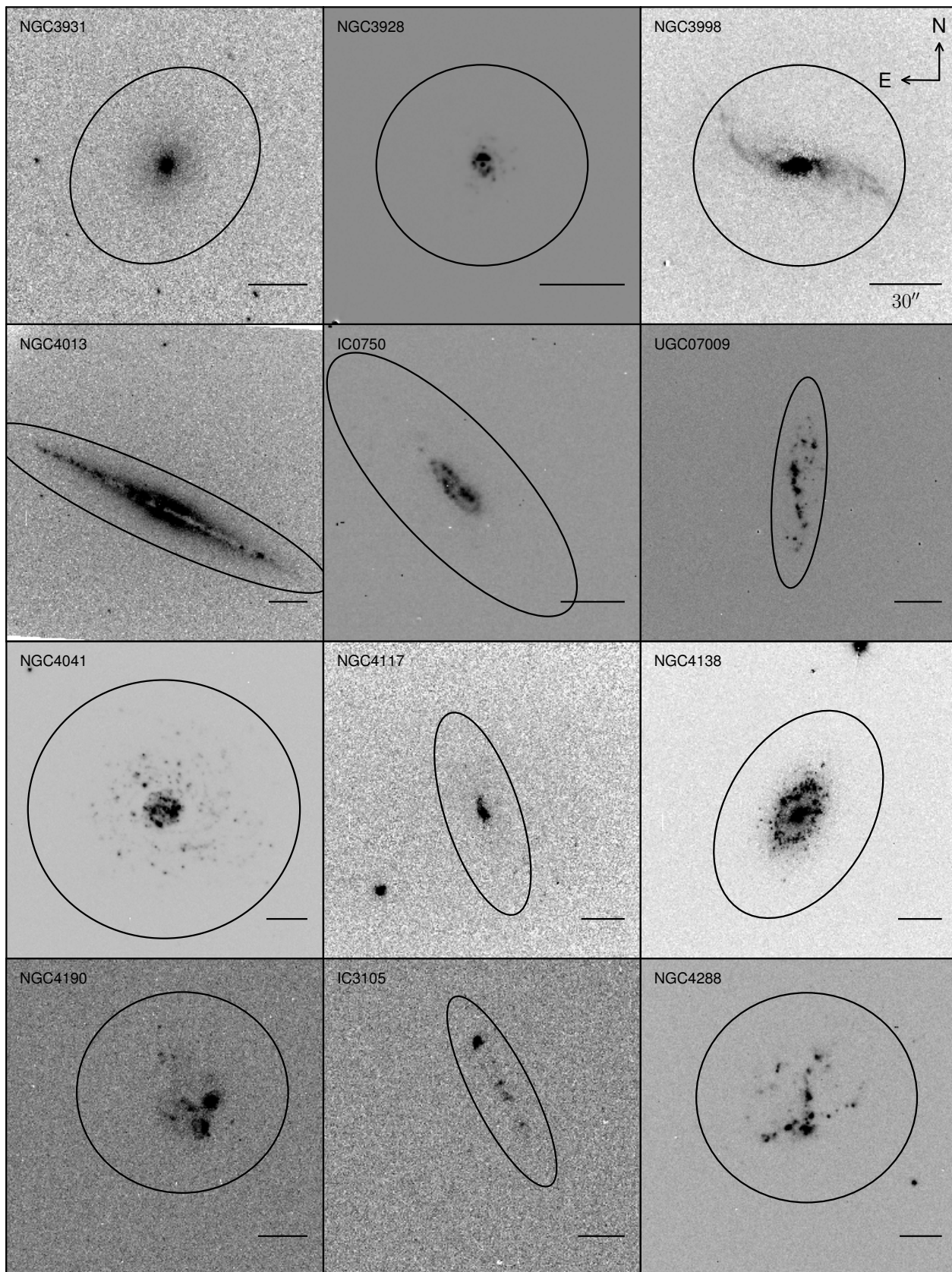


Figure 2. Continued

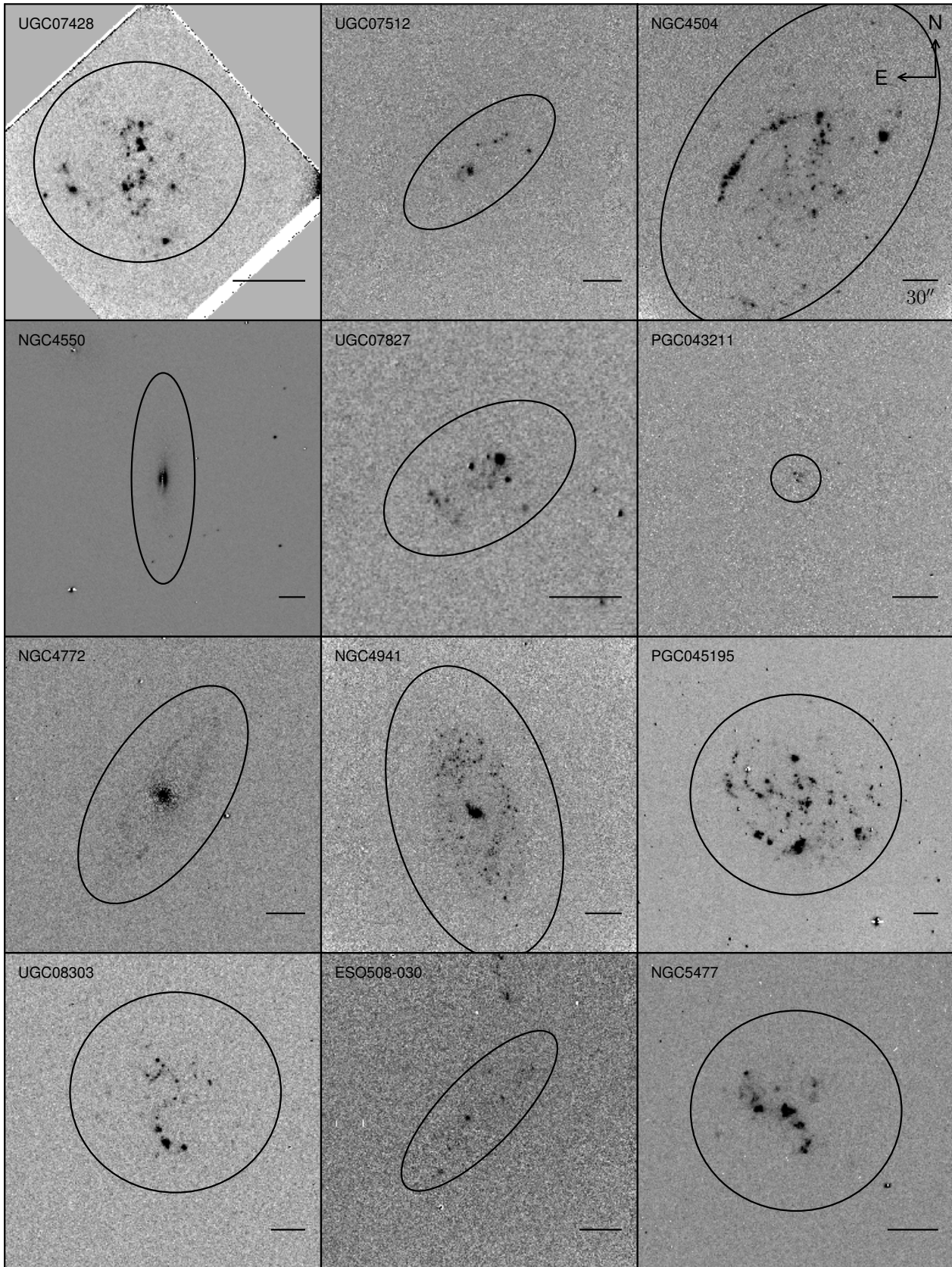


Figure 2. Continued

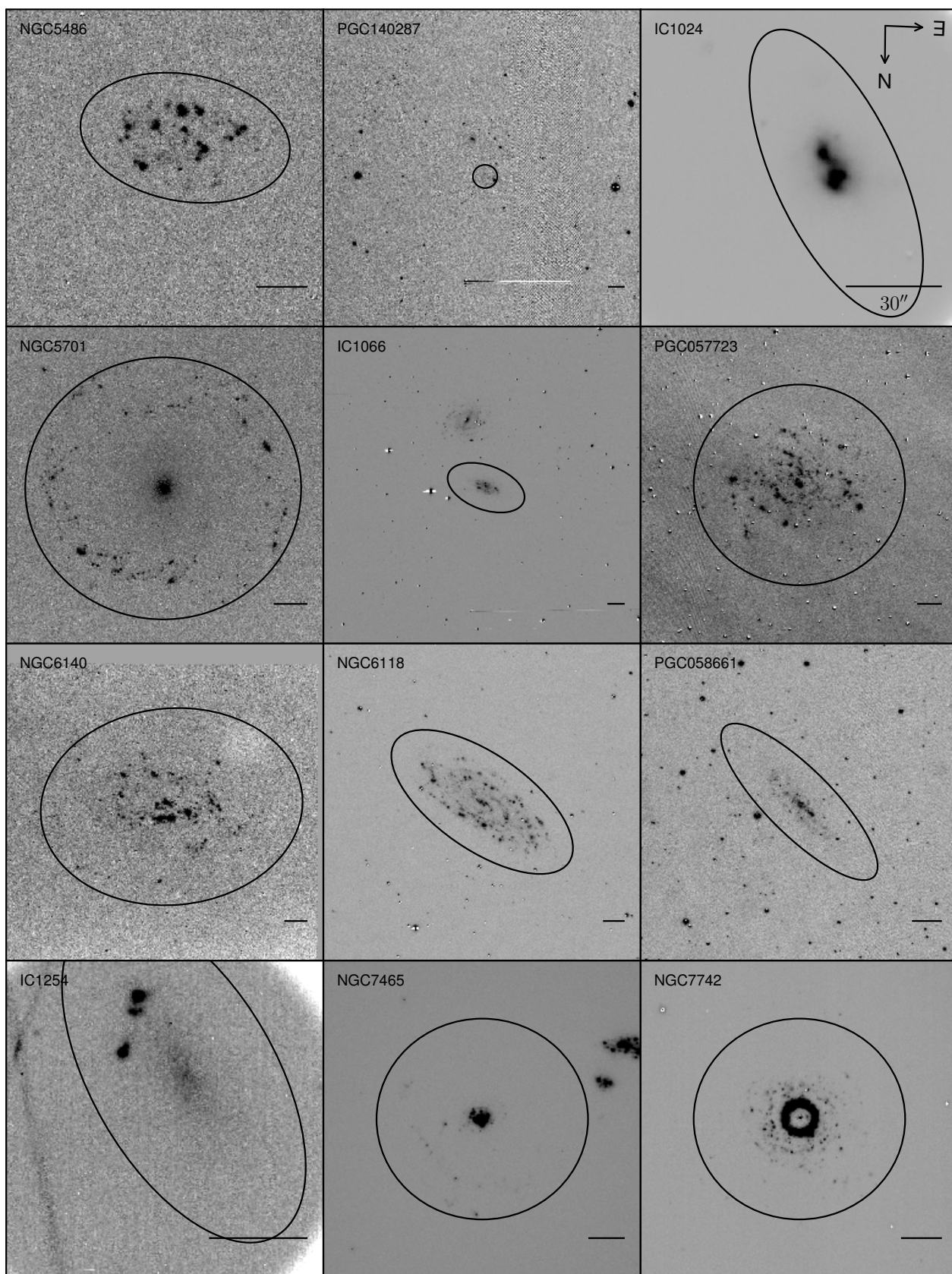


Figure 2. Continued

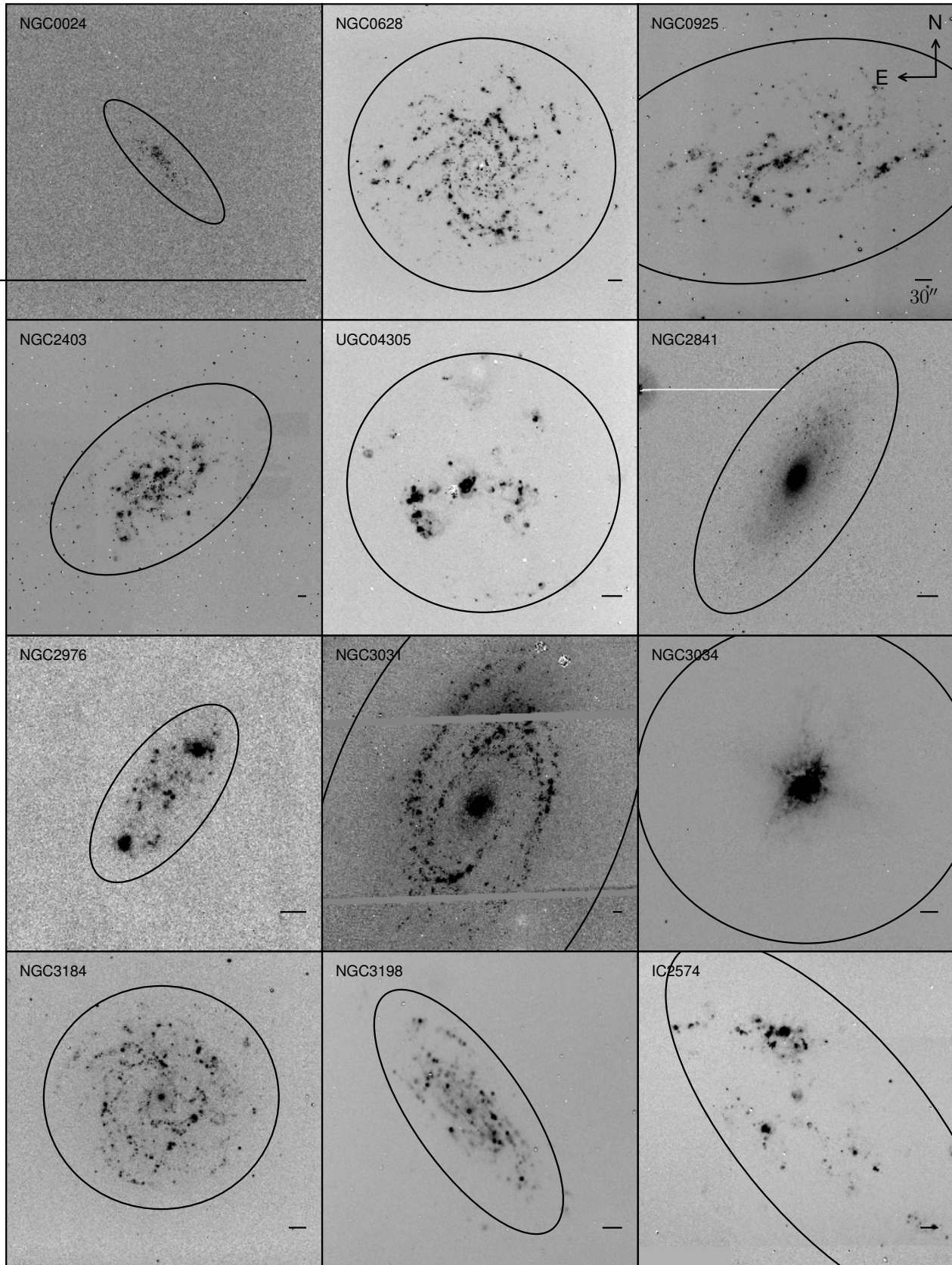


Figure 3. As Figure 2 but now for the SINGS Large galaxies in our sample.

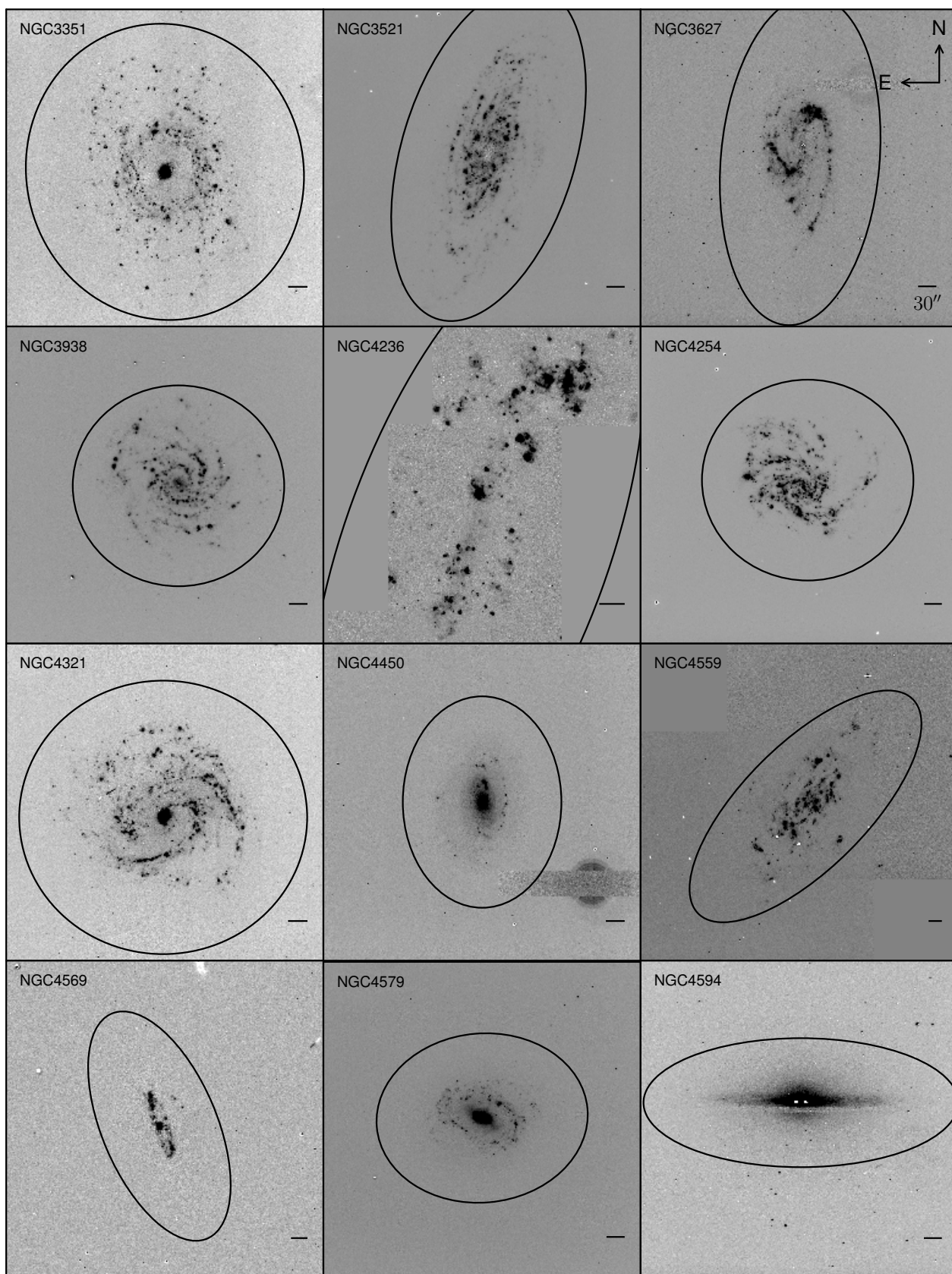


Figure 3. Continued

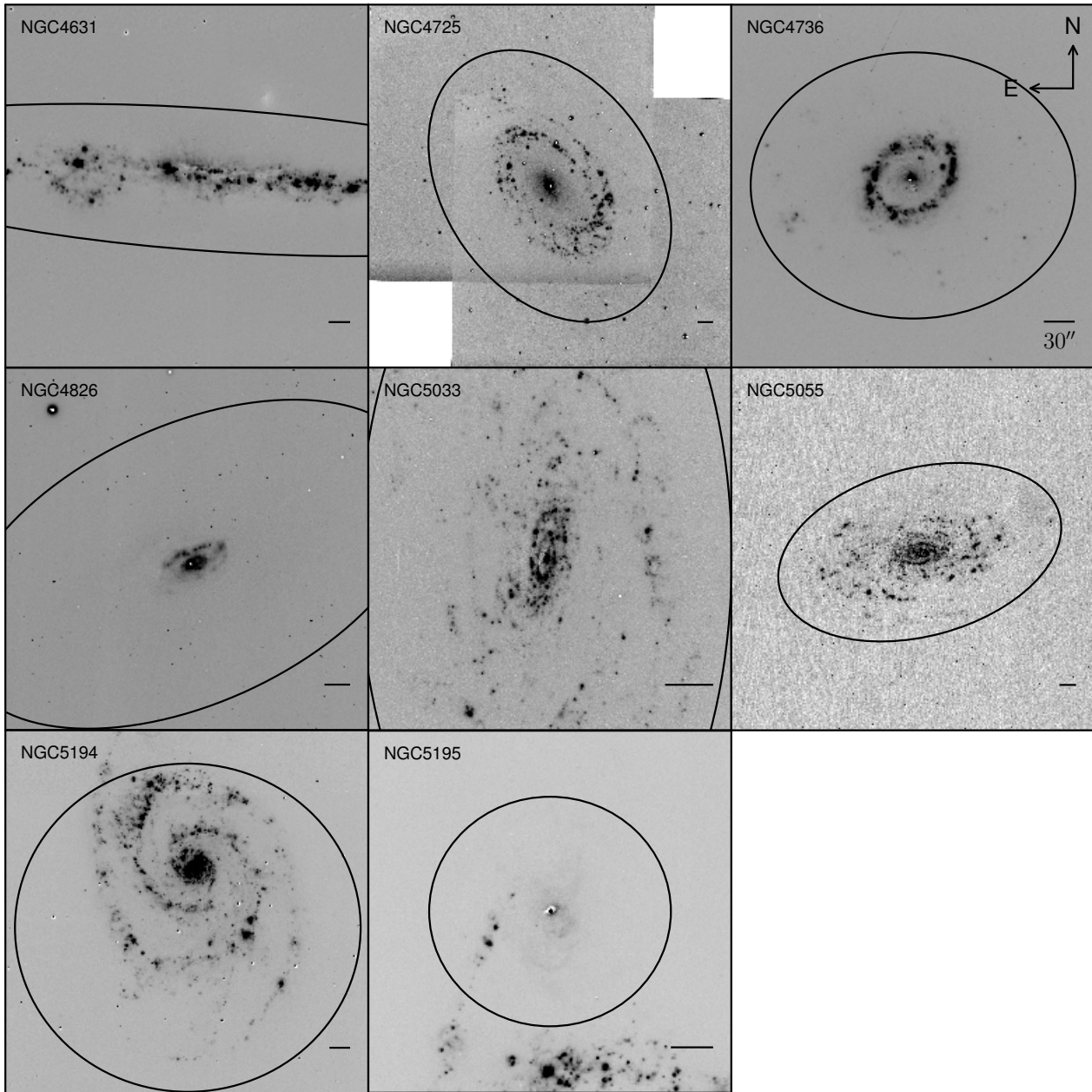


Figure 3. Continued

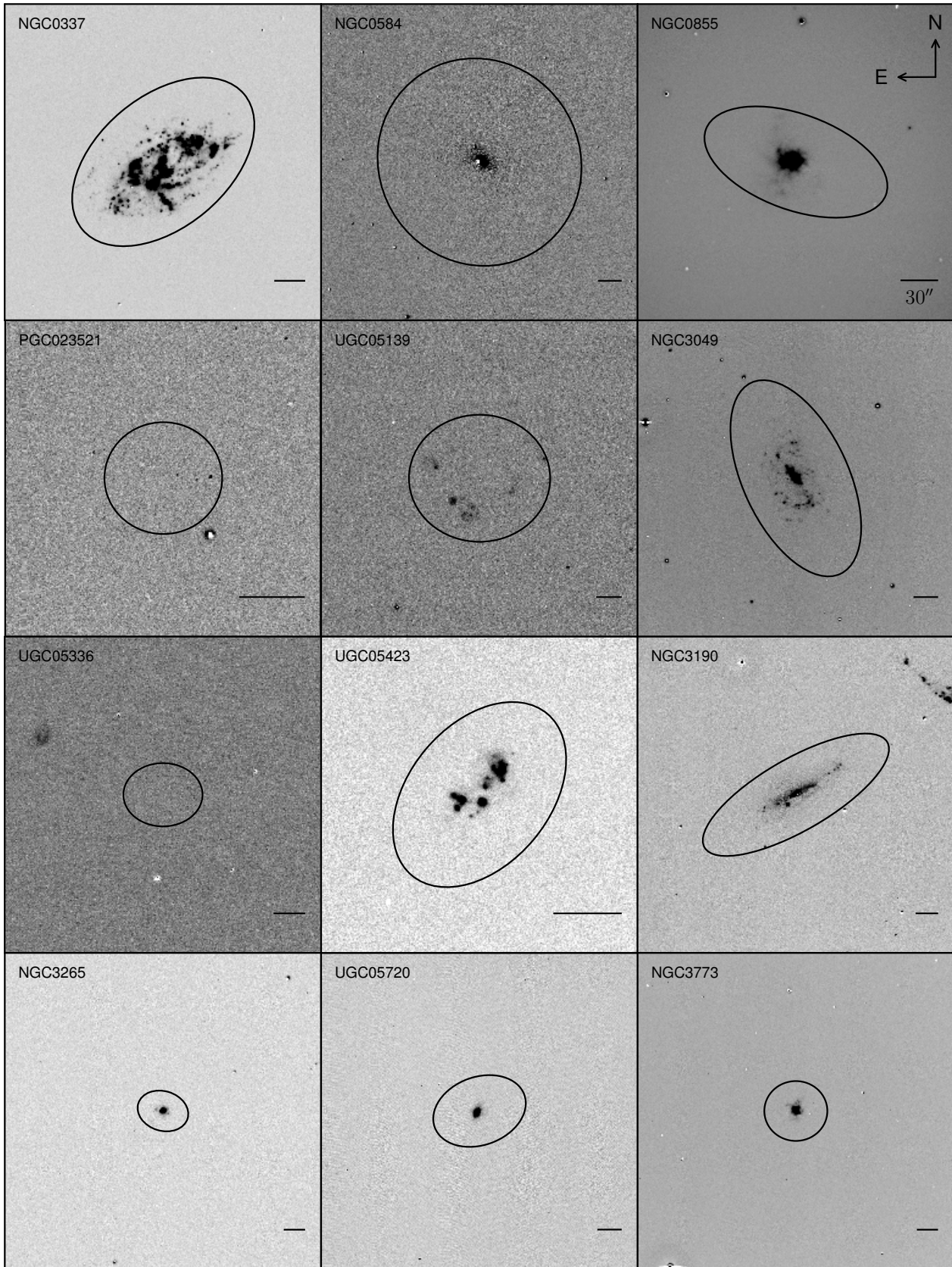


Figure 4. As Figure 2 but now for the SINGS Small galaxies in our sample.

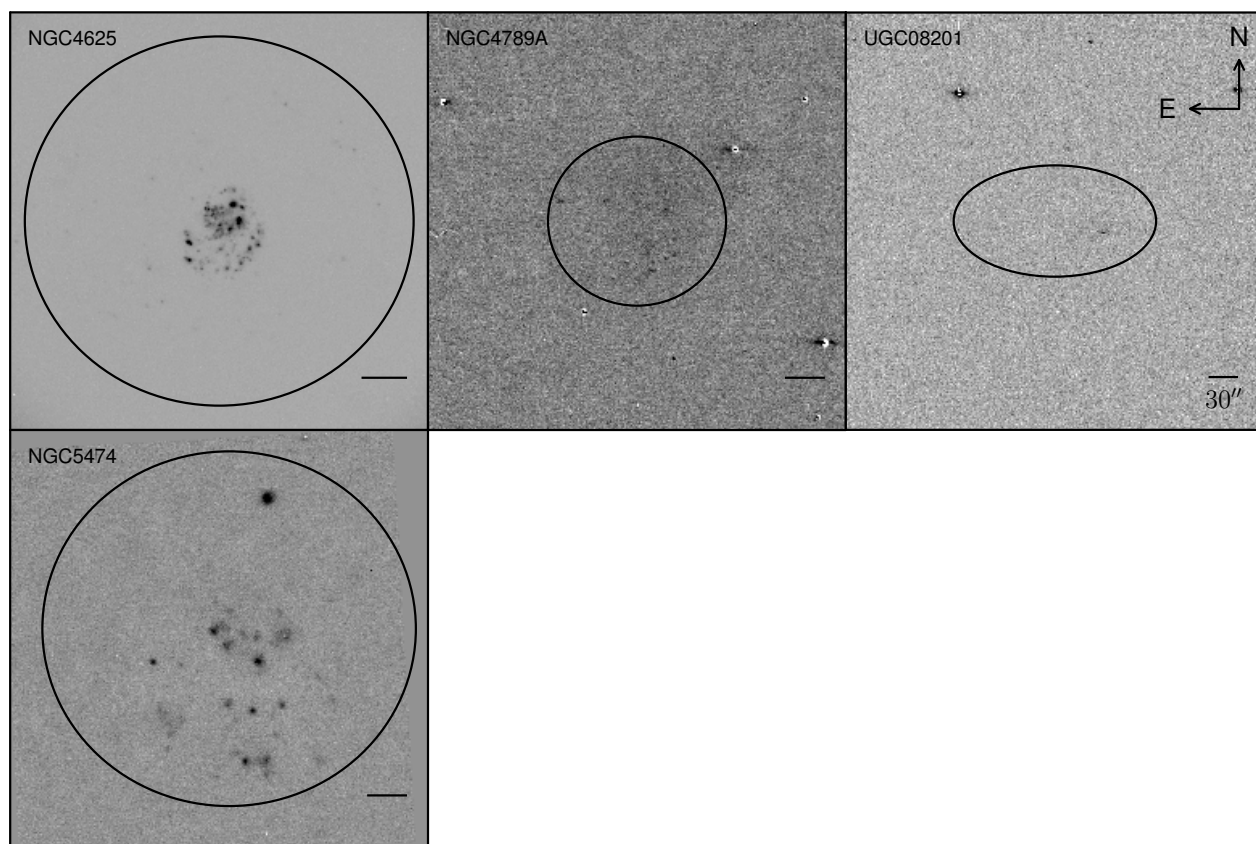


Figure 4. Continued

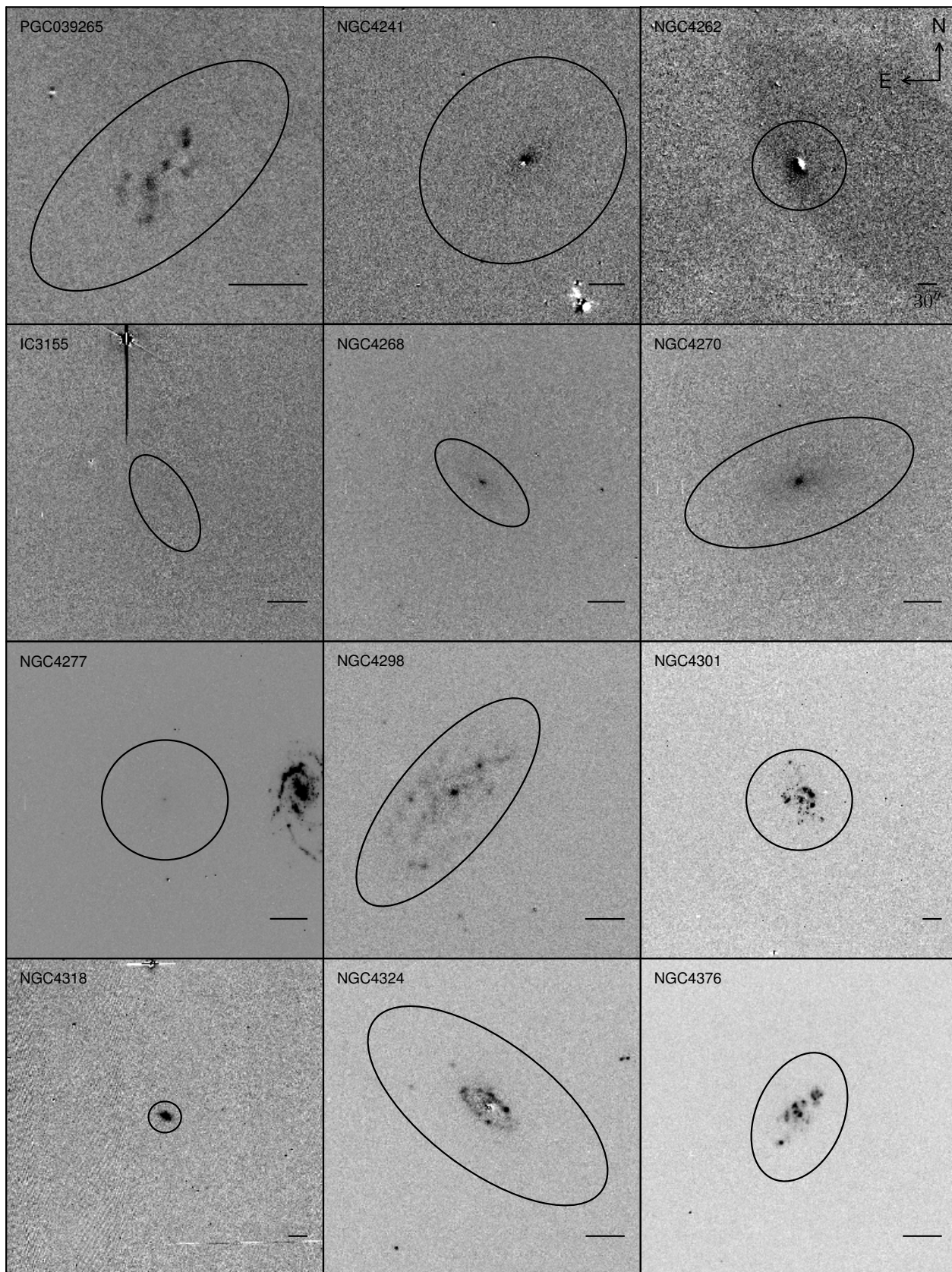


Figure 5. As Figure 2 but now for the Virgo Small galaxies in our sample.

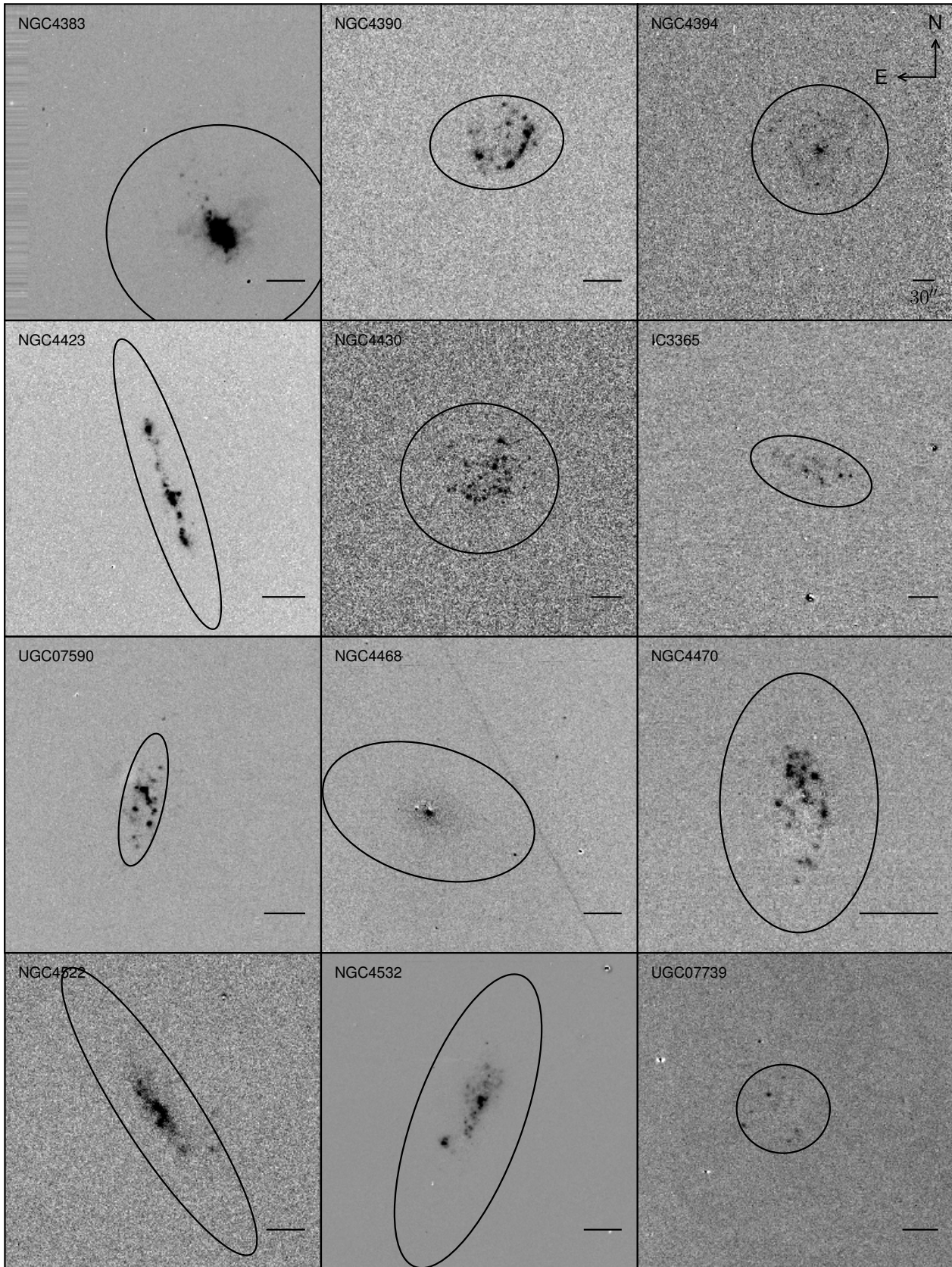


Figure 5. Continued

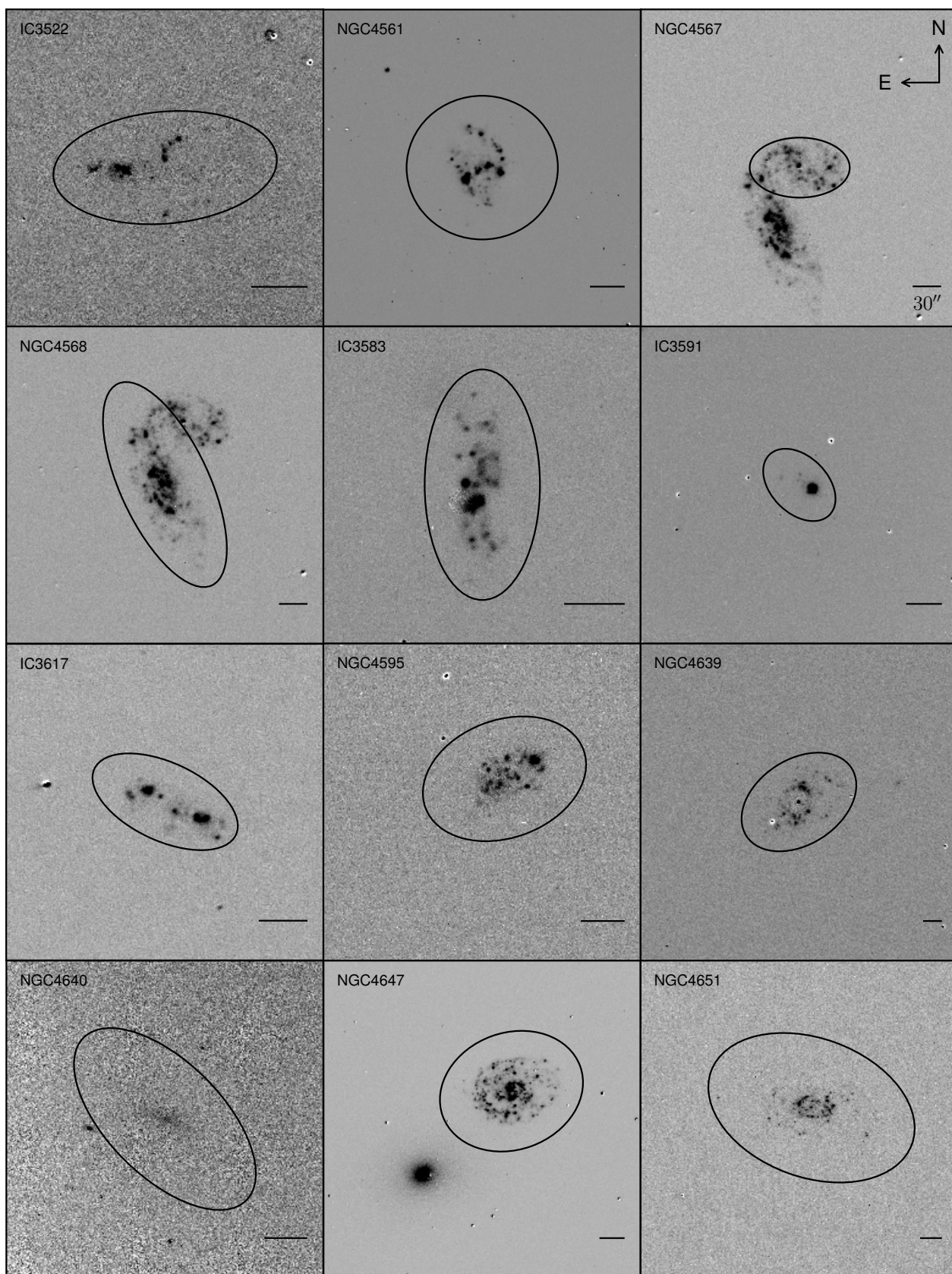


Figure 5. Continued

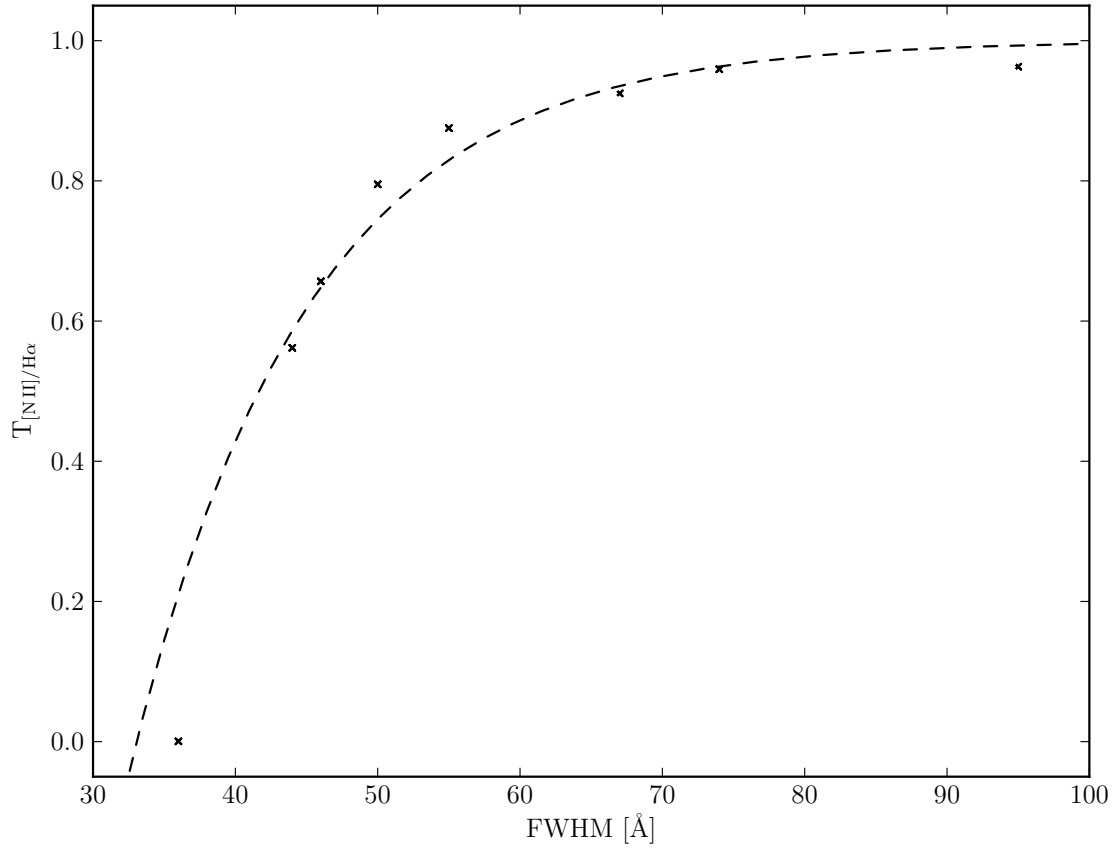


Figure 6. Relation between the transmission of the $H\alpha$ and $N\text{ II}$ lines for different narrow filters used in this work, as a function of the filter width. The dashed line indicates the exponential fit obtained (see Section 5.6).

This paper has been typeset from a \TeX / \LaTeX file prepared by the author.

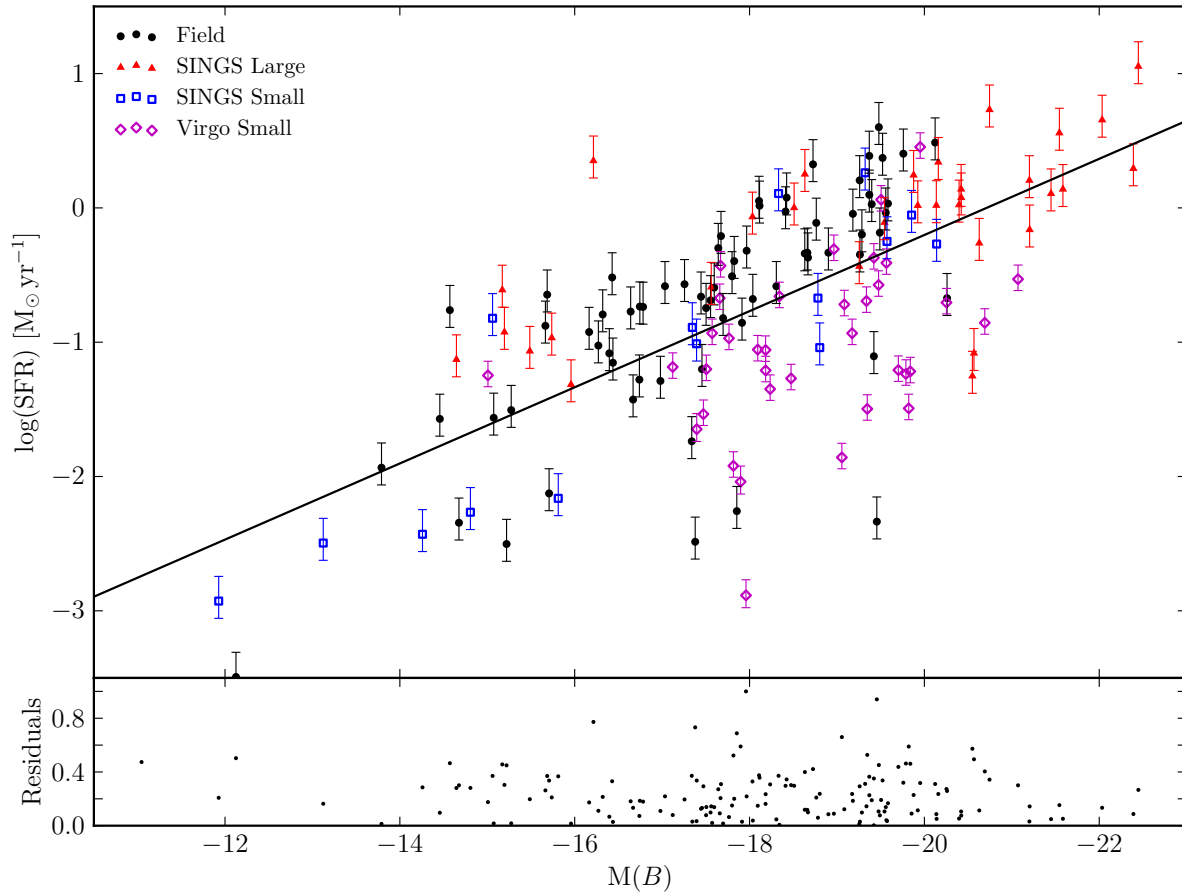


Figure 7. Logarithm of the SFR (in units of solar masses per year) versus the absolute B magnitude of the galaxies in our sample. The four subsamples which constitute the complete list are marked with different colors and symbols. The black solid line indicates the least squares regression fit for the plotted data. The lower plot shows the normalized root mean square of each galaxy to its fitted value.

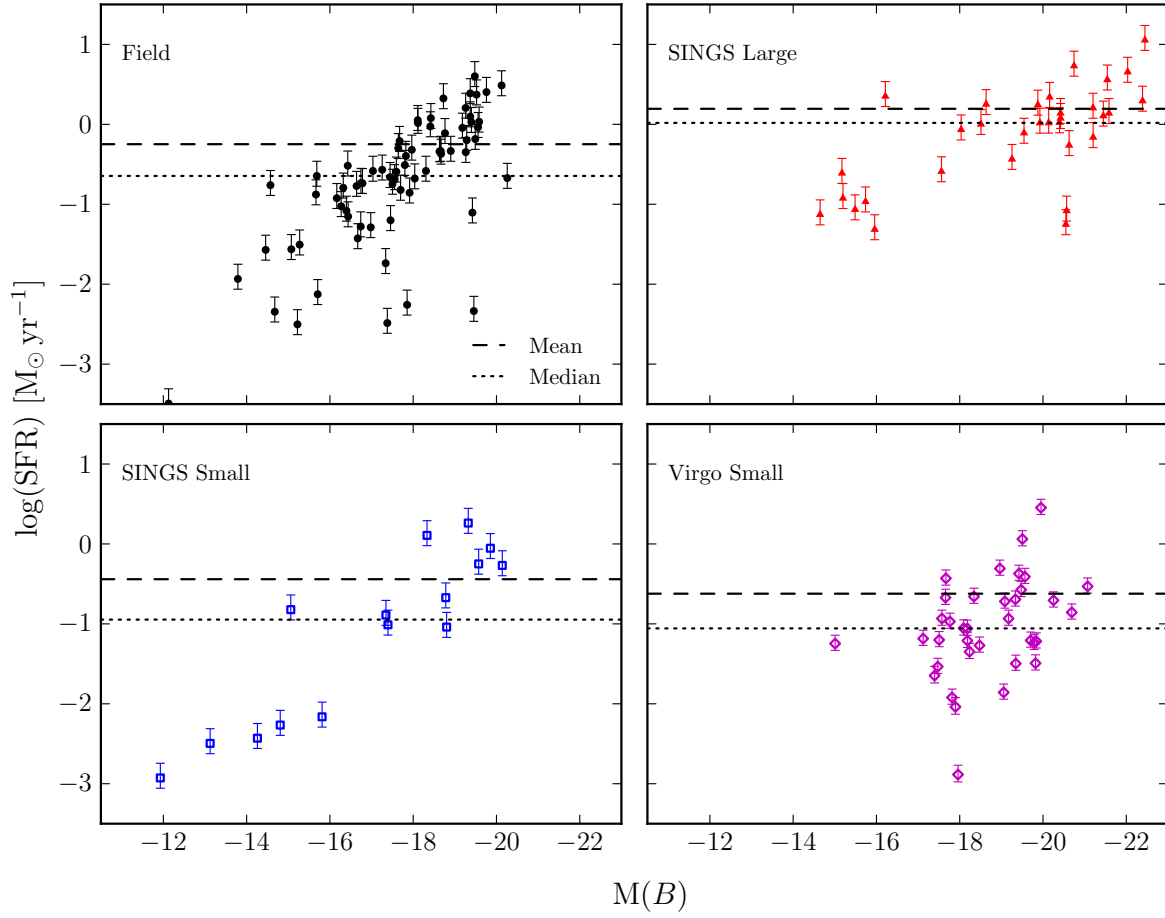


Figure 8. As Figure 7 but now with the subsamples divided into different panels. The dashed lines indicate the mean values of $\log(\text{SFR})$ for each subsample while the dotted ones indicate the median values.

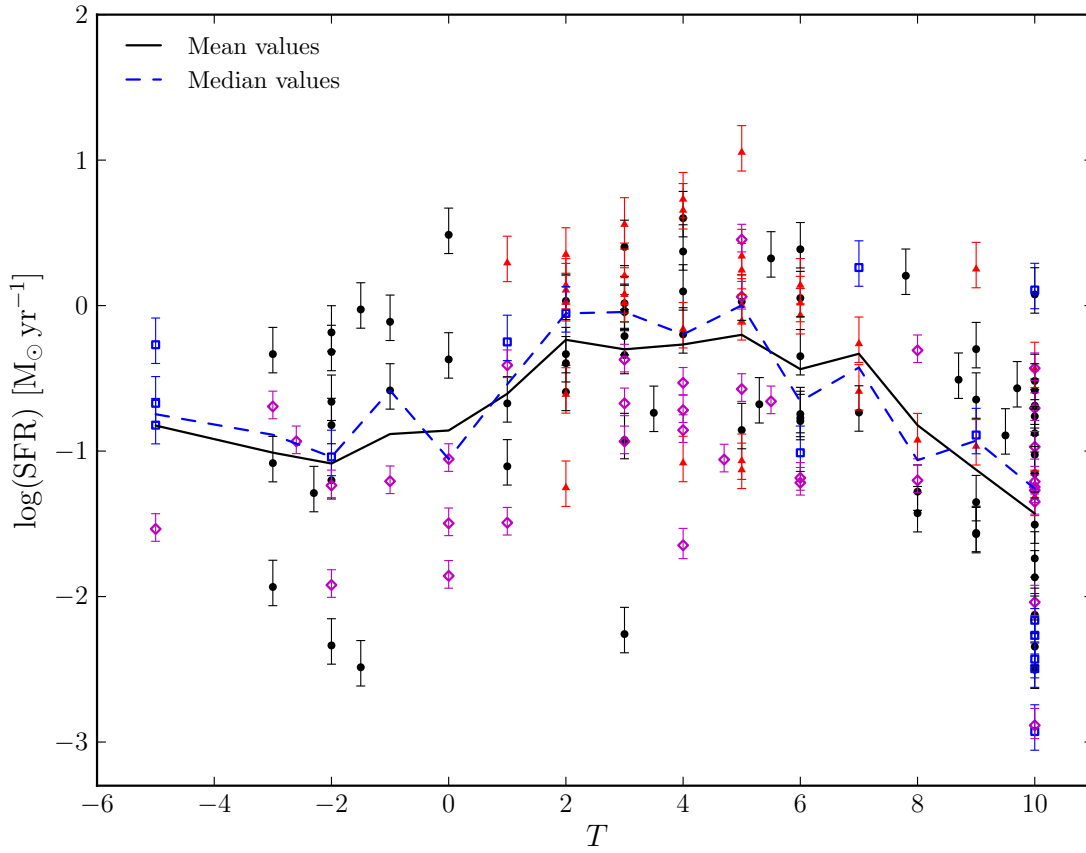


Figure 9. Logarithm of the SFR (in units of solar masses per year) versus the Hubble stage of the galaxies in the sample. The different subsamples in our complete list are plotted separately. The solid black line shows the mean values of the data binned to $\Delta T = 1$. The dashed blue line shows the median values calculated with the same procedure.

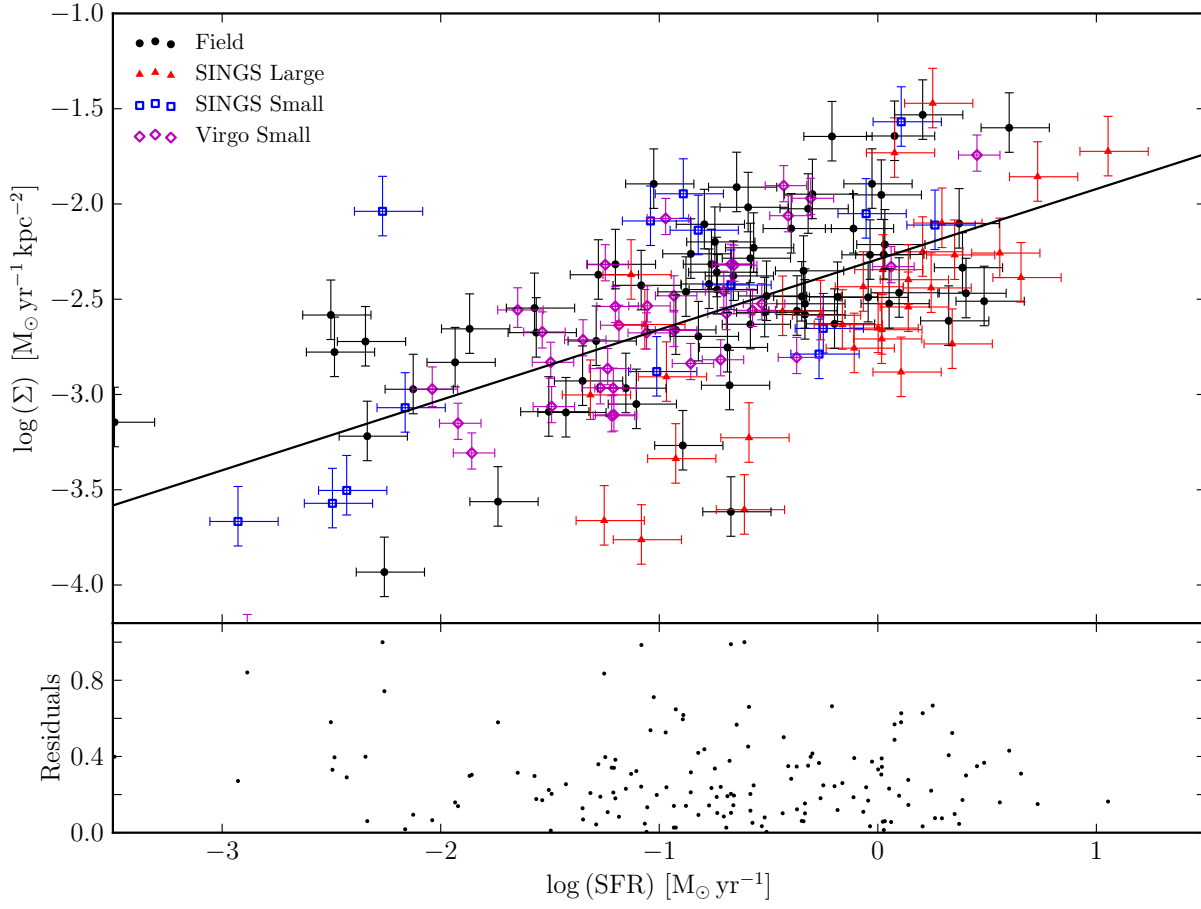


Figure 10. As Figure 7 but now plotting the logarithm of Σ in units of solar masses per year and per square kiloparsec versus the SFR in units of solar masses per year.

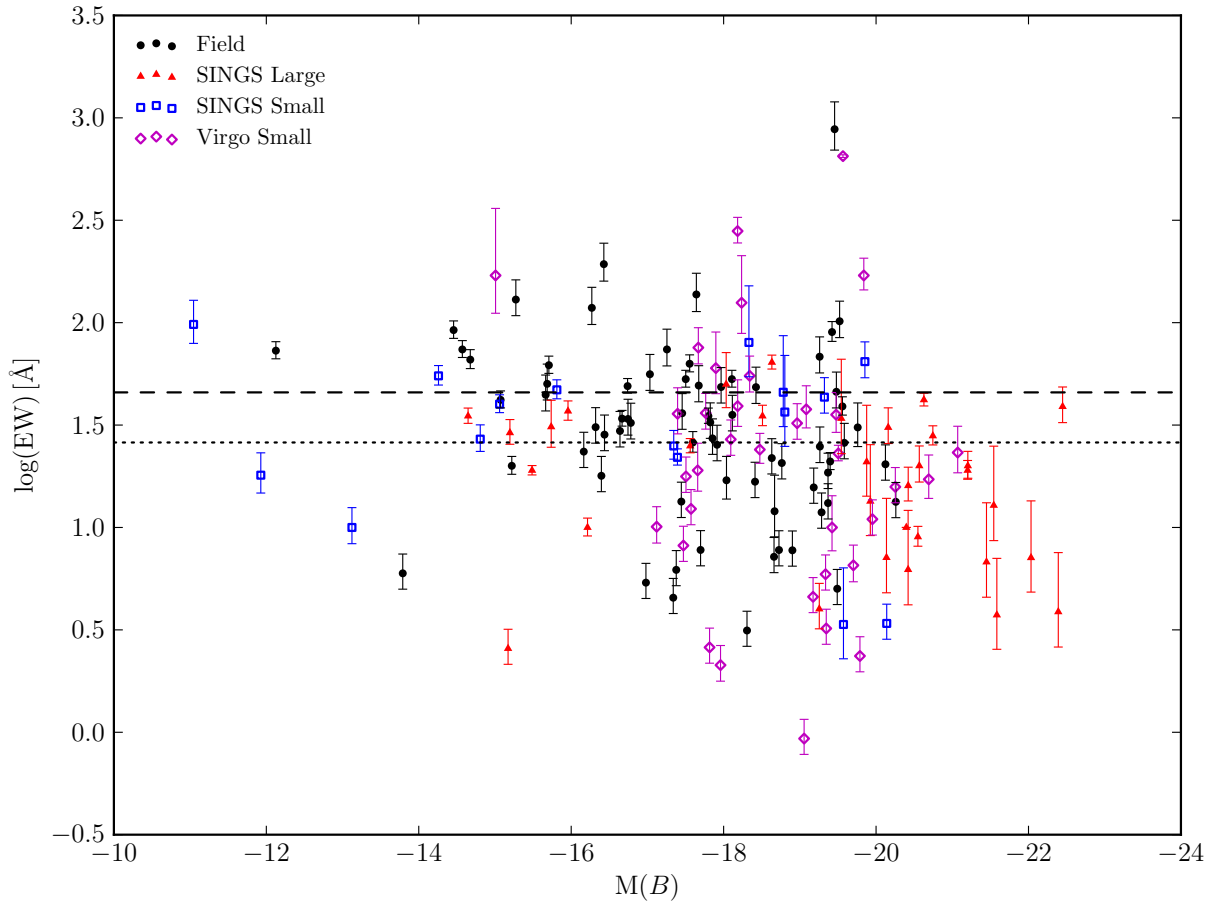


Figure 11. As Figure 7 but now with the logarithm of the equivalent width in Ångström. The dashed line indicates the mean value of $\log(\text{EW})$ for the full sample while the dotted one indicates the median value.

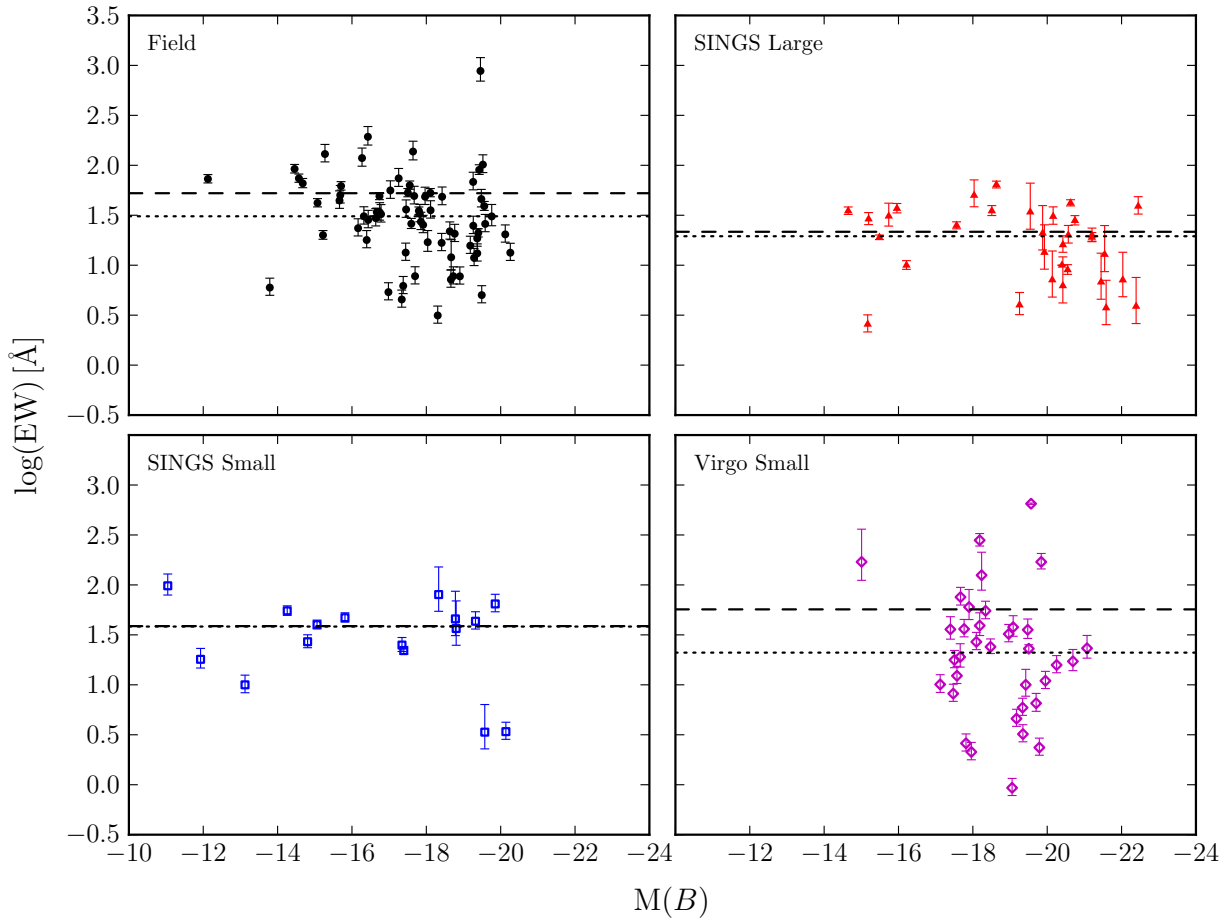


Figure 12. As Figure 11 but now with the subsamples divided into different panels.

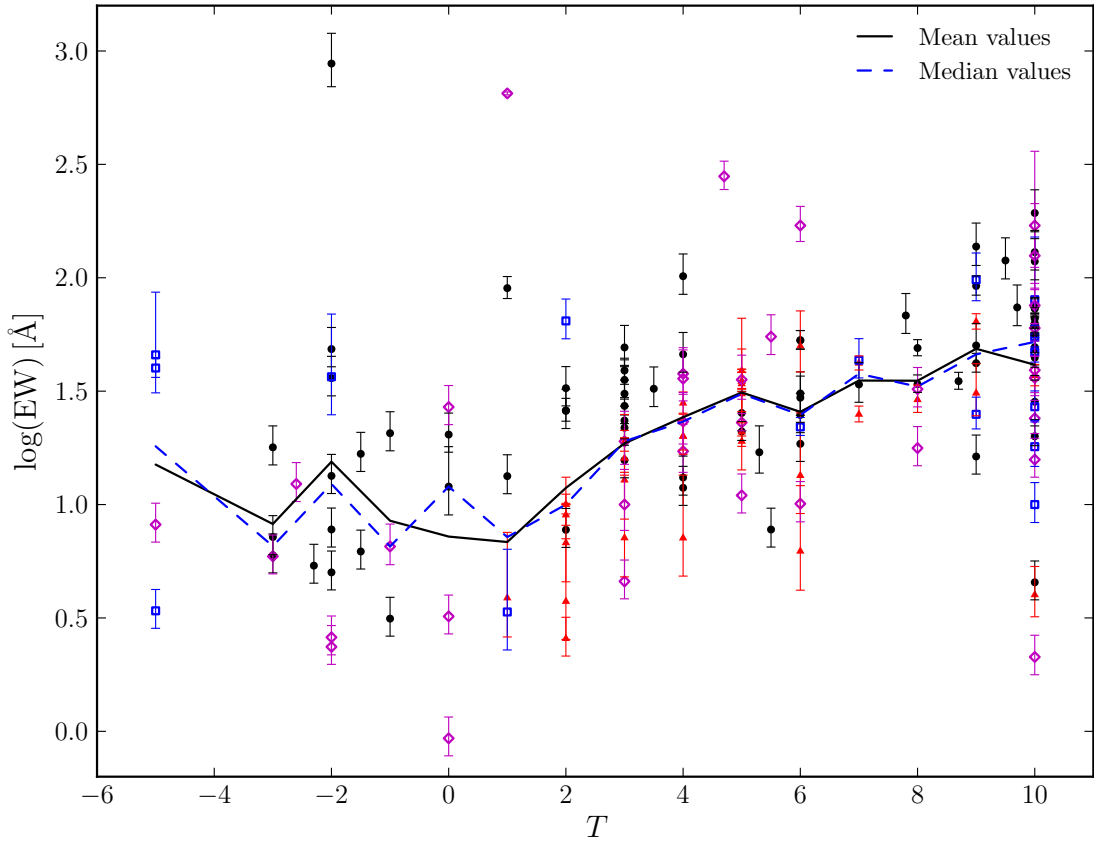


Figure 13. As Figure 9 but now with the logarithm of the equivalent width in Ångström.

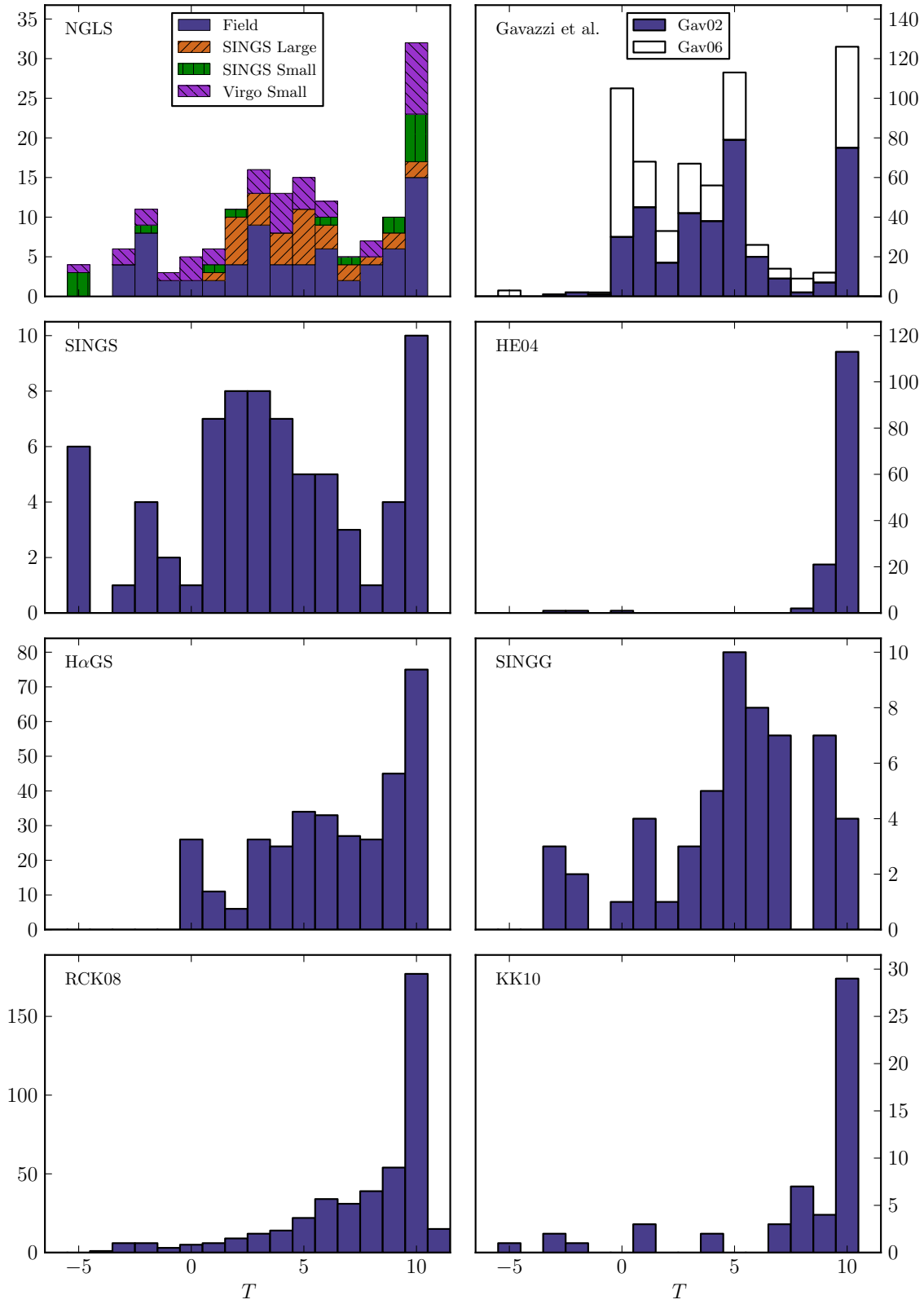


Figure 14. Histograms comparing the RC3 Hubble stage distribution, T , of our sample (top left panel) with several samples found in the literature: the Gavazzi et al. (2002, 2006) survey of nearby galaxy clusters, the SINGS sample (Kennicutt et al. 2003), the sample of irregular and Sm galaxies observed by Hunter & Elmegreen (2004), the H α GS survey (James et al. 2004), the SINGG survey (Meurer et al. 2006), the volume-limited sample within 11 Mpc studied by Kennicutt et al. (2008) and the 52 galaxies observed in H α by Karachentsev & Kaisin (2010) as part of a larger Local Volume survey. Note that the last bin in each histogram includes the galaxies with values of T larger than the upper limit in the plot. Further details are given in the text of Section 7.
 © 2011 RAS, MNRAS 000, 1–35

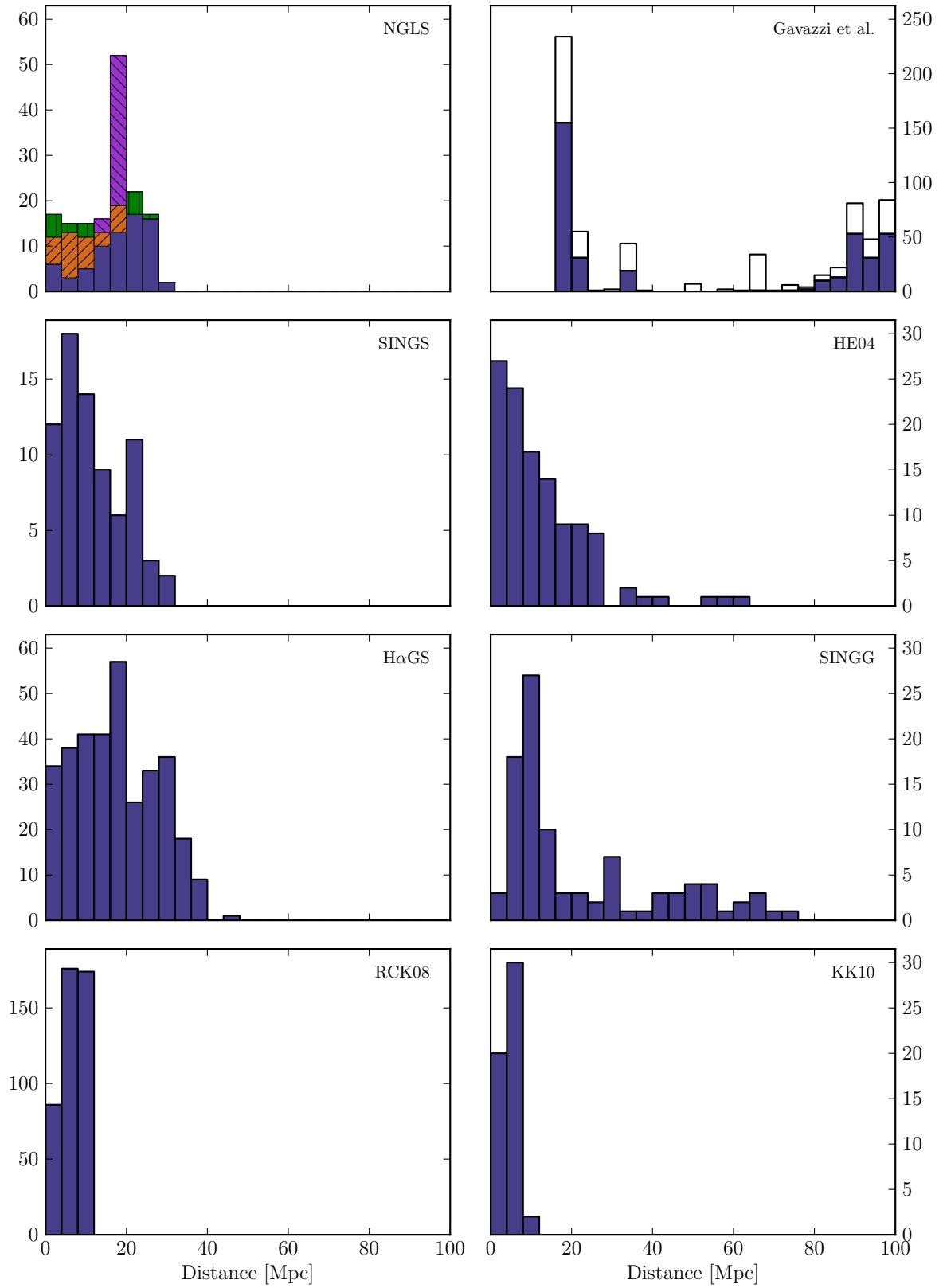


Figure 15. As Figure 14 but now showing the histograms of the distance in units of Mpc.

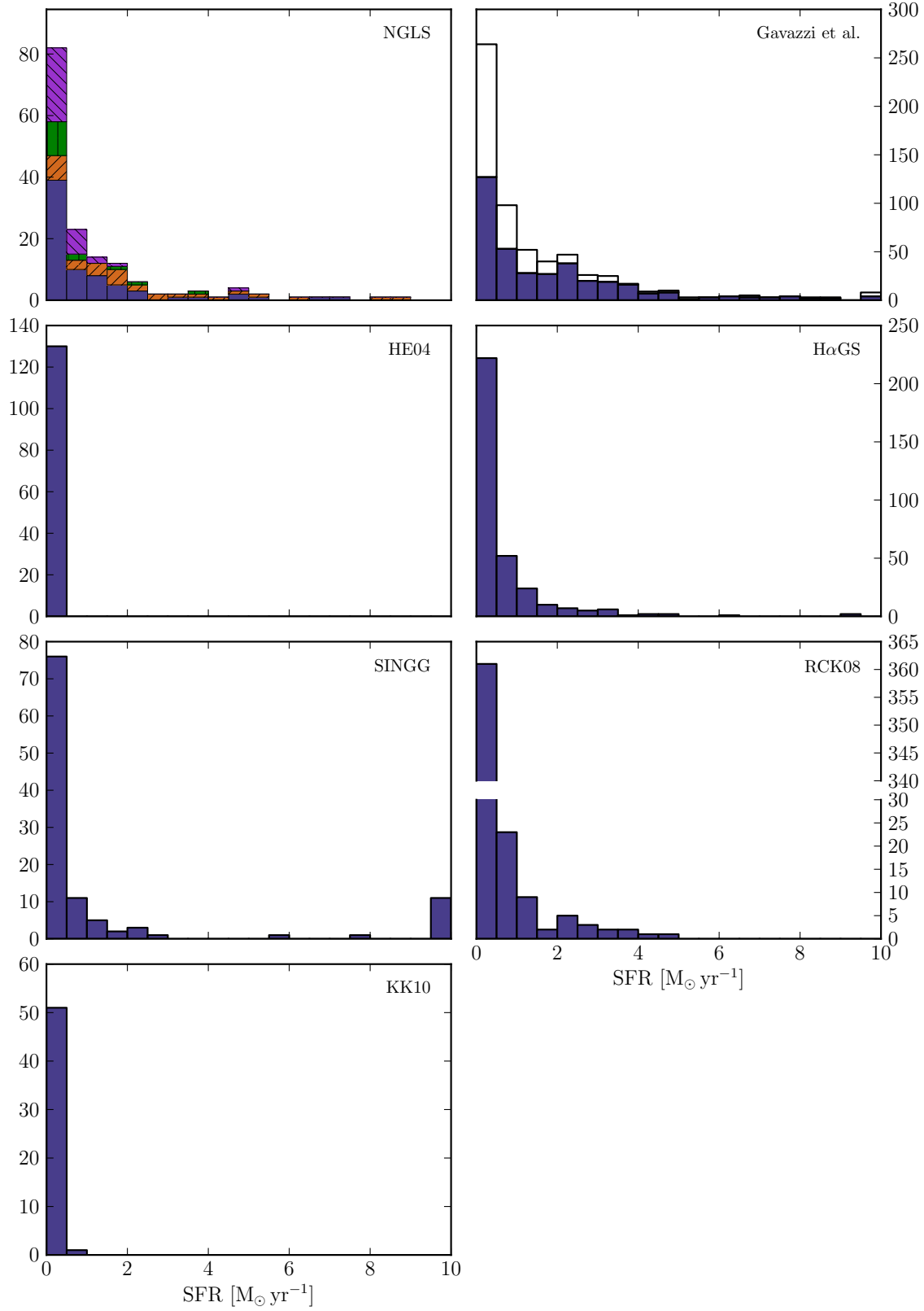


Figure 16. As Figure 14 but now showing the histograms of the SFR in units of $M_{\odot} \text{yr}^{-1}$. The values plotted here have been calculated directly from the $F(\text{H}\alpha)$ measurements taken from the catalogues using the same extinction and $F(\text{H}\alpha)$ -to-SFR values as in Sections 5.5 and 5.7.

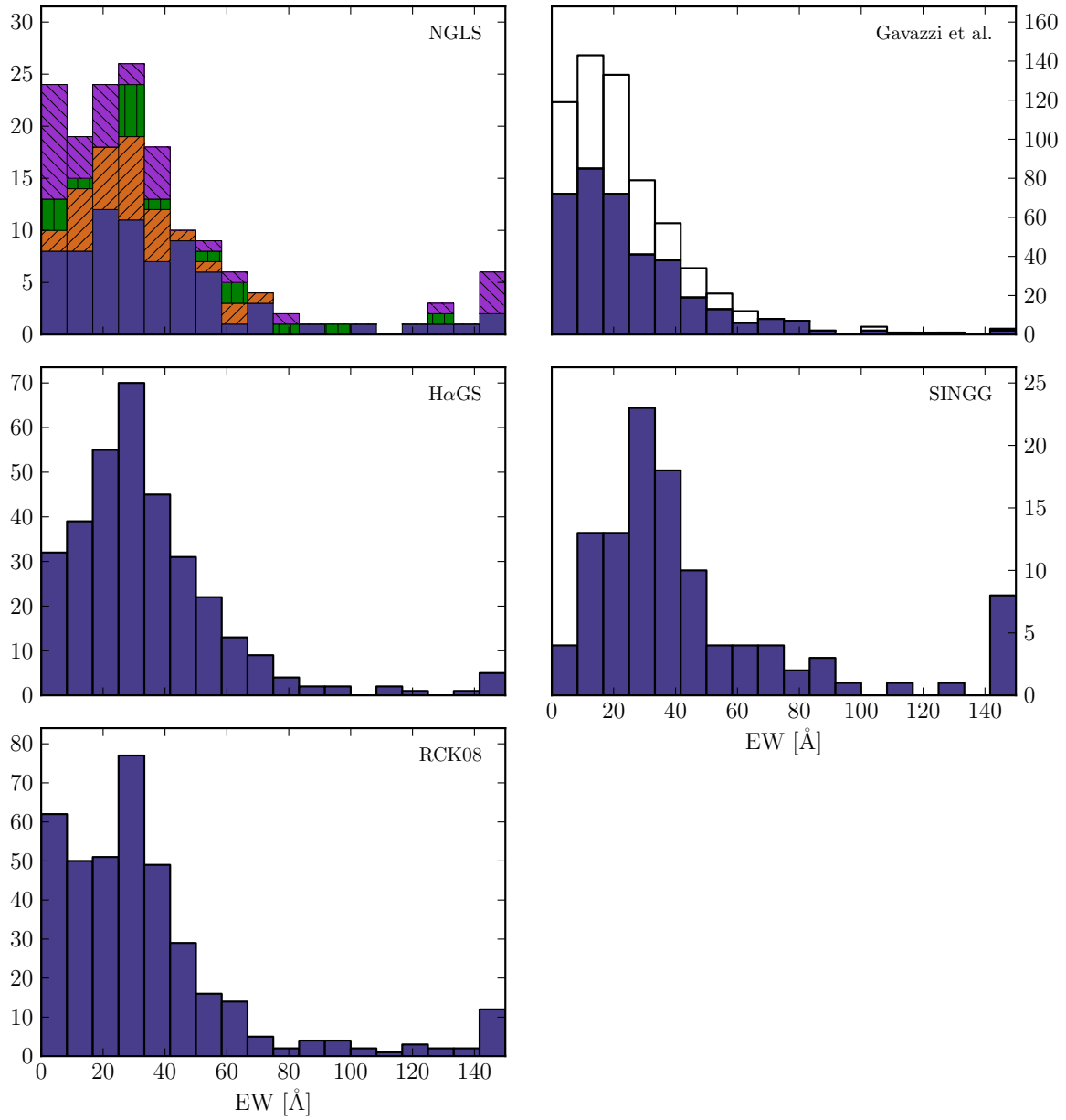


Figure 17. As Figure 14 but now showing the histograms of the EW in Ångströms.

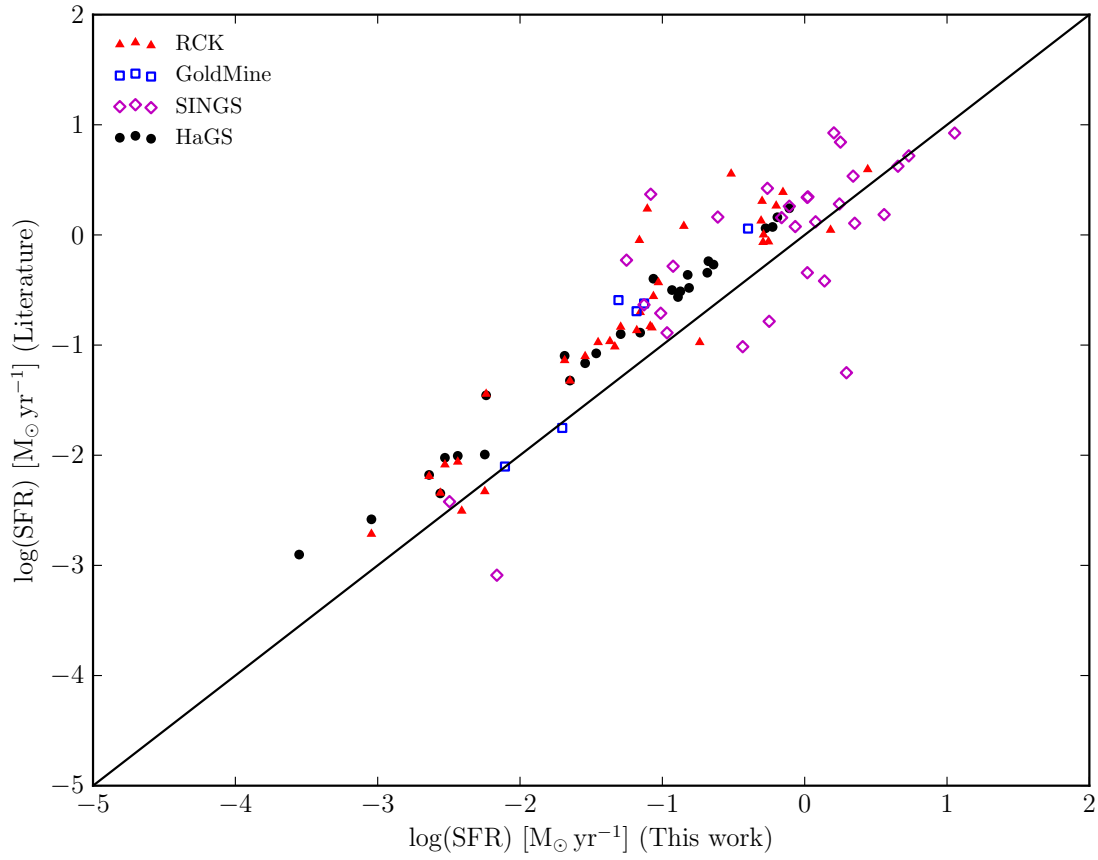


Figure 18. Comparison of SFR values calculated in this work with those obtained from the literature. Except in the case of the SINGS values, all the SFRs have been derived from the same images used in the literature. The solid line indicates $y = x$. Further details can be found in the text.